

## **ABSTRACT**

BRAVO, NIKOLAS BILY. Synthesis of Uncertainty Quantification, Surrogate Modeling, and Robust Control Design for PZT Bimorph Actuators. (Under the direction of Dr. Ralph Smith).

In this dissertation, we synthesize surrogate modeling, uncertainty quantification, and robust control design for a high fidelity model of a Lead Zirconate Titanate (PZT) bimorph actuator used for micro-air vehicles. This includes the Harvard Microrobotic Fly, also known as RoboBee. We quantify the high-fidelity actuator dynamics using the homogenized energy model (HEM) framework, which quantifies the nonlinear, hysteretic, and rate-dependent behavior inherent to PZT in dynamic operating regimes. We then identify the influential parameters using local and global sensitivity measures. We discuss the development of a local sensitivity method, which allows comparison between parameters having different orders of magnitude. Once the identifiable parameters are determined, we perform Bayesian inference on those parameters to determine the uncertainty in the parameters. We then propagate the uncertainty through the model to quantify the uncertainty in the tip displacement of the beam. To synthesize uncertainty quantification and control design, we investigate the extension of dynamic mode decomposition with control via interpolation to create a parameter and control-dependent surrogate model. Finally, we quantify uncertainty in different controllers to determine their robustness under parameter uncertainty. In this manner, we design a control that is robust to the parameter uncertainty.

© Copyright 2019 by Nikolas Bily Bravo

All Rights Reserved

Synthesis of Uncertainty Quantification, Surrogate Modeling, and Robust Control Design  
for PZT Bimorph Actuators

by  
Nikolas Bily Bravo

A dissertation submitted to the Graduate Faculty of  
North Carolina State University  
in partial fulfillment of the  
requirements for the Degree of  
Doctor of Philosophy

Applied Mathematics

Raleigh, North Carolina

2019

APPROVED BY:

---

Dr. Alen Alexanderian

---

Dr. Stephen Campbell

---

Dr. Matthew Bryant

---

Dr. Ralph Smith  
Chair of Advisory Committee

## **DEDICATION**

I would like to dedicate this dissertation to my wife, Paige, my parents, Shari and Roy, and to my brother Cameron. Without your support this journey would not be possible.

Thank you!

## **BIOGRAPHY**

Nikolas Bravo was born in Kansas City, Missouri. He was raised in Raymore, Missouri, and attended Raymore-Peculiar High School. His love of mathematics came from playing number games with his brother and parents. This motivated him to pursue a B.S in mathematics from the University of Nebraska-Lincoln- Go Huskers! Wanting to further his math knowledge, he earned a M.S. in applied mathematics from North Carolina State University in pursuit of his Ph.D. In his free time, he enjoys playing board games, coaching and playing water polo, going on adventures with his wife, Paige, and watching his cat, Marvin, zoom around the house.

## **ACKNOWLEDGEMENTS**

First, I must thank my wife, Paige, for her support throughout graduate school and her assistance editing this dissertation. Next, I must thank my brother, Cameron, for his guidance in helping me understand the physics in the model development and for suggesting helpful background reading material. Additionally, I must thank my parent, Roy and Shari, for their continued support and for always being an ear to vent to on this journey. Finally, I thank my advisor, Dr. Smith, for his assistance in this process.

This research was partially supported in part by the Air Force Office of Scientific Research (AFOSR) through the grant AFOSR FA9550-15-1-0299.

This material was also based upon work partially supported by the National Science Foundation under Grant DMS-1638521 to the Statistical and Applied Mathematical Sciences Institute (SAMSI). Any opinions, findings, and conclusions or recommendations expressed in this material are those of the author(s) and do not necessarily reflect the views of the National Science Foundation.

# TABLE OF CONTENTS

<b>LIST OF TABLES</b> . . . . .	<b>vii</b>
<b>LIST OF FIGURES</b> . . . . .	<b>viii</b>
<b>Chapter 1 Introduction</b> . . . . .	<b>1</b>
<b>Chapter 2 Model Development</b> . . . . .	<b>8</b>
2.1 Homogenized Energy Model . . . . .	8
2.2 Beam Model . . . . .	13
2.2.1 Numerical Solution . . . . .	19
2.3 Inverse Problem . . . . .	21
<b>Chapter 3 Sensitivity Analysis</b> . . . . .	<b>25</b>
3.1 Introduction . . . . .	25
3.2 Scaled Subset Selection . . . . .	27
3.2.1 Subset Selection . . . . .	27
3.2.2 Bayesian Inference on $\tau_{180}$ . . . . .	28
3.2.3 Scaled Subset Selection . . . . .	29
3.3 Parameter Subset Selection . . . . .	32
3.4 Pearson Correlation . . . . .	36
3.5 Active Subspaces . . . . .	38
3.6 Morris Screening . . . . .	42
3.7 Conclusion of Sensitivity Analysis . . . . .	44
<b>Chapter 4 Uncertainty Quantification</b> . . . . .	<b>47</b>
4.1 Bayesian Inference . . . . .	47
4.1.1 DRAM . . . . .	48
4.2 Uncertainty Propagation . . . . .	50
4.3 Results . . . . .	51
<b>Chapter 5 Parameter-dependent Dynamic Mode Decomposition</b> . . . . .	<b>54</b>
5.1 Dynamic Mode Decomposition . . . . .	54
5.1.1 Examples . . . . .	58
5.2 Dynamic Mode Decomposition with Control . . . . .	62
5.3 PI Control . . . . .	67
5.4 Interpolation method . . . . .	70
5.5 Results . . . . .	73
<b>Chapter 6 Synthesis of UQ and Control</b> . . . . .	<b>78</b>
6.1 Discrete-Time Tracking Problem . . . . .	78

6.1.1	Uncertainty in the Optimal Control . . . . .	82
6.2	Combining the Optimal and PI control . . . . .	83
<b>Chapter 7</b>	<b>Conclusion . . . . .</b>	<b>87</b>
<b>BIBLIOGRAPHY</b>	<b>. . . . .</b>	<b>90</b>



## LIST OF TABLES

Table 1.1	Nominal parameters values after model was fitted to data. . . . .	6
Table 2.1	Nominal parameter values after the model was fitted to data. . . . .	23
Table 3.1	The normalized eigenvalue associated with the parameter as it gets removed from the set of parameters. . . . .	30
Table 3.2	The normalized eigenvalue associated with the parameter as it gets removed from the set of parameters with the scaled derivative. . . . .	33
Table 3.3	Identifiable subset of parameters given the data for sets of size $n = 1, \dots, 5$ with unscaled partial derivatives. . . . .	35
Table 3.4	Identifiable subset of parameters given the data for sets of size $n = 1, \dots, 5$ with the scaled partial derivatives. . . . .	37
Table 3.5	The Pearson correlation values for $Y = \sqrt{\int_0^T y(t; q)^2 dt}$ and the parameter $X$ with the identifiable parameters from the scaled subset selection results in bold. . . . .	38
Table 3.6	The activity scores of the parameters for the quantity of interest $h(\theta) = \sqrt{\int_0^T y(t; \theta)^2 dt}$ . . . . .	42
Table 3.7	The Morris screening's sensitivity measures for the parameters with the quantity of interest $h(\theta) = \sqrt{\int_0^T y(t; \theta)^2 dt}$ . . . . .	44
Table 3.8	Local and Global sensitivity results. Parameters used for uncertainty quantification are bold. . . . .	46
Table 5.1	Singular values for HEM Example. . . . .	60
Table 5.2	Singular values for HEM Example with extrapolation. . . . .	62
Table 5.3	Time to complete one model run, DMD run with the data already obtained, and DMDip run. Also, the number of nodes used for each interpolation method for DMDip. . . . .	75

## LIST OF FIGURES

Figure 1.1	(a) Design of RoboBee and (b) picture of RoboBee from [42]. . . . .	2
Figure 1.2	The controlled flight of Robobee from [23]. . . . .	3
Figure 1.3	Nonlinear effects of PZT (a) Hysteresis loop [11], (b) Hysteresis butterfly from [11] and (c) rate dependence from [35]. . . . .	4
Figure 2.1	The grain and domain structure of PZT. . . . .	9
Figure 2.2	The unit cell of PZT in a (a) +180-well, (b) −180-well, and (c) 90-well. . . . .	10
Figure 2.3	The different material behavior across the domains of PZT. . . . .	13
Figure 2.4	(a),(b) The fit to data and (b) the densities from [17]. . . . .	14
Figure 2.5	Bimorph schematic. . . . .	14
Figure 2.6	Cross-sectional view of bimorph. . . . .	15
Figure 2.7	Simplified glass geometry for moment calculation. . . . .	17
Figure 2.8	Drive mechanism for bimorph actuators. . . . .	17
Figure 2.9	Cubic spline used for numerical solution. . . . .	20
Figure 2.10	Model fit to data from [5]. . . . .	24
Figure 3.1	Results from DRAM (a) chains, and (b) marginal densities. . . . .	31
Figure 3.2	The singular values from the activity subspace results, which are used to determine the active and inactive subspaces. . . . .	41
Figure 4.1	Results from DRAM (a) chains, (b) pairwise plots, and (c) marginal densities. . . . .	52
Figure 4.2	(a)95% credible intervals and prediction intervals and (b) magnification of (a). . . . .	53
Figure 5.1	DMD for the HEM driven by $V_b(t) = 150 + 150 \sin(4\pi t)$ at fixed spatial points: (a) $x = 0.0025m$ , (b) $x = 0.005m$ , (c) $x = 0.0075m$ , and (d) $x = 0.01m$ . . . . .	59
Figure 5.2	DMD approximation for the HEM driven by $V_b(t) = 150 + 150 \sin(4\pi t)$ using the first 0.8750 seconds of data to create the DMD, then extrapolating with the DMD at fixed spatial points: (a) $x = 0.0025m$ , (b) $x = 0.005m$ , (c) $x = 0.0075m$ , and (d) $x = 0.01m$ . . . . .	61
Figure 5.3	Impulse response for a simplified beam example at fixed spatial points: (a) $x = 0.1500m$ , (b) $x = 0.225m$ , (c) $x = 0.3000m$ , and (d) $x = 0.3750m$ . . . . .	63
Figure 5.4	Impulse response for a simplified beam example where sampling started at $t_0 = 2$ secs at fixed spatial points: (a) $x = 0.1500m$ , (b) $x = 0.2250m$ (c) $x = 0.3000m$ , and (d) $x = 0.3750m$ . . . . .	64

Figure 5.5	Data that was used to create the approximate the full-order system's state matrix $A$ and control matrix $B$ that is utilized in future control design and the DMDC approximation. . . . .	67
Figure 5.6	(a),(b) The performance of the designed PI controller and the control designed, and (c),(d) includes 5% noise. . . . .	68
Figure 5.7	(a) The control from DMDC as a feedforward control in HEM and (b) with 5% noise. . . . .	69
Figure 5.8	(a),(b)The control from DMDC as PI control in the high-fidelity model and (c),(d) with 5% noise. . . . .	70
Figure 5.9	Two dimensional level-3 Clenshaw-Curtis grid. . . . .	72
Figure 5.10	(a)Level-5 Lobatto grid based Smolyak's sparse grid and (b) Latin hypercube . . . . .	73
Figure 5.11	DMD with parameter interpolation results using 5 point Clenshaw-Curtis grid where each row are results from a different set of randomly drawn parameter values for $d_{\pm}$ , $\gamma_{pzt}$ , $P_R^{\pm}$ , and $\epsilon_R^{\pm}$ . . . . .	74
Figure 5.12	The relative error between the model andDMDip responses plotted against the parameters for (a) full Clenshaw grid, (b) Smolyak's sparse Lobatto grid , and (c) Latin hypercube. . . . .	76
Figure 5.13	The relative difference between the DMD and DMDip responses plotted against the parameters for (a) full clenshaw grid, (b) Smolyak's sparse Lobatto grid , and (c) Latin hypercube. . . . .	77
Figure 6.1	The DMDip (a)optimal trajectory and (b)optimal control with a randomly sampled set of parameters . . . . .	82
Figure 6.2	The HEM solution using the optimal control in Figure 6.1 where (a) trajectory and (b) magnification of (a) . . . . .	83
Figure 6.3	The HEM credible intervals of the tracking problem for (a) the control and (b),(c) the tip displacement. . . . .	84
Figure 6.4	The HEM solution using the optimal control in Figure 6.1 combined with the PI control from Section 5.3 where (a) trajectory and (b) control. . . . .	85
Figure 6.5	The HEM credible intervals of the tracking problem with combining the optimal control and PI control for (a),(b) the control and (c),(d) the tip displacement. . . . .	86

## CHAPTER

# 1

## INTRODUCTION

Lead Zirconate Titanate (PZT) bimorph actuators are utilized as the driving mechanisms in a number of micro-air vehicles (MAVs). Developed by Dr. Robert Woods, Harvard Micro-robotic Fly, or RoboBee, was designed for autonomous pollination using PZT bimorphs actuators. The Harvard Microrobotic Fly is an insect-size flapping-winged MAV as shown in Figure 1.1 [42]. This MAV can be used for hazardous terrain exploration, to aide in search and rescue missions, or intelligence gathering. These vehicles face many challenges to fly outside a controlled environment. Due to the MAV's small size, one of the most significant challenges is designing a control that is robust to turbulence and other uncertainties. Figure 1.2 is an image of the controlled flight of Dr. Wood's MAV [23]. We note that the MAV does not track the target trajectory with the desired accuracy. One objective of our research is to improve the control of these MAVs by understanding the uncertainty in the PZT bimorph actuator model and use the quantified uncertainty to develop robust control algorithms. Note we do not address the control of the MAV with regard to turbulence and wind.

PZT bimorph actuators can be driven at moderate to high frequencies and are energy

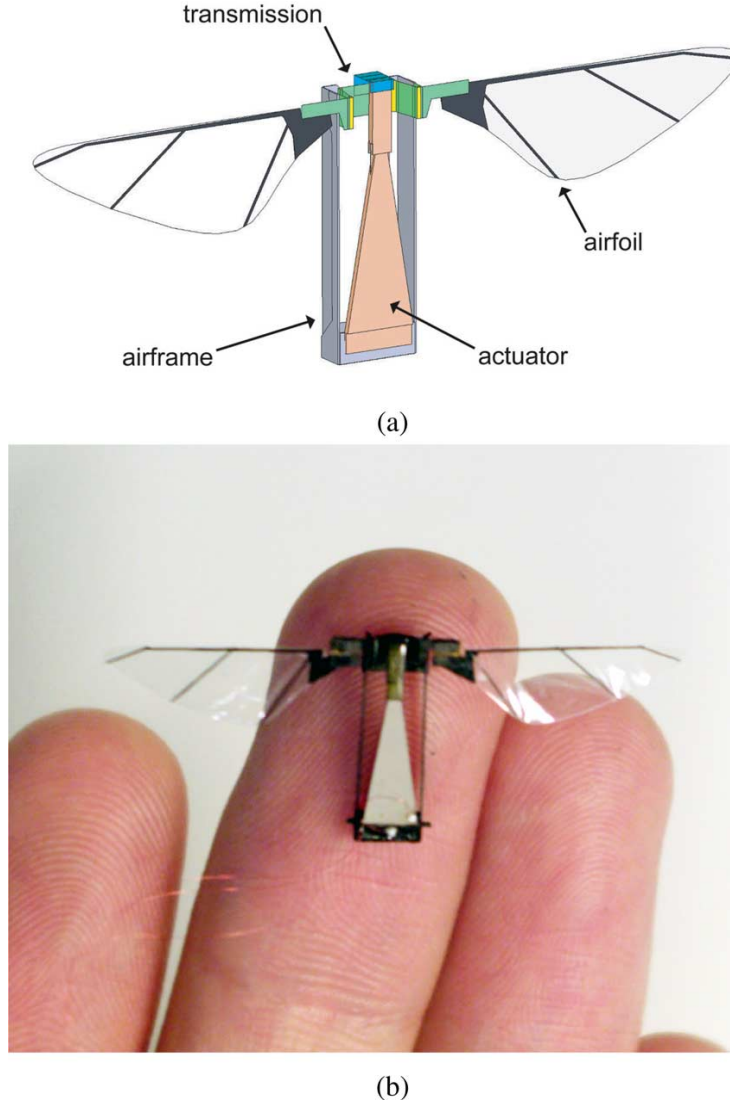


**Figure 1.1** (a) Design of RoboBee and (b) picture of RoboBee from [42].

efficient while exhibiting moderate work densities and high set-point precision. This makes PZT bimorphs an excellent choice to drive MAVs [42]. When driven in dynamic regimes, PZT bimorph actuators exhibit nonlinear, hysteretic, and rate-dependent behavior including creep, saturation, and stress-based effects. These properties are inherent to ferroelectric materials including PZT and can be observed in Figure 1.3. To accurately quantify the nonlinear behavior inherent to ferroelectric material; i.e., PZT, we need to use a nonlinear model for a PZT bimorph [43]. We use a homogenized energy model (HEM) framework to



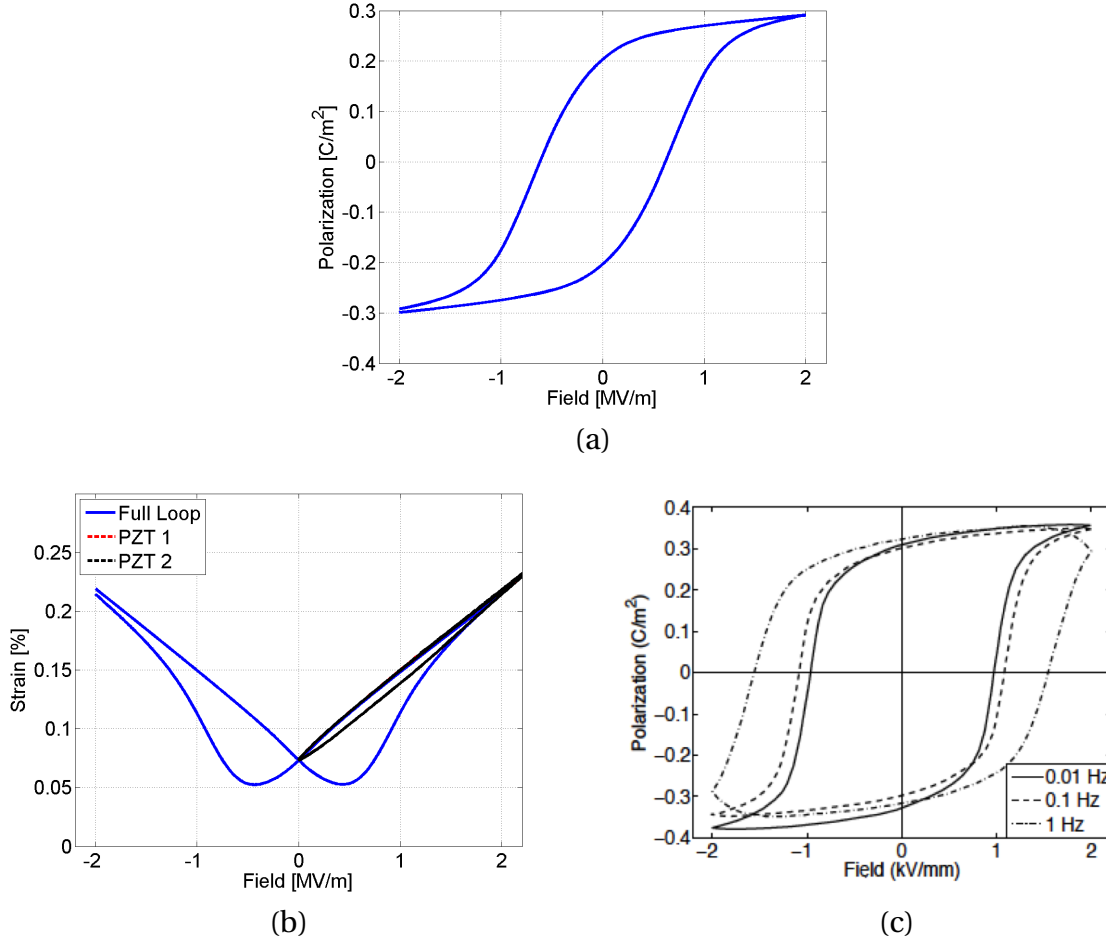


**Figure 1.3** Nonlinear effects of PZT (a) Hysteresis loop [11], (b) Hysteresis butterfly from [11] and (c) rate dependence from [35].

sary for model-based control designs in MAVs' dynamical regimes [23]. In [11], we demonstrated the implementation of a HEM for these actuators to quantify the nonlinearities. The actuator for the MAVs can be modeled as an Euler-Bernoulli cantilever beam, where the bending moment is comprised of active and passive parts [33]. We note that the HEM can be numerically inverted and implemented in real time for certain control regimes [12, 25, 27].

Understanding the uncertainty in the HEM model is necessary to develop a robust control. These uncertainties come from model limitations, parameters, and the data [34]. We use Bayesian inference to quantify the uncertainties from the observations and parameters.

In a Bayesian framework, parameters are taken to be random variables with associated distributions. Then, we propagate those uncertainties through to model to construct prediction and credible intervals for the quantity of interest, or the physically value that is being measured. For our application, the quantity of interest is the tip displacement of the bimorph. A 95% prediction interval represents the region where the next data sample will be located with a 95% probability. For our model, we consider 18 parameters as listed in Table 1.1. Depending on the information content of the data, all of the parameters cannot be inferred by the data. Therefore, before we perform uncertainty quantification, we need to determine the identifiable parameters in the model.

We use five different methods to determine the influential parameters, so we can fix the other parameters for Bayesian inference. The results of the five different methods will be compared with the results of our proposed method, scaled subset selection. We investigated two local sensitivity measures: Quaizer and Monnigmann's parameter subset selection [29] and Bank's, et al., parameter subset selection [2]. To distinguish between the two, we will call Quaizer and Monnigmann's method 'subset selection' and Bank's, et al., method 'parameter subset selection.' Subset selection does not work well when parameters are on different scales, so we created a scaled subset selection technique to determine the identifiable parameters for our model. The other four methods used were to verify the scaled subset selection results. We then used two global techniques to support our results from the local sensitivity analysis. The global techniques used were Pearson correlation [41] and Morris screening [26]. We finally use a technique to find an influential subspace in the parameter space called active subspaces [9]. Using the subspace, we can create activity scores to determine the most influential parameters [10]. For these methods, we considered the same parameter space as the one used for scaled subset selection. We determined four parameters to be identifiable and ran our uncertainty quantification on those parameters.

To improve computational efficiency, we also develop a data-driven model based on a dynamic mode decomposition (DMD), which approximates the Koopman operator [18, 19]. We employ an extension of DMD termed DMD with control (DMDc) for control problems. This method can be used to approximate the nonlinear control system as a discrete linear system [28]. Once we obtain the DMDc, we are able to design controls for the surrogate model [4, 6].

DMDc does not specifically accommodate the parameters, so the resulting surrogate model works for only one set of parameters. We developed an extension of DMDc, which



**Table 1.1** Nominal parameters values after model was fitted to data.

Parameter	Description
$\gamma$	Air damping coefficient (kg/s)
$\rho_{cf}$	Density of the CF layer (kg/m <sup>3</sup> )
$\rho_s$	Density of the S2 Glass (kg/m <sup>3</sup> )
$\rho_{pzt}$	Density of the PZT actuators (kg/m <sup>3</sup> )
$Y_{cf}$	Elastic modulus of CF (Pa)
$Y_s$	Elastic modulus of S2 Glass (Pa)
$c_{cf}$	Damping coefficient for CF(kg/s)
$c_s$	Damping coefficient for S2 Glass (kg/s)
$c_{pzt}$	Damping coefficient for PZT (kg/s)
$s^E$	Elastic compliance (1/Pa)
$d_{\pm}$	Piezoelectric coupling coefficient for $\alpha = \pm$ (m/V)
$\epsilon_R^{\pm}$	Remanent strain for $\alpha = \pm$ (%)
$\epsilon_R^{90}$	Remanent strain for $\alpha = 90$ (%)
$P_R^{\pm}$	Remanent polarization for $\alpha = \pm$ (C/m <sup>2</sup> )
$\chi^{\sigma}$	Ferroelectric susceptibility (F/m)
$\tau_{90}$	Relaxation time for 90° switching (s)
$\tau_{180}$	Relaxation time for 180° switching (s)
$\gamma_{pzt}$	Inverse of relative thermal energy (m <sup>3</sup> /J)

allows DMDC to be parameter and control-dependent by means of interpolation. This method was developed for projection-based surrogate models such as Proper Orthogonal Decomposition [13]. With this extension, we can perform robust control design, optimization and uncertainty quantification with DMDC.

Lastly, we synthesize our uncertainty quantification and control design. Specifically, we investigate uncertainty in optimal tracking problem. We specify the control as our quantity of interest to propagate the uncertainty in the model through the control problem to quantify the robustness with respect to the parameters of the control. We performed

this analysis on the optimal control tracking problem and a controller comprised of a combination of an optimal control and PI control.

In Chapter 2, we summarize the model for the HEM and beam model for the RoboBee. Chapter 3 consists of the sensitivity analysis followed by the uncertainty quantification results in Chapter 4. Chapter 5 introduces DMD and DMDc algorithms along with the development of DMDc with parameter interpolation. We discuss the synthesis of control design and uncertainty quantification in Chapter 6. Finally, we present conclusions and future work in Chapter 7. With the work accomplished in this dissertation, we contributed:

1. Employed the HEM framework model the bimorph actuator for RoboBee
2. Performed global and local sensitivity analysis on the HEM.
3. Created a local sensitivity analysis method for models with parameters that are on drastically different orders of magnitude.
4. Performed Bayesian inference on the identifiable parameters and propagated the uncertainties through the HEM.
5. Created DMDip which is a control and parameter-dependent surrogate model that can be used in parameter estimation of control systems and control design.
6. Developed a robust control algorithm for the HEM and quantified robustness of the controller under parameter uncertainty.

## CHAPTER

## 2

# MODEL DEVELOPMENT

### 2.1 Homogenized Energy Model

The homogenized energy model (HEM) quantifies the strains and polarization generated by applied electric fields in the PZT [35]. The HEM uses energy relations at the domain and grain levels to describe the macro-scale behavior of the material. The structure of the domain and grains of PZT are displayed in Figure 2.1. To begin, we use the Helmholtz and Gibbs energy densities,

$$\psi_{\alpha}(P, \epsilon) = \frac{1}{2} \eta_{\alpha}^{\epsilon} (P - P_R^{\alpha})^2 + \frac{1}{2} Y_{\alpha}^P (\epsilon - \epsilon_R^{\alpha})^2 + h_{\alpha} (P - P_R^{\alpha}) (\epsilon - \epsilon_R^{\alpha}), \quad (2.1)$$

$$G_{\alpha}(E, \sigma; P, \epsilon) = \psi_{\alpha}(P, \epsilon) - EP - \sigma \epsilon, \quad (2.2)$$

to derive the constitutive relations at the domain-level for the  $\alpha = 90, \pm 180$ -wells. Here,  $\eta_{\alpha}^{\epsilon}$  is the  $\alpha$ -variant of the inverse susceptibility at constant strain,  $Y_{\alpha}^P$  is the  $\alpha$ -variant of the elastic stiffness at constant polarization, and  $h_{\alpha}$  is the  $\alpha$ -variant piezoelectric constant. Note that  $P_R^{\alpha}$ ,  $\epsilon_R^{\alpha}$  are the remanent polarization of the  $\alpha$ -variant and remanence strain of

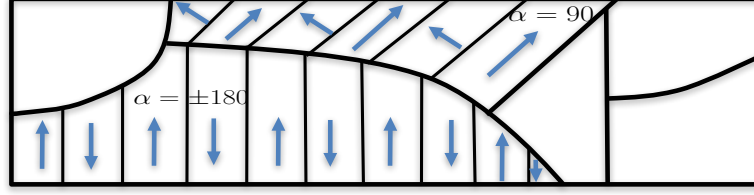


**Figure 2.1** The grain and domain structure of PZT.

the  $\alpha$ -variant, respectively. We set  $\frac{\partial G}{\partial P} = \frac{\partial G}{\partial \epsilon} = 0$  and solve for  $P$  and  $\epsilon$  to obtain

$$\begin{aligned} P_m^\alpha &= \chi_\alpha^\sigma E + d_\alpha \sigma + P_R^\alpha, \\ \epsilon_m^\alpha &= d_\alpha E + s_\alpha^E \sigma + \epsilon_R^\alpha \end{aligned}$$

as the polarization and strain that minimize the Gibbs energy density. It thus follows that

$$\chi_\alpha^\sigma = \frac{Y_\alpha^P}{Y_\alpha^P \eta_\alpha^\epsilon - h_\alpha^2}, \quad d_\alpha = \frac{-h_\alpha}{Y_\alpha^P \eta_\alpha^\epsilon - h_\alpha^2}, \quad s_\alpha^E = \frac{\eta_\alpha^\epsilon}{Y_\alpha^P \eta_\alpha^\epsilon - h_\alpha^2}.$$

Here,  $\chi_\alpha^\sigma$  is the  $\alpha$ -variant ferroelectric susceptibility inverse at constant stress,  $s_\alpha^E$  is the  $\alpha$ -variant elastic compliance at constant field, and  $d_\alpha$  is the  $\alpha$ -variant Piezoelectric coupling coefficient. The corresponding minimum Gibbs energy density is

$$G_{\alpha m} = -\frac{1}{2} \chi_\alpha^\sigma E^2 - \frac{1}{2} s_\alpha^E \sigma^2 - d_\alpha E \sigma - E P_R^\alpha - \sigma \epsilon_R^\alpha,$$

which we will use to define the probability of the transition from an  $\alpha$ -well to another  $\beta$ -well. Note we will use  $\pm$  to designate  $\pm 180$ -wells and 90 for the 90-wells for the remainder of the dissertation. Note that 90-wells are caused by applied stresses. Each of the units cells associated with each well are displayed in Figure 2.2.

The strain and polarization associated with each well can be interpreted as the integral averages of the strain and polarization in the energy minima. We use the low thermal activation approximations  $P_m^\alpha$  and  $\epsilon_m^\alpha$  to be the strain and polarization associated with each well for computational efficiency. The polarization and strain kernels are take to be

$$\bar{P} = \sum_{\alpha=\pm,90} x_\alpha P_m^\alpha, \quad \bar{\epsilon} = \sum_{\alpha=\pm,90} x_\alpha \epsilon_m^\alpha,$$

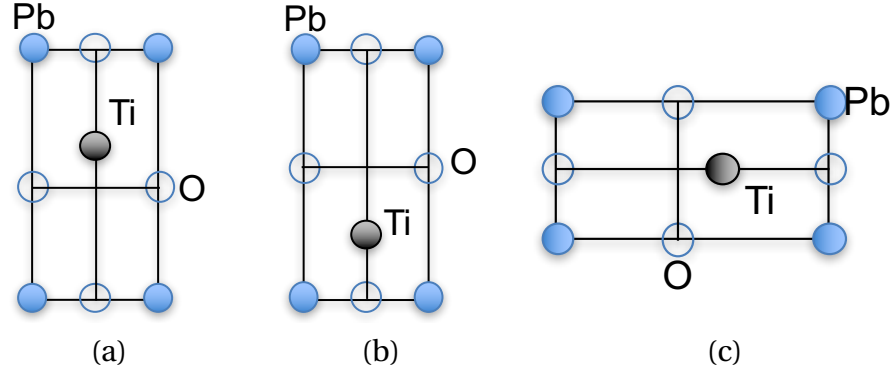


**Figure 2.2** The unit cell of PZT in a (a) +180-well, (b) -180-well, and (c) 90-well.

where  $x_\alpha$  is the dipole fraction associated with the  $\alpha$ -well. The evolution of dipole fractions is modeled as

$$\begin{aligned}\dot{x}_- &= -(p_{-90} + p_{-+} + p_{90-})x_- + (p_{+-} - p_{90-})x_+ + p_{90-}, \\ \dot{x}_+ &= (p_{-+} - p_{90+})x_- - (p_{+90} + p_{+-} + p_{90+})x_+ + p_{90+}.\end{aligned}$$

Here we utilize the fact  $x_+ + x_- + x_{90} = 1$ . Note that  $p_{\alpha\beta}$  is the probability of transitioning from the  $\alpha$ -well to the  $\beta$ -well as modeled by

$$p_{\alpha\beta} = \frac{1}{\tau_{\alpha\beta}} e^{-\Delta G_{\alpha\beta}^a(E, \sigma) \frac{V}{kT}}.$$

Here  $\tau_{\alpha\beta}$  is the relaxation time for  $\alpha$  to  $\beta$  switching and  $\frac{kT}{V}$  is the relative thermal energy. Note that  $T$  is the temperature,  $k$  is the Boltzmann's constant, and  $V$  is a constant volume.

The activation energy  $\Delta G_{\alpha\beta}^a(E, \sigma)$  is given by

$$\Delta G_{\alpha\beta}^a(E, \sigma) = \begin{cases} \Delta G_0 \left(1 - \frac{G_{\alpha m} - G_{\beta m}}{f_c}\right)^2, & G_{\alpha m} - G_{\beta m} \leq f_c, \\ 0, & G_{\alpha m} - G_{\beta m} > f_c. \end{cases}$$

Note that the activation energy represents the energy between the stable and unstable equilibrium of Gibbs energy density (2.2). Therefore, when the thermodynamic driving force,  $G_{\alpha m} - G_{\beta m}$ , is smaller than the critical driving force  $f_c$ , then  $\alpha$ -well stable equilibrium

is less than the unstable equilibrium, meaning the larger the activation energy, the less switching from a  $\alpha$ -well to a  $\beta$ -well will occur. In contrast, when  $G_{\alpha m} - G_{\beta m} > f_c$ , the  $\alpha$ -well equilibrium does not exist, so more switching to  $\beta$ -well will occur in order to achieve a stable state. The energy barrier at zero driving force  $\Delta G_0$  is given by

$$\Delta G_0 = \begin{cases} \frac{1}{4}f_c, & 180^\circ \text{Switching}, \\ \frac{1}{16}f_c, & 90^\circ \text{Switching}, \end{cases}$$

where we define  $f_c = 2E_c P_R$ . Here  $E_c$  is the coercive field. The coercive field is the electric field where the material begins to depolarize.

As in [35], the observed material behavior allows for the assumptions

$$\begin{aligned} \chi_+^\sigma &= \chi_-^\sigma = \chi_{90}^\sigma = \chi^\sigma, \\ s_+^E &= s_-^E = s_{90}^E = s^E, \\ P_R^{90} &= 0, \quad P_R^+ = -P_R^-, \quad \epsilon_R^+ = \epsilon_R^-, \\ d_{90} &= 0, \quad d_- = d_+, \\ \tau_{90-} &= \tau_{-90} = \tau_{90+} = \tau_{+90} = \tau_{90}, \quad \tau_{-+} = \tau_{+-} = \tau_{180}. \end{aligned} \tag{2.3}$$

These assumptions do not reduce the generality of the model. The model is still capable of quantifying the behavior of many different materials. Under these assumptions, the governing equations become

$$\begin{aligned} \bar{P}(E, \sigma) &= \bar{d}(E, \sigma)\sigma + \chi^\sigma E + \bar{P}_{irr}(E, \sigma), \\ \bar{\epsilon}(E, \sigma) &= s^E \sigma + \bar{d}(E, \sigma)E + \bar{\epsilon}_{irr}(E, \sigma), \end{aligned}$$

where

$$\begin{aligned} \bar{P}_{irr}(E, \sigma) &= \sum_{\alpha=\pm, 90} P_R^\alpha x_\alpha(E, \sigma), \\ \bar{\epsilon}_{irr}(E, \sigma) &= \sum_{\alpha=\pm, 90} \epsilon_R^\alpha x_\alpha(E, \sigma), \\ \bar{d}(E, \sigma) &= \sum_{\alpha=\pm, 90} d_\alpha x_\alpha(E, \sigma). \end{aligned}$$

To complete the HEM, we take the average of the kernels over the grains and domains to obtain the constitutive relations

$$\begin{aligned} P(E, \sigma) &= d(E, \sigma)\sigma + \chi^\sigma E + P_{irr}(E, \sigma), \\ \varepsilon(E, \sigma) &= s^E \sigma + d(E, \sigma)E + \varepsilon_{irr}(E, \sigma). \end{aligned}$$

The macroscopic piezoelectric coupling is given by

$$d(E, \sigma_0) = \int_0^\infty \int_{-\infty}^\infty \bar{d}(E(t) + E_I, \sigma_0; f_c) \nu_c(f_c) \nu_I(E_I) dE_I df_c. \quad (2.4)$$

The irreversible strain function is

$$\varepsilon_{irr}(E, \sigma_0) = \int_0^\infty \int_{-\infty}^\infty \bar{\varepsilon}_{irr}(E(t) + E_I, \sigma_0; f_c) \nu_c(f_c) \nu_I(E_I) dE_I df_c, \quad (2.5)$$

and the irreversible polarization function is

$$P_{irr}(E, \sigma_0) = \int_0^\infty \int_{-\infty}^\infty \bar{P}_{irr}(E(t) + E_I, \sigma_0; f_c) \nu_c(f_c) \nu_I(E_I) dE_I df_c.$$

As in [35], the average incorporates the effects of polycrystallinity, material nonhomogeneities, and variable interaction. The interaction field,  $E_I$ , quantifies how the different grains and domain interact with each other and determines the effective field,  $E_e = E(t) + E_I$ , on each domain. A constant interaction field would describe that all grains and domains interact the same, but having an underlying distribution for the interaction field will allow different interactions to be modeled. Averaging over the critical driving force,  $f_c = 2E_c P_R$ , allows the varying coercive fields over the domain to be represented in the model. Note, the coercive field,  $E_c$ , is the applied electric field where the material begins to depolarize. Figure 2.3 demonstrates how the coercive fields vary across domains and how they produce different material behavior.

The density functions

$$\begin{aligned} \nu_c(f_c) &= \frac{1}{c_1} \sum_{k=1}^{K_{f_c}} \gamma_k \phi_k(f_c), \\ \nu_I(E_I) &= \frac{1}{c_2} \sum_{k=1}^{K_{E_I}} \eta_k \phi_k(E_I), \end{aligned}$$

are taken to be linear combinations of lognormal,  $\phi_k(f_c)$ , and normal density functions,  $\psi_k(E_I)$  [35]. We choose  $\phi_k(f_c)$  to be log-normal, because the domain of  $f_c$  is  $[0, \infty]$  and the distribution needs to decay exponentially. As for  $\psi(E_I)_k$  being normal distributions, we desire a density function that decays exponentially and that is symmetric to reproduce the effects of low-field Rayleigh loops [35]. Therefore, lognormal and normal densities are natural choices. Here  $c_1$  and  $c_2$  are coefficients that ensure the density function integrates to unity and the coefficients  $\gamma_k$  and  $\eta_k$  were found through least square fits to data as displayed in Figure 2.4 from [17]. The integrals can be calculated using composite Gaussian quadrature techniques. Note, we can reduce the domain to a finite region due to the exponential decay of the densities.

## 2.2 Beam Model

Figures 2.5 and 2.6 depict the PZT bimorph actuators under consideration. Following the development in [33], the actuator can be modeled as an Euler-Bernoulli cantilever beam

$$\rho(x) \frac{\partial^2 w(x, t)}{\partial t^2} + \gamma \frac{\partial w(x, t)}{\partial t} - \frac{\partial^2 M(x, t)}{\partial x^2} = 0, \quad (2.6)$$

with  $x \in [0, x_4]$ ,  $t \geq 0$  and boundary conditions

$$w(0, t) = \frac{\partial w}{\partial x}(0, t) = M(x_4, t) = \frac{\partial M}{\partial x}(x_4, t) = 0.$$

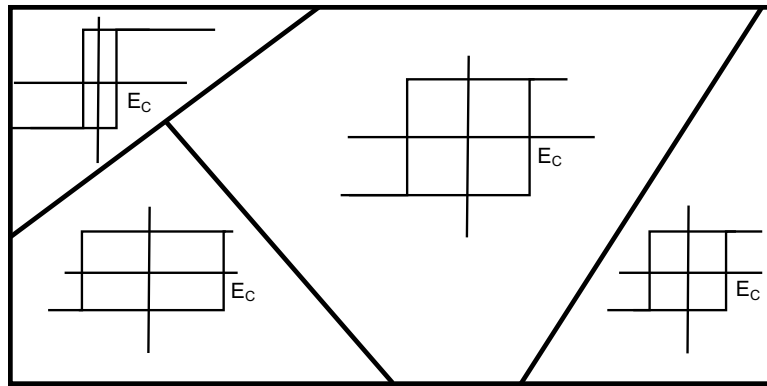


**Figure 2.3** The different material behavior across the domains of PZT.



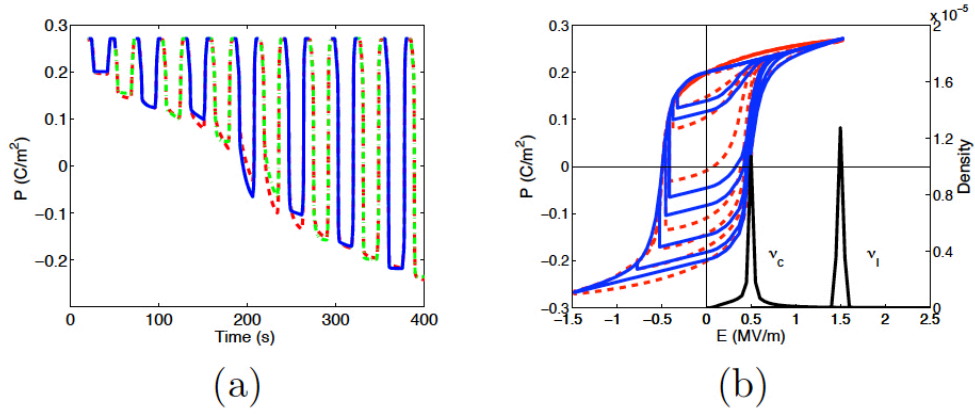


**Figure 2.4** (a),(b) The fit to data and (b) the densities from [17].

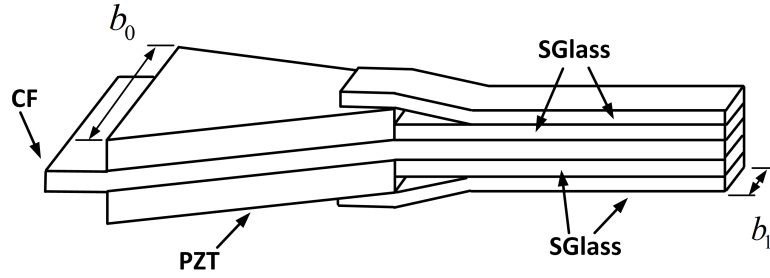


**Figure 2.5** Bimorph schematic.

Here  $w(x, t)$  is the transverse displacement,  $\rho(x)$  is the composite linear density,  $\gamma$  is the air damping coefficient,  $M(x, t)$  is the moment and  $L$  is the length of the beam.

Let  $h_{cf}$ ,  $b_{cf}$ , and  $\rho_{cf}$  denote the height, width, and density of the carbon fiber (CF) beam,  $h_{pzt}$ ,  $b_{pzt}$ , and  $\rho_{pzt}$  are the height, width, and density of the PZT patches, and  $h_s$ ,  $b_s$ , and  $\rho_s$  are the height, width, and density of the S2 Glass. Note that the  $\chi_{pzt}(x)$  describes where the PZT patch is located and  $\chi_s(x)$  describes location and quantifies number of pieces of S2 Glass components. The composite linear density is

$$\rho(x) = h_{cf} b_{cf}(x) \rho_{cf} + 2 \chi_{pzt}(x) h_{pzt} b_{pzt}(x) \rho_{pzt} + \chi_s(x) h_s b_s \rho_s,$$

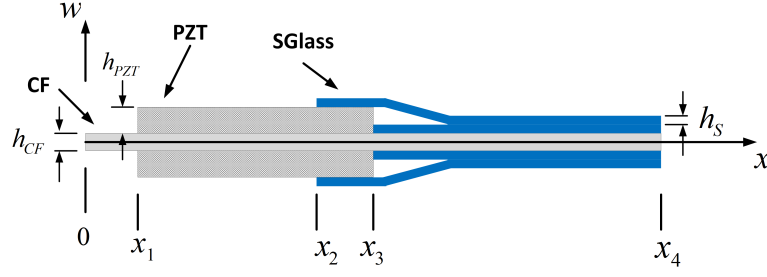


**Figure 2.6** Cross-sectional view of bimorph.

where

$$b_{cf}(x) = \begin{cases} b_0, & x < x_1 \\ b_0 - (b_0 - b_1) \frac{x - x_1}{x_3 - x_1}, & x_1 \leq x \leq x_3 \\ b_1, & x > x_3, \end{cases}$$

$$\chi_{pzt}(x) = \begin{cases} 1, & x_1 \leq x \leq x_3 \\ 0, & \text{else,} \end{cases}$$

$$b_{pzt}(x) = b_0 - (b_0 - b_1) \frac{x - x_1}{x_3 - x_1},$$

and

$$\chi_s(x) = \begin{cases} 0, & x \leq x_2 \\ 2, & x_2 \leq x \leq x_3 \\ 4, & x > x_3. \end{cases}$$

Note that  $x_1 = 1$  mm,  $x_2 = 5.5$  mm,  $x_3 = 6.5$  mm,  $x_4 = 10$  mm,  $h_{cf} = 0.1778$  mm,  $h_s = 31.75$   $\mu$ m,  $h_{pzt} = 0.127$  mm,  $b_0 = 1.5$  mm and  $b_1 = 1$  mm.

The moment can be separated into its active  $M_A(x, t)$  and passive  $M_P(x, t)$  components

$$M(x, t) = M_A(x, t) + M_P(x, t).$$

The passive component is due to the carbon fiber beam and the S2 Glass. To compute the moments, we simplify the geometry in the manner depicted in Figure 2.7, so the two spaces between the two pieces of S2 glass are removed to decrease computation complexity. The

moment due to the carbon fiber is

$$M_{cf} = \int_{-h_{cf}/2}^{h_{cf}/2} b_{cf}(x)(z - z_N) \sigma_{cf} dz, \quad (2.7)$$

where the stress in the carbon fiber,  $\sigma_{cf}$ , is given by

$$\sigma_{cf} = Y_{cf} \epsilon + c_{cf} \frac{\partial \epsilon}{\partial t}.$$

Here,  $Y_{cf}$  is the elastic Young's modulus of carbon fiber, and  $c_{cf}$  is the Kelvin-Voigt damping coefficient. The moment due to the S2 Glass is given by

$$\begin{aligned} M_s = & \int_{h_{pzt}}^{h_{pzt}+h_s} b_1(z - z_N) \sigma_s \chi_{s1}(x) dz + \int_{-h_{pzt}-h_s}^{h_{pzt}} b_1(z - z_N) \sigma_s \chi_{s1}(x) dz \\ & + \int_{h_{cf}}^{h_{cf}+2h_s} b_1(z - z_N) \sigma_s \chi_{s2}(x) dz + \int_{-h_{cf}-2h_s}^{-h_{cf}} b_1(z - z_N) \sigma_s \chi_{s2}(x) dz, \end{aligned} \quad (2.8)$$

where

$$\begin{aligned} \chi_{s1}(x) &= \begin{cases} 1, & x_2 \leq x \leq x_3 \\ 0, & \text{else,} \end{cases} \\ \chi_{s2}(x) &= \begin{cases} 1, & x > x_3 \\ 0, & \text{else,} \end{cases} \end{aligned}$$

and

$$\sigma_s = Y_s \epsilon + c_s \frac{\partial \epsilon}{\partial t}.$$

Note that  $\chi_{s1}(x)$  isolates the portion of the beam where the S2 Glass rests on top of the PZT patch and  $\chi_{s2}(x)$  is the characteristic function for the portion of the S2 Glass that rests on top of the carbon fiber beam.

The active moment due to the PZT is patch given by

$$\begin{aligned} M_A = & \int_{h_{cf}/2}^{h_{pzt}+h_{cf}/2} b_{pzt}(x)(z - z_N) \sigma_{pzt,1} \chi_{pzt}(x) dz \\ & + \int_{-h_{pzt}-h_{cf}/2}^{-h_{cf}/2} b_{pzt}(x)(z - z_N) \sigma_{pzt,2} \chi_{pzt}(x) dz. \end{aligned} \quad (2.9)$$

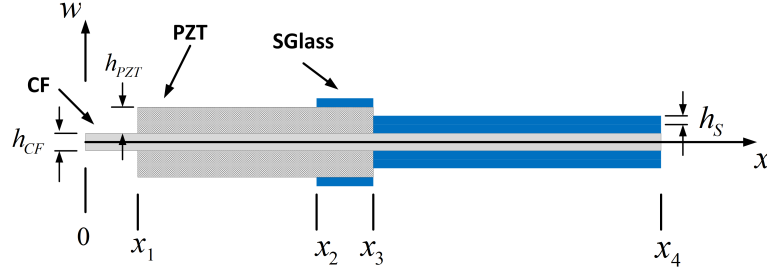


**Figure 2.7** Simplified glass geometry for moment calculation.

The stress in the PZT actuators is modeled using the nonlinear constitutive relationship

$$\begin{aligned}\sigma_{pzt,1} &= \frac{1}{s^E} [\epsilon - d(E_1(t), \sigma_0)E_1(t) - \epsilon_{irr}(E_1(t), \sigma_0)] + \frac{1}{s^E} \epsilon_{irr}(0, \sigma_0) + c_{pzt} \frac{\partial \epsilon}{\partial t}, \\ \sigma_{pzt,2} &= \frac{1}{s^E} [\epsilon - d(E_2(t), \sigma_0)E_2(t) - \epsilon_{irr}(E_2(t), \sigma_0)] + \frac{1}{s^E} \epsilon_{irr}(0, \sigma_0) + c_{pzt} \frac{\partial \epsilon}{\partial t}.\end{aligned}\quad (2.10)$$

Here  $s^E$  is the elastic compliance under constant field and  $c_{pzt}$  is the Kelvin-Voigt damping coefficient. The macroscopic nonlinear and hysteretic piezoelectric coupling coefficient and irreversible strain function are described in (2.4) and (2.5), respectively.

In Figure 2.8, we display the drive schematics for the actuator. The bimorph actuators are driven with a simultaneous, dual-source mechanism [44]. The outside of one actuator receives a constant voltage  $V_{\max}$  and the outside of the other actuator is grounded. The carbon fiber beam serves as a third electrode and is driven with voltage  $V_b(t)$ , where  $0 \leq V_b(t) \leq V_{\max}$ . The applied electric fields in the actuators are related to the voltage by the

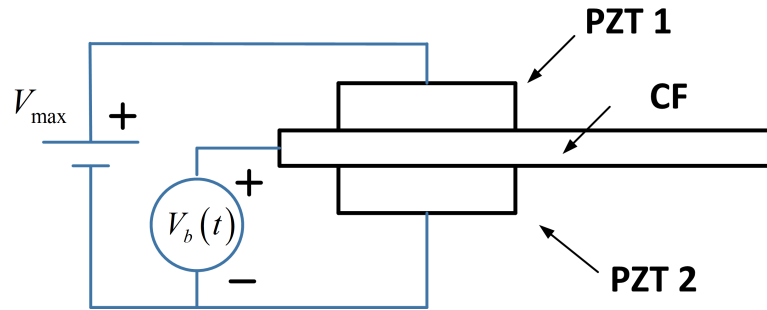


**Figure 2.8** Drive mechanism for bimorph actuators.

relations

$$E_1(t) = \frac{V_{\max} - V_b(t)}{h_{pzt}}, \quad E_2(t) = \frac{V_b(t)}{h_{pzt}}.$$

Note, that the static neutral position of the actuator occurs when  $V_b(t) = V_{\max}/2$ .

The elastic strain is modeled using the Kirchhoff relation

$$\varepsilon(z) = \kappa(z - z_N), \quad (2.11)$$

where the curvature  $\kappa$  is approximated by

$$\kappa = - \frac{\partial^2 w(x, t)}{\partial x^2}.$$

Using the fact that  $z_N = 0$  due to symmetry, the Kirchhoff hypothesis (2.11), and evaluating the integrals (2.7) - (2.10), yields the moment relations

$$\begin{aligned} M_{cf} &= \frac{1}{12} b_{cf}(x) h_{cf}^3 \left( -Y_{cf} \frac{\partial^2 w(x, t)}{\partial x^2} - c_{cf} \frac{\partial^3 w(x, t)}{\partial t \partial x^2} \right), \\ M_s &= \frac{2}{3} b_1 \left[ \chi_{s1} \left( (h_{pzt} + h_s)^3 - h_{pzt}^3 \right) + \chi_{s2} \left( (h_{cf} + 2h_s)^3 - h_{cf}^3 \right) \right] \\ &\quad \cdot \left( -Y_s \frac{\partial^2 w(x, t)}{\partial x^2} - c_s \frac{\partial^3 w(x, t)}{\partial t \partial x^2} \right), \\ M_A &= \frac{2}{3} b_{pzt}(x) \chi_{pzt}(x) \left( (h_{pzt} + \frac{1}{2} h_{cf})^3 - \frac{1}{8} h_{cf}^3 \right) \left( -\frac{1}{s^E} \frac{\partial^2 w(x, t)}{\partial x^2} - c_{pzt} \frac{\partial^3 w(x, t)}{\partial t \partial x^2} \right) \\ &\quad + \frac{1}{2} b_{pzt}(x) \chi_{pzt}(x) \frac{1}{s^E} \left[ \left( h_{pzt} + \frac{1}{2} h_{cf} \right)^2 - \frac{1}{4} h_{cf}^2 \right] \\ &\quad \cdot \left[ -d(E_1(t), \sigma_0) E_1(t) + d(E_2(t), \sigma_0) E_2(t) - \varepsilon_{irr}(E_1(t), \sigma_0) + \varepsilon_{irr}(E_2(t), \sigma_0) \right]. \end{aligned} \quad (2.12)$$

Finally, the total moment in (2.6) is given by

$$M(x, t) = -Y I(x) \frac{\partial^2 w(x, t)}{\partial x^2} - c I(x) \frac{\partial^3 w(x, t)}{\partial t \partial x^2} + f(x, t), \quad (2.13)$$

where

$$\begin{aligned} Y I(x) &= Y_{cf} I_{cf}(x) + Y_s I_s(x) + \frac{1}{s^E} I_{pzt}(x), \\ c I(x) &= c_{cf} I_{cf}(x) + c_s I_s(x) + c_{pzt} I_{pzt}(x), \\ I_{cf}(x) &= \frac{1}{12} b_{cf}(x) h_{cf}^3, \\ I_s(x) &= \frac{2}{3} b_1 \left[ \chi_{s1} \left( (h_{pzt} + h_s)^3 - h_{pzt}^3 \right) + \chi_{s2} \left( (h_{cf} + 2h_s)^3 - h_{cf}^3 \right) \right], \\ I_{pzt}(x) &= \frac{2}{3} b_{pzt}(x) \chi_{pzt}(x) \left( (h_{pzt} + \frac{1}{2} h_{cf})^3 - \frac{1}{8} h_{cf}^3 \right) \end{aligned} \quad (2.14)$$

and

$$\begin{aligned}
f(x, t) &= \frac{c_1}{s^E} \chi_{pzt}(x) \\
&\cdot \left[ -d(E_1(t), \sigma_0) E_1(t) + d(E_2(t), \sigma_0) E_2(t) - \varepsilon_{irr}(E_1(t), \sigma_0) + \varepsilon_{irr}(E_2(t), \sigma_0) \right], \quad (2.15) \\
c_1 &= \frac{1}{2} b_{pzt}(x) \left( (h_{pzt} + \frac{1}{2} h_{cf})^2 - \frac{1}{4} h_{cf}^2 \right).
\end{aligned}$$

### 2.2.1 Numerical Solution

To compute a numerical solution for the beam model, we substitute (2.13) into (2.6). We then multiply (2.6) by a test function,  $\phi(x)$ , and integrate by parts to yield the weak formulation,

$$\begin{aligned}
\int_0^{x_4} \left[ \rho(x) \frac{\partial^2 w(x, t)}{\partial t^2} \phi(x) + \gamma \frac{\partial w(x, t)}{\partial t} \phi(x) \right. \\
\left. + Y I(x) \frac{\partial^2 w(x, t)}{\partial x^2} \phi''(x) + c I(x) \frac{\partial^3 w(x, t)}{\partial t \partial x^2} \phi''(x) - f(x, t) \phi''(x) \right] dx = 0. \quad (2.16)
\end{aligned}$$

A Galerkin method is used to approximate the weak solution. Let the approximate solution be of the form

$$w^N(x, t) = \sum_{k=1}^{N+1} w_k(t) \phi_k(x), \quad (2.17)$$

where  $N$  is the number of subintervals of the domain  $[0, x_4]$  used to approximate the solution and  $\phi_k$  are basis functions. Here  $N$  was selected by convergence study of the numerical solution. The solution with  $N$  test functions was compared with the solution with  $2N$  test functions by calculating the difference between the two. We doubled  $N$  until the two solutions varied by less than 1% to prove the solution has converged.

We chose the basis functions,

$$\phi_k(x) = \begin{cases} \widehat{\phi}_0 - 2\widehat{\phi}_{-1} - 2\widehat{\phi}_1, & k = 1 \\ \widehat{\phi}_k, & k = 2, \dots, N+1 \end{cases}$$

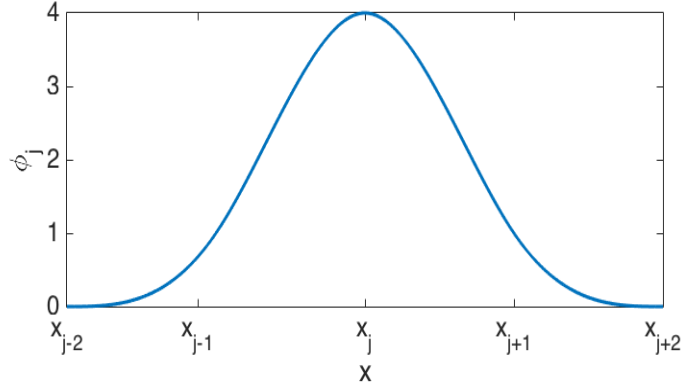


**Figure 2.9** Cubic spline used for numerical solution.

where

$$\widehat{\phi}_k(x) = \frac{1}{h^3} \begin{cases} (x - \hat{x}_{k-2})^3, & x \in [\hat{x}_{k-2}, \hat{x}_{k-1}) \\ h^3 + 3h^2(x - \hat{x}_{k-1}) + 3h(x - \hat{x}_{k-1})^2 - 3(x - \hat{x}_{k-1})^3, & x \in [\hat{x}_{k-1}, \hat{x}_k) \\ h^3 + 3h^2(\hat{x}_{k+1} - x) + 3h(\hat{x}_{k+1} - x)^2 - 3(\hat{x}_{k+1} - x)^3, & x \in [\hat{x}_k, \hat{x}_{k+1}) \\ (\hat{x}_{k+2} - x)^3, & x \in [\hat{x}_{k+1}, \hat{x}_{k+2}] \\ 0, & \text{otherwise} \end{cases}$$

to be the cubic spline in Figure 2.9. Here  $h = \frac{x_4}{N}$ . We selected these cubic splines, because they form a basis for our test function space  $H_0^2(0, x_4) = \{H^2(0, x_4) | \phi(0) = \phi'(0) = 0\}$  with the inner product of

$$\langle \phi, \psi \rangle = \int_0^{x_4} Y I(x) \phi'' \psi'' dx.$$

We next solve for  $w_k(t)$ .

Substituting (2.17) into (2.16), we obtain the system

$$M \frac{d^2 w(t)}{dt^2} + Q \frac{dw(t)}{dt} + K w(t) = f(t),$$

where

$$\begin{aligned} [M]_{ij} &= \int_0^{x_4} \rho(x) \phi_i \phi_j dx, \\ [Q]_{ij} &= \int_0^{x_4} [\gamma \phi_i \phi_j + c I(x) \phi_i'' \phi_j''] dx, \\ [K]_{ij} &= \int_0^{x_4} Y I(x) \phi_i'' \phi_j'' dx, \\ [f(t)]_i &= \int_0^{x_4} f(x, t) \phi_i'' dx. \end{aligned}$$

Note  $w(t) = [w_1(t), \dots, w_{n+1}(t)]^T$ . We obtain a first-order differential equation by letting  $z_1(t) = w(t)$  and  $z_2(t) = \frac{dw}{dt}(t)$  to yield

$$\frac{dz}{dt} = Az + B(t), \quad (2.18)$$

where

$$A = \begin{bmatrix} \mathbf{0} & \mathbf{I} \\ -M^{-1}K & -M^{-1}Q \end{bmatrix}, \quad B(t) = \begin{bmatrix} \mathbf{0} \\ -M^{-1}f(t) \end{bmatrix}.$$

Here  $\mathbf{0}$  and  $\mathbf{I}$  are the zero matrix and identity matrix, respectively, and  $z(t) = [z_1(t), z_2(t)]^T$ . We note from (2.15) that  $f(t)$  is nonlinearly dependent on the applied electric field,  $E_1(t)$  and  $E_2(t)$ . Through these applied fields, we will develop control algorithms for the nonlinear system. We solve (2.18) with a numerical ordinary differential equation solver. We implemented implicit Euler for the numerical solution, because it is highly efficient. We used gaussian elimination to solve the system at each step in implicit Euler. We validated the numerical solution by comparing it with MATLAB's stiff solver *ode15s*.

## 2.3 Inverse Problem

The solution to the deterministic inverse problem will be employed as the nominal values for our model. These nominal values will be utilized as initial values for Delayed Rejection Adaptive Metropolis (DRAM), the algorithm used to perform Bayesian inference. We avoid nondimensionalizing the problem, because the physical parameter values are informative of material properties and are important to identify individually. The data used was collected from Figure 5(a) in [43]. We used the MATLAB function *digitize2.m* to collect the data from



the image. We sampled one full wingbeat from the image at 41 evenly spaced points letting the first and last point be the same point. We then assumed that the frequency of the wingbeat is 110 Hz, which is the resonant frequency [42]. When we compare the data and the model output of the transverse tip displacement, we allow the bimorph to complete 4.5 cycles before using the output of the model. By doing this, we eliminate the influence of the initial conditions of the dipole fractions from the output. The data set accurately informs the HEM component of the model, but we are not able to learn about the damping behavior from this particular data set. This is due to the sinusoidal behavior of the electric field.

With the assumptions in (2.3), we list the remaining 18 parameters in Table 2.1 along with their nominal values. The nominal values were determined using MATLAB's *fminsearch.m* to develop an initial value for MATLAB's *fmincon.m*, where we minimize the square errors of the difference of the model predictions and the data. We employed *fminsearch.m* for 500 iteration before stopping to checking the parameter values were physically reasonable. If the parameters values were reasonable, then we continued with *fminsearch.m* for another 500 iterations. Once parameters were no longer physically reasonable, we stop and used the result of *fminsearch.m* from the previous 500 iterations. We used these parameters values as initial values for *fmincon.m* and  $\pm 20\%$  of the initial values as the bounds for the problem. We used default options for *fmincon.m* which uses the finite-difference method to compute the gradient and the 'interior-point' algorithm. The algorithm converged to a possible local minimizer, because the step-size of the current step was smaller than the tolerance of  $10^{-4}$ . We note that we will use Bayesian inference to determine the global minimizer. These optimal values which we will define as our nominal values will be provide initial values for further analysis. Figure 2.10 displays the model's fit to the data with the nominal parameter values. We used the values in Table 2.1 for the rest of the dissertation unless stated otherwise.

**Table 2.1** Nominal parameter values after the model was fitted to data.

Parameter	Description	Value
$\gamma$	Air damping coefficient (kg/s)	0.0015
$\rho_{cf}$	Density of the CF layer (kg/m <sup>3</sup> )	$2.27 \times 10^3$
$\rho_s$	Density of the S2 Glass (kg/m <sup>3</sup> )	$1.81 \times 10^3$
$\rho_{pzt}$	Density of the PZT actuators (kg/m <sup>3</sup> )	$1.22 \times 10^3$
$Y_{cf}$	Elastic modulus of CF (Pa)	$4.57 \times 10^{11}$
$Y_s$	Elastic modulus of S2 Glass (Pa)	$8.65 \times 10^{11}$
$c_{cf}$	Damping coefficient for CF (kg/s)	$1.25 \times 10^4$
$c_s$	Damping coefficient for S2 Glass (kg/s)	$6.66 \times 10^3$
$c_{pzt}$	Damping coefficient for PZT (kg/s)	$1.32 \times 10^3$
$s^E$	Elastic compliance (1/Pa)	$1.12 \times 10^{-11}$
$d_{\pm}$	Piezoelectric coupling coefficient for $\alpha = \pm$ (m/V)	$8.79 \times 10^{-10}$
$\epsilon_R^{\pm}$	Remanent strain for $\alpha = \pm$ (%)	0.1771
$\epsilon_R^{90}$	Remanent strain for $\alpha = 90$ (%)	$-8.12 \times 10^{-13}$
$P_R^{\pm}$	Remanent polarization for $\alpha = \pm$ (C/m <sup>2</sup> )	0.1208
$\chi^{\sigma}$	Ferroelectric susceptibility (F/m)	$1.24 \times 10^{-6}$
$\tau_{90}$	Relaxation time for 90° switching (s)	$1.50 \times 10^{-6}$
$\tau_{180}$	Relaxation time for 180° switching (s)	$9.25 \times 10^{-13}$
$\gamma_{pzt}$	Inverse of relative thermal energy (m <sup>3</sup> /J)	0.0853

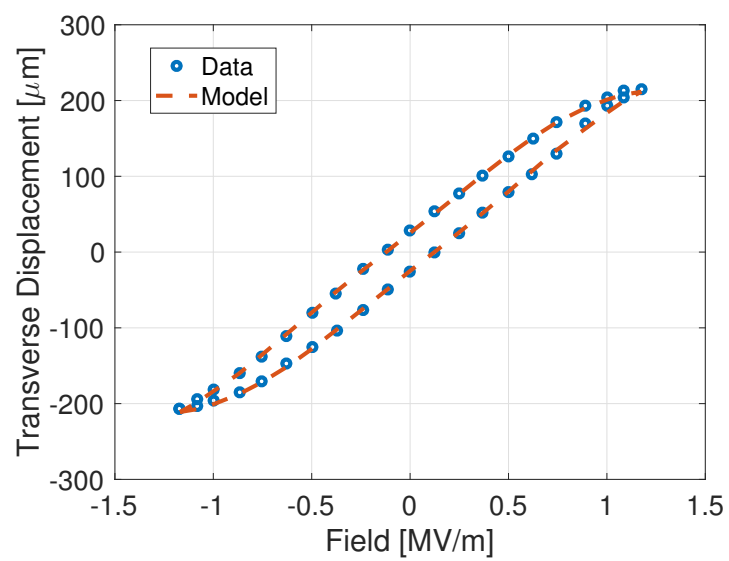


**Figure 2.10** Model fit to data from [5].

## CHAPTER

### 3

# SENSITIVITY ANALYSIS

## 3.1 Introduction

Before performing Bayesian inference and uncertainty quantification on the model, we must determine the identifiable or influential parameters. As defined in [34], identifiable parameters are the parameters that are uniquely determined by the data. More rigorously, let  $y$  denote the map

$$y = f(q),$$

where  $q \in U \subset \mathbb{R}^p$ . Note  $U$  is the feasible parameter space. The parameters  $q$  are identifiable at  $q^*$  if  $f(q) = f(q^*)$  implies that  $q = q^*$  for  $q^* \in U$ . Influential parameters are the parameters that cause a noticeable change in the output; i.e., we say  $q \in U \subset \mathbb{R}^p$  are a non-influential set of parameters if  $|y(q) - y(q^*)| < \epsilon$  for all  $q, q^* \in U$  and some  $\epsilon \ll O(y(q))$ .

We determine the influential parameters, or in some cases the non-influential parameters through sensitivity analysis. There are two types of sensitivity analysis: local and global. A local sensitivity measure determines the parameters that are influential around a specific set of parameters,  $q_0$ . The two local methods we consider exploit the partial derivative with

respect to the parameters at the point  $q_0$  to determine the identifiable parameters. These methods examine which parameters cause the most change to the quantity of interest around the nominal values. Alternatively, global sensitivity methods explore the entire parameter space to determine the influential parameters. These methods quantify how the uncertainties in the quantity of interest are apportioned to uncertainties in parameters. There are global methods that compare the correlation between the parameters and the quantity of interest, average the local sensitivities across the parameter space, and some variance based method. There are many different techniques to calculate sensitivities, but we will focus on five different methods: Quaizer and Monnigmann’s parameter subset selection, Bank’s, et al., parameter subset selection, Pearson correlation, Morris screening, and activity scores from active subspaces. We did not use any variance-based methods like, Sobol indices [37], because these tend to be more sensitive to the assumption of independent parameters, which is violated by our model.

We investigate two local methods that employ the nominal values from Section 2.3. The first is an adaptation of Quaizer and Monnigmann’s parameter subset selection [29]. We will show that the algorithm has difficulties when the scales of the parameter values are drastically different. We propose a scaled adaptation of the method to produce accurate results. The Q-M’s method uses the eigenstructure of a scaled Fischer information matrix to determine the non-influential parameters. The second method is the Bank’s, et al., parameter subset selection [2] which, given a data set, determines an identifiable set of parameters that minimizes uncertainty; i.e., the asymptotic standard error. This method determines a set of parameters for a given size of the set. We can determine the appropriate size by calculating the rank of the covariance matrix. Bank’s, et al., parameter subset selection is capable of comparing parameter that are on drastically different scales. We note to distinguish between two methods, we will call Quaizer and Monnigmann’s method ‘subset selection’ and Bank’s, et al., method ‘parameter subset selection.’

The other three methods are global methods. The first method we consider is Pearson correlation [41], because parameters on drastically different scales are normalized within the method. Pearson correlation is used to describe the correlation between two random variables. If we let both our parameters and output be random variables, then we can determine how correlated a parameter is to our quantity of interest. If the correlation value is large, then the parameters are determined to be influential to the quantity of interest. Next, we will use active subspaces to determine the identifiable parameters [9]. The active

subspace method is not a global sensitivity analysis method, but can be used to create a global sensitivity metric through activity scores [10]. Active subspace methods determine an influential subspace of the parameter space. Note that the subspace consist of linear combinations of parameters. We determine the set of influential parameters by calculating activity scores for the parameter in the active subspace. Finally, we investigate the derivative-based global sensitivity measure of Morris screening [26]. The Morris screening method approximates the average partial derivative for each parameter across the parameter space. Morris screening is a derivative-based global method that compares naturally with the scaled subset selection. This determines a ranking for the influential parameters. It also determines the variance as an additional measure to compare the parameters, so we can see how the derivatives vary more across the parameter space. We will compare the results of the five methods to select which set of parameters to use while performing Bayesian inference and uncertainty propagation.

## 3.2 Scaled Subset Selection

### 3.2.1 Subset Selection

We first determine the partial derivatives evaluates at the parameter values in Table 2.1 to create the Fischer information matrix. This matrix can be used to determine the identifiable parameters.

Following the development of subset selection detailed in [29], we define the functional

$$J(q) = \frac{1}{N} \sum_{n=1}^N [y_n - f(t_n, q)]^2,$$

where  $q = [q_1, \dots, q_p]$  is the vector of parameters,  $y_n$  is the observed tip displacement at  $t = t_n$ , and  $f$  is the model output. We then Taylor expand the model around the optimal  $q^*$  to obtain

$$J(q) \approx \frac{1}{N} \sum_{n=1}^N [y_n - (f(t_n, q^*) + \nabla f(t_n, q^*) \Delta q)]^2.$$

Assuming that  $q^*$  is the minimizer, this yields  $y_n \approx f(t_n, q^*)$  and

$$J(q) \approx J(q^* + \Delta q) = \frac{1}{N} \sum_{n=1}^N [\nabla f(t_n, q^*) \Delta q]^2.$$

We define

$$\chi = \begin{bmatrix} \frac{\partial f}{\partial q_1}(t_1, q^*) & \cdots & \frac{\partial f}{\partial q_m}(t_1, q^*) \\ \vdots & \ddots & \vdots \\ \frac{\partial f}{\partial q_1}(t_N, q^*) & \cdots & \frac{\partial f}{\partial q_m}(t_N, q^*) \end{bmatrix}.$$

We then can write

$$J(q^* + \Delta q) = \frac{1}{N} \Delta q^T \chi^T \chi \Delta q.$$

If we let  $\Delta q$  be an eigenvector of  $\chi^T \chi$  with eigenvalue  $\lambda$ , we obtain

$$J(q^* + \Delta q) = \frac{1}{N} \lambda \|\Delta q\|_2^2.$$

If  $\lambda$  is small, then the eigenvector has very little influence on the cost functional. We note that the eigenvectors components quantify the amount of change in each parameter.

We implemented Algorithm 1 the subset selection algorithm from [29] to determine the identifiable parameters. To compute the partial derivatives, we use a finite-difference technique to approximate derivatives with a step size of  $1 \times 10^{-4}\%$  of the nominal value. The rank of  $\chi^T \chi$  is five during the first iteration. We decided to make  $\epsilon = 10^{-8}$  in step (3) and (4) from Algorithm 1, because it is the square root of machine precision. Table 3.1 displays the results of subset selection given the data and the normalized eigenvalues that we associated with the parameter when it was removed from  $\chi$ . The influential parameters are  $\tau_{180}$ ,  $d_{\pm}$ , and  $S^E$ .

### 3.2.2 Bayesian Inference on $\tau_{180}$

We ran Bayesian inference on the model to find the uncertainty of each of the identifiable parameters. As detailed in Chapter 4, we used the Delayed Rejection Adaptive Metropolis (DRAM) algorithm to calculate the posterior distributions [16]. The algorithm produces posterior probability distributions for each of the parameters and the distributions need to converge in the probabilistic sense. The data does not inform the prior, so the algorithm does not converge when we used all three identifiable parameters. We then ran Bayesian inferences for only  $\tau_{180}$  to show that subset selection algorithm does not produce an identifiable set of parameters. Here  $\tau_{180}$  is not informed by the data.

We used the nominal parameters from Table 2.1 as initial values for the  $\tau_{180}$  and fixed the other parameters. We ran the algorithm for 30,000 samples with 10,000 samples used as

1. Determine or approximate

$$\chi = \begin{bmatrix} \frac{\partial f}{\partial q_1}(t_1, q^*) & \cdots & \frac{\partial f}{\partial q_m}(t_1, q^*) \\ \vdots & \ddots & \vdots \\ \frac{\partial f}{\partial q_1}(t_N, q^*) & \cdots & \frac{\partial f}{\partial q_m}(t_N, q^*) \end{bmatrix}.$$

2. Compute the smallest eigenvalue,  $\lambda$ , and corresponding eigenvector,  $v$ , of  $\chi^T \chi$ . Also, compute the largest eigenvalue,  $\lambda_{max}$ .
3. If  $\frac{\lambda}{\lambda_{max}} > \epsilon$ , then stop. The parameters that correspond to the remaining columns of  $\chi$  are the identifiable parameters
4. If  $\frac{\lambda}{\lambda_{max}} < \epsilon$ , then identify the largest component in magnitude,  $v_i$ , of  $v$  where  $v = (v_i)_{i=1}^{18}$ .  
Remove the corresponding column of  $\chi$  and repeat steps 2 - 4.

**Algorithm 1:** Quaizer and Monnigmann's parameter subset selection algorithm [29].

burn-in. Burn-in is the samples we collect to ensure that the algorithm has converged before generating the chains of the posterior distribution. We used samples after the burn-in to create marginal distribution for the identifiable parameter. Figure 3.1 displays the chain and marginal density created from the results. The chains explore the entire space, but the posterior distribution is the same as the prior, which we took as a uniform distribution. This means that all values of  $\tau_{180}$  are equally likely, causing  $\tau_{180}$  to be unidentifiable. It appeared to be a sensitive parameter when using parameter subset selection, because the order of magnitude of the nominal value. Therefore, the subset selection did not select the identifiable parameters due to the vast differences in scaling. This motivates the use of a scaled subset selection.

### 3.2.3 Scaled Subset Selection

We note that the parameters which were selected as identifiable in the subset selection were of very small magnitude. This causes division by numbers on the order of  $10^{-19}$ . It is also difficult to compare parameters or derivatives that are on different scales and have different units. We need to normalized the parameters to have accurate subset selection results.



**Table 3.1** The normalized eigenvalue associated with the parameter as it gets removed from the set of parameters.

Parameter	Description	$\lambda$
$\gamma$	Air damping coefficient(kg/s)	$5.30 \times 10^{-30}$
$\rho_{cf}$	Density of the CF layer (kg/m <sup>3</sup> )	$4.84 \times 10^{-36}$
$\rho_s$	Density of the S2 Glass (kg/m <sup>3</sup> )	$2.16 \times 10^{-36}$
$\rho_{pzt}$	Density of the PZT actuators (kg/m <sup>3</sup> )	$3.41 \times 10^{-40}$
$Y_{cf}$	Elastic modulus of CF (Pa)	$-3.05 \times 10^{-55}$
$Y_s$	Elastic modulus of S2 Glass (Pa)	$4.27 \times 10^{-57}$
$c_{cf}$	Damping coefficient for CF (kg/s)	$3.35 \times 10^{-45}$
$c_s$	Damping coefficient for S2 Glass(kg/s)	$5.45 \times 10^{-45}$
$c_{pzt}$	Damping coefficient for PZT (kg/s)	$3.19 \times 10^{-42}$
$s^E$	<b>Elastic compliance (1/Pa)</b>	1.00
$d_{\pm}$	<b>Piezoelectric coupling coefficient for <math>\alpha = \pm</math> (m/V)</b>	$3.65 \times 10^{-6}$
$\epsilon_R^{\pm}$	Remanent strain for $\alpha = \pm$ (%)	$1.21 \times 10^{-18}$
$\epsilon_R^{90}$	Remanent strain for $\alpha = 90$ (%)	$8.16 \times 10^{-9}$
$P_R^{\pm}$	Remanent polarization for $\alpha = \pm$ (C/m <sup>2</sup> )	$3.66 \times 10^{-24}$
$\chi^{\sigma}$	Ferroelectric susceptibility (F/m)	$4.55 \times 10^{-25}$
$\tau_{90}$	Relaxation time for 90° switching (s)	$5.13 \times 10^{-14}$
$\tau_{180}$	<b>Relaxation time for 180° switching (s)</b>	$4.89 \times 10^{-5}$
$\gamma_{pzt}$	Inverse of relative thermal energy (m <sup>3</sup> /J)	$-1.42 \times 10^{-20}$

Our original model is of the form

$$f(t_n, q) : \mathbb{R} \times \mathbb{R}^p \mapsto \mathbb{R}.$$

To obtain parameters on the same scale, we map them to  $[0, 1]^p$ . We define the scaled model as

$$h(t_n, \theta) : \mathbb{R} \times [0, 1]^p \mapsto \mathbb{R},$$

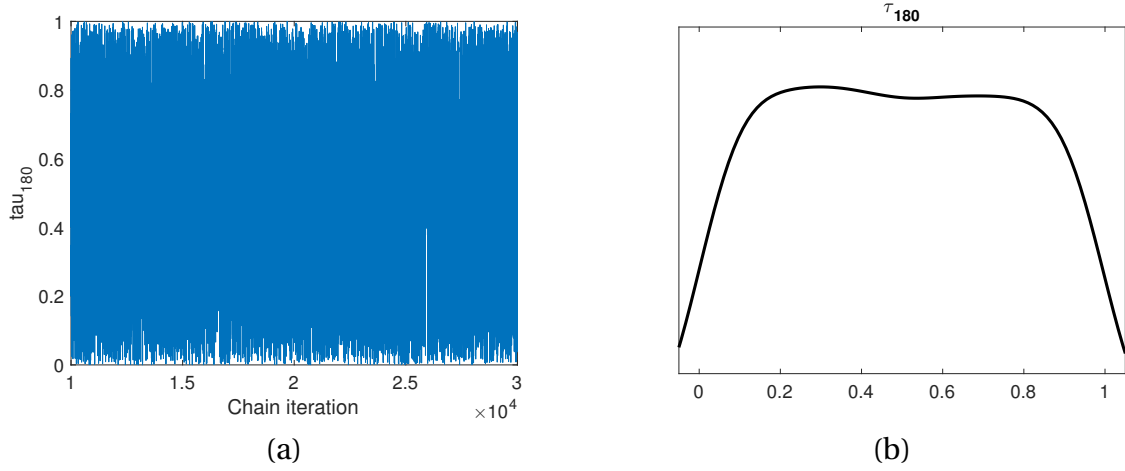


**Figure 3.1** Results from DRAM (a) chains, and (b) marginal densities.

such that

$$h(t_n, \theta) = f(t_n, g(\theta)),$$

where

$$g : [0, 1]^p \mapsto \mathbb{R}^p$$

is the map from the interval  $[0, 1]^p$  to the physical parameter space. We consider the map

$$g_k(\theta_k) = (0.8 + 0.4\theta_k)q_k^*$$

in our analysis. We note that  $g_k$  maps to  $\pm 20\%$  of the nominal parameter value  $q_k^*$  from Table 2.1. We define  $g(\theta) = [g(\theta_1), \dots, g(\theta_p)]^T$ . With this map, correlated parameters will still be correlated, but the correlation coefficients will be scaled. This produces a scaled derivative that allows a comparison of the parameters local sensitivities for parameters on

drastically different scales. For  $p = 1$ , the approximate derivative is

$$\begin{aligned}
h'(\theta) &\approx \frac{h(\theta + \Delta) - h(\theta)}{\Delta}, \\
&= \frac{f(g(\theta + \Delta)) - f(g(\theta))}{\Delta}, \\
&\approx \frac{f(g(\theta) + \Delta g'(\theta)) - f(g(\theta))}{\Delta}, \\
&\approx \frac{f(g(\theta)) + \Delta g'(\theta) f'(g(\theta)) - f(g(\theta))}{\Delta}, \\
&\approx f'(g(\theta)) g'(\theta),
\end{aligned}$$

where  $\Delta$  is the step size. We use the Algorithm 1, but with the model  $h(t_n, \theta)$ . The results are displayed in Table 3.2. We have four identifiable parameters,  $d_{\pm}$ ,  $\gamma_{pzt}$ ,  $P_R^{\pm}$ , and  $\epsilon_R^{\pm}$ . Note that  $\tau_{180}$  is no longer determined to be an identifiable parameter. We will perform Bayesian inference on these four parameters in Chapter 4. For these results, we chose only four parameter to be identifiable, because the results in Section 3.2.1 indicated only three parameters where selected and the rank of the sensitivity matrix in Section 3.2.1 was five. When we selected five parameters, the DRAM was not converging. In future work, we will investigate why the chains are not converging.

### 3.3 Parameter Subset Selection

To verify the results from the scaled subset selection, we also consider other local and global sensitivity measures. The other local sensitivity method is parameter subset selection from [2]. The object of the method is to determine an identifiable set of parameters, which minimizes uncertainty for the inverse problem given a data set. The uncertainty that is being minimized is the asymptotic standard error. The goal is to minimize

$$\alpha(q_I) = \|\nu(q_I)\|_2,$$

where the coefficients of variation for  $q_i \in q_I = \{q_{i_1}, \dots, q_{i_n}\}$  with  $1 \leq i_1 < \dots < i_n \leq p$  is

$$\nu(q_i) = \frac{\text{Standard Error}(q_i)}{q_i}.$$

**Table 3.2** The normalized eigenvalue associated with the parameter as it gets removed from the set of parameters with the scaled derivative.

Parameter	Description	$\lambda$
$\gamma$	Air damping coefficient (kg/s)	$8.21 \times 10^{-23}$
$\rho_{cf}$	Density of the CF layer (kg/m <sup>3</sup> )	$-4.31 \times 10^{-18}$
$\rho_s$	Density of the S2 Glass (kg/m <sup>3</sup> )	$1.25 \times 10^{-13}$
$\rho_{pzt}$	Density of the PZT actuators (kg/m <sup>3</sup> )	$2.56 \times 10^{-13}$
$Y_{cf}$	Elastic modulus of CF (Pa)	$3.96 \times 10^{-8}$
$Y_s$	Elastic modulus of S2 Glass (Pa)	$-3.17 \times 10^{-19}$
$c_{cf}$	Damping coefficient for CF (kg/s)	$3.40 \times 10^{-18}$
$c_s$	Damping coefficient for S2 Glass (kg/s)	$1.74 \times 10^{-23}$
$c_{pzt}$	Damping coefficient for PZT (kg/s)	$9.37 \times 10^{-15}$
$s^E$	Elastic compliance (1/Pa)	$1.51 \times 10^{-6}$
$d_{\pm}$	<b>Piezoelectric coupling coefficient for <math>\alpha = \pm</math> (m/V)</b>	$5.38 \times 10^{-4}$
$\epsilon_R^{\pm}$	<b>Remanent strain for <math>\alpha = \pm</math> (%)</b>	1
$\epsilon_R^{90}$	Remanent strain for $\alpha = 90$ (%)	$4.89 \times 10^{-22}$
$P_R^{\pm}$	<b>Remanent polarization for <math>\alpha = \pm</math> (C/m<sup>2</sup>)</b>	0.01
$\chi^{\sigma}$	Ferroelectric susceptibility (F/m)	$-7.12 \times 10^{-23}$
$\tau_{90}$	Relaxation time for 90° switching (s)	$8.87 \times 10^{-8}$
$\tau_{180}$	Relaxation time for 180° switching (s)	$6.87 \times 10^{-10}$
$\gamma_{pzt}$	<b>Inverse of relative thermal energy (m<sup>3</sup>/J)</b>	0.08

The method is only able to select a subset of  $n$  parameters from the full parameter set. We can use the rank of the covariance matrix with all of the parameters to choose  $n$ . The method calculates  $\alpha(q_I)$  for all  $\binom{p}{n}$  subsets of the parameters. We used Algorithm 2 from [2] to determine the set of size  $n$  that minimize the asymptotic standard error.

We again use a finite-difference technique to approximate the partial derivatives with a step size of 0.01% of the nominal value. We do not need to scale the derivatives, because we

divide by the parameter value when computing the coefficients of variation. The numerical rank of  $\chi^T \chi$  with all of the parameters is five. Table 3.3 displays the identifiable subset of parameters given the data for sets of size  $n = 1, \dots, 5$ . The subsets of size  $n = 1, 2, 3$  are all subsets from the scaled parameter subset selection results from Section 3.2.3. The set of size four has three parameters from the scaled subset selection results,  $\varepsilon_R^\pm$ ,  $P_R^\pm$ , and  $\gamma_{pzt}$ , but also contains  $\tau_{90}$  which is not listed as one of the parameters selected from Section 3.2.3. However,  $\tau_{90}$  was one of the last parameters removed from the set and its associated eigenvalue is  $8.87 \times 10^{-8}$ , which is on the order of the square root of machine epsilon. The subset of size five did not have any parameters from the scaled subset selection

1. Pre-determine the nominal parameter values,  $q_0$ , and error variance

$$\sigma_0^2 = \frac{1}{N-p} \sum_{k=1}^N (Y_k - f(t_k; q_0))^2.$$

2. Calculate

$$\widehat{V}(\hat{q}_I) = \sigma_0^2 (\chi(\hat{q}_I)^T \chi(\hat{q}_I))^{-1}$$

where

$$\chi(\hat{q}_I) = \begin{bmatrix} \frac{\partial f}{\partial q_{i_1}}(t_1, \hat{q}_I) & \cdots & \frac{\partial f}{\partial q_m}(t_1, \hat{q}_{i_n}) \\ \vdots & \ddots & \vdots \\ \frac{\partial f}{\partial q_{i_1}}(t_N, \hat{q}_I) & \cdots & \frac{\partial f}{\partial q_m}(t_N, \hat{q}_{i_n}) \end{bmatrix}.$$

3. Compute the coefficients of variation,

$$v_j(\hat{q}_I) = \frac{\sqrt{V(\hat{q}_I)_{j,j}}}{(\hat{q}_I)_j}, \text{ for } j = 1, \dots, n$$

4. Calculate the sensitivity score,

$$\alpha(q_I) = \|\nu(q_I)\|_2,$$

5. Repeat 2-4 for all subsets of size  $n$  where the rank of  $\chi(\hat{q}_I) = n$  to find the smallest  $\alpha(q_I)$ .

**Algorithm 2:** Banks, et al, parameter subset selection algorithm from [2] where  $N$  is the size of the data set and  $n$  is the size of the desired subset.

**Table 3.3** Identifiable subset of parameters given the data for sets of size  $n = 1, \dots, 5$  with unscaled partial derivatives.

Parameter	Description	1	2	3	4	5
$\gamma$	Air damping coefficient (kg/s)					
$\rho_{cf}$	Density of the CF layer (kg/m <sup>3</sup> )					X
$\rho_s$	Density of the S2 Glass (kg/m <sup>3</sup> )					X
$\rho_{pzt}$	Density of the PZT actuators (kg/m <sup>3</sup> )					X
$Y_{cf}$	Elastic modulus of CF (Pa)					X
$Y_s$	Elastic modulus of S2 Glass (Pa)					
$c_{cf}$	Damping coefficient for CF (kg/s)					
$c_s$	Damping coefficient for S2 Glass (kg/s)					
$c_{pzt}$	Damping coefficient for PZT (kg/s)					X
$s^E$	Elastic compliance (1/Pa)					
$d_{\pm}$	Piezoelectric coupling coefficient for $\alpha = \pm$ (m/V)	X				
$\epsilon_R^{\pm}$	Remanent strain for $\alpha = \pm$ (%)		X	X	X	
$\epsilon_R^{90}$	Remanent strain for $\alpha = 90$ (%)					
$P_R^{\pm}$	Remanent polarization for $\alpha = \pm$ (C/m <sup>2</sup> )			X	X	
$\chi^{\sigma}$	Ferroelectric susceptibility (F/m)					
$\tau_{90}$	Relaxation time for 90° switching (s)				X	
$\tau_{180}$	Relaxation time for 180° switching (s)					
$\gamma_{pzt}$	Inverse of relative thermal energy (m <sup>3</sup> /J)		X	X	X	

results. This is likely due to sensitivity of the covariance matrices of size five. This helps verify the results from the scaled subset selection, because  $d_{\pm}$ ,  $\gamma_{pzt}$ ,  $P_R^{\pm}$ , and  $\epsilon_R^{\pm}$  were all determined to be in an identifiable subset for a set of size four or less.

We also tested using the scaled finite-difference technique to approximate derivatives with a step size of  $h = 1 \times 10^{-4}$ . Although we do not need to use the scaled derivatives from Section 3.2.3, we wanted to test the method with the scaled derivatives to see if it would produce different results. The rank of  $\chi^T \chi$  with all of the parameters is 11, but

we will only report the  $n = 1, \dots, 5$ , since the rank of non-scaled  $\chi^T \chi$  was 5. The larger rank is likely due using the scaled finite-difference technique from Section 3.2.3. Scaled finite-difference technique produces relative derivatives not physical derivatives which are necessary to determine the size of the identifiable set. Table 3.4 displays the identifiable subset of parameters given the data for sets of size  $n = 1, \dots, 5$ . The subsets of size  $n = 1, 2, 4$  are all subsets from the scaled parameter subset selection results from Section 3.2.3. When  $n = 5$ , the parameter  $Y_{cf}$  was included along with the parameters from the scaled subset selection results,  $d_{\pm}$ ,  $\gamma_{pzt}$ ,  $P_R^{\pm}$ , and  $\epsilon_R^{\pm}$ . However, it also selected  $c_s$  which has one of the smallest relative eigenvalues associated with it from Section 3.2.3. This may be due to the correlation of the parameters which made other sets not full rank or have larger standard error. Overall, the results are consistent with the scaled subset selection results. We conclude that parameters,  $d_{\pm}$ ,  $\gamma_{pzt}$ ,  $P_R^{\pm}$ , and  $\epsilon_R^{\pm}$  are identified as an identifiable set of parameters and corroborate the results from the scaled subset selection.

### 3.4 Pearson Correlation

Pearson correlation discussed in [41], quantifies the correlation between two random variables. It compares the covariance of the two random variables and each of their standard deviations. For random variables  $X$  and  $Y$ , the Pearson correlation is given by

$$\rho(X, Y) = \frac{\text{cov}(X, Y)}{\sigma_X \sigma_Y}.$$

The values are on the interval  $[-1, 1]$  where  $-1$  and  $1$  represent a negative and positive linear algebraic relationship and  $0$  represents two random variables with no correlation.

The quantity of interest must be a scalar value. We considered the  $L_2$  norm of the tip displacement,  $y(t)$ ,

$$Y = \sqrt{\int_0^T y(t)^2 dt},$$

which will be one random variable. The other random variable is a parameter,  $q_i$ . Table 3.5 displays the results for each parameter. We report the results from 10,000 samples out of uniform distributions with support of  $\pm 20\%$  of the nominal parameter values to compute the correlation values. We also tested 5,000 samples to compare for convergence analysis. The three parameters with the largest absolute value for its Pearson correlation are also

**Table 3.4** Identifiable subset of parameters given the data for sets of size  $n = 1, \dots, 5$  with the scaled partial derivatives.

Parameter	Description	1	2	3	4	5
$\gamma$	Air damping coefficient (kg/s)					
$\rho_{cf}$	Density of the CF layer (kg/m <sup>3</sup> )					
$\rho_s$	Density of the S2 Glass (kg/m <sup>3</sup> )					
$\rho_{pzt}$	Density of the PZT actuators (kg/m <sup>3</sup> )					
$Y_{cf}$	Elastic modulus of CF (Pa)					X
$Y_s$	Elastic modulus of S2 Glass (Pa)					
$c_{cf}$	Damping coefficient for CF (kg/s)					
$c_s$	Damping coefficient for S2 Glass (kg/s)			X		
$c_{pzt}$	Damping coefficient for PZT (kg/s)					
$s^E$	Elastic compliance (1/Pa)					
$d_{\pm}$	Piezoelectric coupling coefficient for $\alpha = \pm$ (m/V)	X		X	X	X
$\epsilon_R^{\pm}$	Remanent strain for $\alpha = \pm$ (%)		X		X	X
$\epsilon_R^{90}$	Remanent strain for $\alpha = 90$ (%)					
$P_R^{\pm}$	Remanent polarization for $\alpha = \pm$ (C/m <sup>2</sup> )			X	X	X
$\chi^{\sigma}$	Ferroelectric susceptibility (F/m)					
$\tau_{90}$	Relaxation time for 90° switching (s)					
$\tau_{180}$	Relaxation time for 180° switching (s)					
$\gamma_{pzt}$	Inverse of relative thermal energy (m <sup>3</sup> /J)		X		X	X

selected using scaled subset selection,  $d_{\pm}$ ,  $\gamma_{pzt}$ , and  $\epsilon_R^{\pm} \cdot P_R^{\pm}$ , is the sixth most correlated parameter with  $Y_{cf}$  and  $s^E$  being more sensitive. This may be due to the fact that our quantity of interest is the  $L_2$  norm of the tip displacement instead of just the tip displacement. The Pearson correlation results support the results from the scaled subset selection by identifying,  $d_{\pm}$ ,  $\gamma_{pzt}$ ,  $P_R^{\pm}$ , and  $\epsilon_R^{\pm}$  to be influential parameters. Note, the other parameter values are at least an order of magnitude smaller than the six largest values.



**Table 3.5** The Pearson correlation values for  $Y = \sqrt{\int_0^T y(t; q)^2 dt}$  and the parameter  $X$  with the identifiable parameters from the scaled subset selection results in bold.

Parameter	Description	$\rho(X, Y)$
$\gamma$	Air damping coefficient (kg/s)	0.0077
$\rho_{cf}$	Density of the CF layer (kg/m <sup>3</sup> )	-0.0158
$\rho_s$	Density of the S2 Glass (kg/m <sup>3</sup> )	0.0053
$\rho_{pzt}$	Density of the PZT actuators (kg/m <sup>3</sup> )	0.0141
$Y_{cf}$	<b>Elastic modulus of CF (Pa)</b>	<b>-0.2528</b>
$Y_s$	Elastic modulus of S2 Glass (Pa)	-0.0059
$c_{cf}$	Damping coefficient for CF (kg/s)	0.0101
$c_s$	Damping coefficient for S2 Glass (kg/s)	-0.0135
$c_{pzt}$	Damping coefficient for PZT (kg/s)	0.0051
$s^E$	<b>Elastic compliance (1/Pa)</b>	<b>-0.2753</b>
$d_{\pm}$	<b>Piezoelectric coupling coefficient for <math>\alpha = \pm</math> (m/V)</b>	<b>0.6305</b>
$\epsilon_R^{\pm}$	<b>Remanent strain for <math>\alpha = \pm</math> (%)</b>	<b>0.5650</b>
$\epsilon_R^{90}$	Remanent strain for $\alpha = 90$ (%)	-0.0057
$P_R^{\pm}$	<b>Remanent polarization for <math>\alpha = \pm</math> (C/m<sup>2</sup>)</b>	<b>-0.1781</b>
$\chi^{\sigma}$	Ferroelectric susceptibility (F/m)	-0.0108
$\tau_{90}$	Relaxation time for 90° switching (s)	-0.0542
$\tau_{180}$	Relaxation time for 180° switching (s)	-0.0023
$\gamma_{pzt}$	<b>Inverse of relative thermal energy (m<sup>3</sup>/J)</b>	<b>-0.3024</b>

### 3.5 Active Subspaces

The active subspace is not a global sensitivity method, but can be used to create a global sensitivity metric through activity scores [10]. Active subspace methods determine an influential subspace of the parameter space. Note that the active subspace consist of linear combinations of parameters. We determine the set of influential parameters by calculating activity scores for the parameter.

As in [9], we begin our discussion of active subspaces by defining the matrix,

$$C = \int (\nabla_q f)(\nabla_q f)^T \rho dq,$$

as the average of the outer products of the gradient over the parameter space. Here  $f(q)$  is the quantity of interest and  $\rho$  is the probability density for our parameters. We note that  $C$  is symmetric, positive semi-definite, which implies that it has a eigenvalue decomposition with real eigenvalues,

$$C = W \Lambda W^T,$$

where  $W$  is an orthogonal matrix whose columns are eigenvectors. We can exploit the eigenstructure of  $C$  to define active and inactive subspaces. The eigenvalue matrix can be separated into

$$\Lambda = \begin{bmatrix} \Lambda_1 & \\ & \Lambda_2 \end{bmatrix},$$

where  $\lambda_1 \gg \lambda_2$  for  $\lambda_1 \in \Lambda_1$  and  $\lambda_2 \in \Lambda_2$ . Similarly for the eigenvector matrix can be separated as

$$W = \begin{bmatrix} W_1 & W_2 \end{bmatrix}.$$

We then define the active subspace as  $W_1 \in \mathbb{R}^{p \times n}$  and the inactive subspaces as  $W_2 \in \mathbb{R}^{p \times (p-n)}$ . We then create new variables

$$y = W_1^T x \in \mathbb{R}^n \text{ and } z = W_2^T x \in \mathbb{R}^{p-n}.$$

Note, we can express

$$x = W_1 y + W_2 z,$$

where the  $W_1$  direction of  $x$  has a much larger influence on  $f(x)$ . To decide where to separate the eigenvalues, we select the first difference in three orders of magnitude between eigenvalues to separate the active and inactive subspaces.

In some cases, we can directly compute  $C$  and then perform the eigenvalue decomposition. However, in many cases, the analytical gradient cannot be computed analytically [8]. Also, if  $p$  is large, then the integral may be too computationally intensive to compute. We use a Monte Carlo method to approximate the integral and compute the active subspace. We implemented Algorithm 3 from [9] to determine the active subspace. If the analytic gra-

1. Draw independent samples,  $q_{k=1}^M$ , from the density  $\rho$ .

2. Compute

$$\nabla_q f_k = \nabla_q f(q_k) \quad \forall \quad k \in 1, \dots, M.$$

3. Take the SVD of

$$\frac{1}{\sqrt{M}} [\nabla_q f_1 \cdots \nabla_q f_M] = \tilde{W} \sqrt{\tilde{\Lambda}} \tilde{V}$$

**Algorithm 3:** The active subspace algorithm from [9].

dient is unavailable, we can use the finite-difference method for the scaled derivative as in Section 3.2.3 to compute the gradient. Note we could use the gradient-free construction of active subspace method outlined in [8]. When the distribution,  $\rho$ , is unknown, one typically samples from a uniform distribution.

To determine the influential parameters, we need to define a global sensitivity metric. We use activity scores as discussed in [10]. An activity score is computed for each parameters using the relation

$$\alpha_{q_k} = \sum_{j=1}^n \lambda_j w_{k,j}^2.$$

Here  $\lambda_j$  is the  $j^{th}$  eigenvalue  $\Lambda_1$  and  $w_{k,j}$  is the entry in the  $k^{th}$  row and  $j^{th}$  column of  $W_1$ . Note that the square is used to remove the information of the sign from the metric. As proved in [10], activity scores are bounded above by

$$\alpha_{q_k} \leq \int \left( \frac{\partial f}{\partial q_k}(q) \right)^2 \rho(q) dq$$

a global derivative-based sensitivity method that averages local sensitivities. The global derivative-based method was studied in [38]. These two methods produce comparable rankings for the parameters' sensitivities. The parameters with the larger activity scores are the more influential parameters. This provides a system to determine the non-influential parameters.

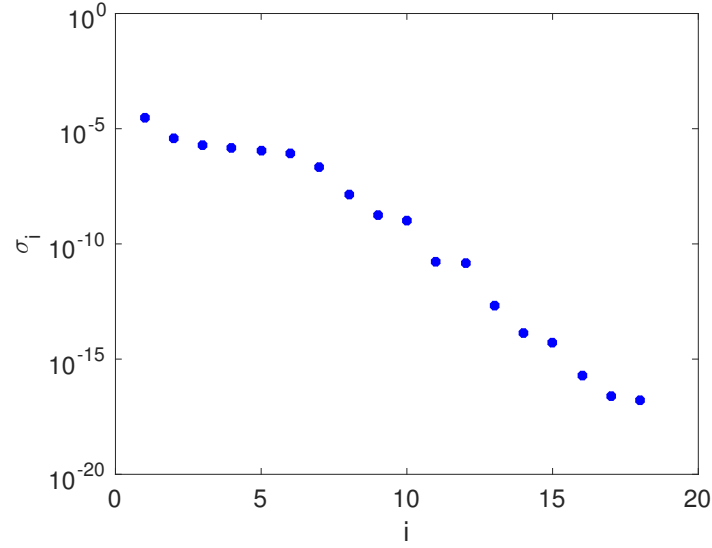


**Figure 3.2** The singular values from the activity subspace results, which are used to determine the active and inactive subspaces.

It is necessary to have a scalar quantity of interest, so we considered

$$h(\theta) = \sqrt{\int_0^T y(t; \theta)^2 dt}.$$

We used  $m = 1,000$  samples to compute the results. We used a uniform distribution with a support of  $\pm 25\%$  of the nominal parameter values. We display our results in Figure 3.2 and Table 3.6. The singular values at most drop two orders of magnitude at a time, so there is no clear cut-off from the active subspace and the non-active subspace. We decide to include all of the eigenvectors in the active subspaces since we are only looking for a ranking of the parameters' influence and not developing a surrogate model. The activity scores rank the top six influential parameters in order as  $d_{\pm}$ ,  $\epsilon_R^{\pm}$ ,  $\gamma_{pzt}$ ,  $P_R^{\pm}$ ,  $s^E$ , and  $Y_{cf}$ . We observe that the four parameters with the largest activity scores are the same set of parameters that were selected from results from scaled subset selection in Section 3.2.3,  $d_{\pm}$ ,  $\gamma_{pzt}$ ,  $P_R^{\pm}$ , and  $\epsilon_R^{\pm}$ .  $s^E$ , and  $Y_{cf}$  were identified as influential by Pearson correlation, so the results from the activity scores support the results from the other methods; especially the scaled subset selection.

**Table 3.6** The activity scores of the parameters for the quantity of interest  $h(\theta) = \sqrt{\int_0^T y(t; \theta)^2 dt}$ .

Parameter	Description	Activity Scores
$\gamma$	Air damping coefficient (kg/s)	$9.57 \times 10^{-24}$
$\rho_{cf}$	Density of the CF layer (kg/m <sup>3</sup> )	$1.67 \times 10^{-16}$
$\rho_s$	Density of the S2 Glass (kg/m <sup>3</sup> )	$1.05e \times 10^{-17}$
$\rho_{pzt}$	Density of the PZT actuators (kg/m <sup>3</sup> )	$3.16 \times 10^{-17}$
$Y_{cf}$	<b>Elastic modulus of CF (Pa)</b>	$6.02 \times 10^{-11}$
$Y_s$	Elastic modulus of S2 Glass (Pa)	$1.10 \times 10^{-14}$
$c_{cf}$	Damping coefficient for CF (kg/s)	$1.82 \times 10^{-22}$
$c_s$	Damping coefficient for S2 Glass (kg/s)	$2.66 \times 10^{-27}$
$c_{pzt}$	Damping coefficient for PZT (kg/s)	$3.16 \times 10^{-22}$
$s^E$	<b>Elastic compliance (1/Pa)</b>	$6.22 \times 10^{-11}$
$d_{\pm}$	<b>Piezoelectric coupling coefficient for <math>\alpha = \pm</math> (m/V)</b>	$3.33 \times 10^{-10}$
$\epsilon_R^{\pm}$	<b>Remanent strain for <math>\alpha = \pm</math> (%)</b>	$2.75 \times 10^{-10}$
$\epsilon_R^{90}$	Remanent strain for $\alpha = 90$ (%)	$5.78 \times 10^{-33}$
$P_R^{\pm}$	<b>Remanent polarization for <math>\alpha = \pm</math> (C/m<sup>2</sup>)</b>	$2.83 \times 10^{-11}$
$\chi^{\sigma}$	Ferroelectric susceptibility (F/m)	$2.05 \times 10^{-36}$
$\tau_{90}$	Relaxation time for 90° switching (s)	$2.45 \times 10^{-11}$
$\tau_{180}$	Relaxation time for 180° switching (s)	$5.16 \times 10^{-17}$
$\gamma_{pzt}$	<b>Inverse of relative thermal energy (m<sup>3</sup>/J)</b>	$7.58 \times 10^{-11}$

### 3.6 Morris Screening

Morris screening averages elementary effects over the parameter space to yield a quasi-global sensitivity measure. To calculate the elementary effects, we will use the scaled derivative as defined in Section 3.2.3,

$$d_i^j = \frac{\partial h(\theta^j)}{\partial \theta_i} \approx \frac{h(\theta_1^j, \dots, \theta_i^j + \Delta, \dots, \theta_p^j) - h(\theta_1^j, \dots, \theta_p^j)}{\Delta},$$

where  $\theta^j$  is the  $j^{th}$  parameter sample and  $\Delta$  is the step size. We take  $M$  samples and compute the elementary effects,  $d_i^j$ , for each parameter at each samples. Then, we calculate the sensitivity measures for each parameter,  $\theta_i$ , by computing the sample mean and variance

$$\mu_i^* = \frac{1}{M} \sum_{j=1}^M |d_i^j|,$$

$$\sigma_i^2 = \frac{1}{M-1} \sum_{j=1}^M (d_i^j - \mu_i)^2,$$

of the elementary effects. Here

$$\mu_i = \frac{1}{M} \sum_{j=1}^M d_i^j.$$

The parameters that are more sensitive are the ones with the larger  $\mu_i^*$  and  $\sigma_i$  values. Note that Morris screening produce a relative measure of sensitivity, so it only produces a ranking system for the parameters.

We need the quantity of interest for our model to be a scalar value, so we employ

$$h(\theta) = \sqrt{\int_0^T y(t; \theta)^2 dt},$$

where  $y(t; \theta)$  is the tip displacement. We compile our results in Table 3.7. We report the results from 1,000 samples out of uniform distributions with support of  $\pm 25\%$  of the nominal parameter values to compute the elementary effects. Morris screening determines the non-influential parameters, which are the parameters with both a small mean and standard deviation of there elementary effects. The parameters that are determined to be influential are the ones that we should allow to vary in further analysis. Therefore, we can conclude that parameters  $d_{\pm}$ ,  $\epsilon_R^{\pm}$ ,  $\gamma_{pzt}$ ,  $P_R^{\pm}$ ,  $s^E$ , and  $Y_{cf}$  are the six most influential parameters since the parameters' elementary effects have the largest mean and standard deviation. This supports the results of the other methods. The parameters from subset selection,  $d_{\pm}$ ,  $\epsilon_R^{\pm}$ ,  $\gamma_{pzt}$ , and  $P_R^{\pm}$ , were determined to be the six most influential parameters. This again supports the results from Section 3.2.3.

**Table 3.7** The Morris screening's sensitivity measures for the parameters with the quantity of interest  $h(\theta) = \sqrt{\int_0^T y(t; \theta)^2 dt}$ .

Parameter	Description	$\mu^*$	$\sigma$
$\gamma$	Air damping coefficient (kg/s)	$3.04 \times 10^{-12}$	$5.81 \times 10^{-13}$
$\rho_{cf}$	Density of the CF layer (kg/m <sup>3</sup> )	$1.27 \times 10^{-8}$	$2.47 \times 10^{-9}$
$\rho_s$	Density of the S2 Glass (kg/m <sup>3</sup> )	$3.18 \times 10^{-9}$	$6.14 \times 10^{-10}$
$\rho_{pzt}$	Density of the PZT actuators (kg/m <sup>3</sup> )	$5.51 \times 10^{-9}$	$1.11 \times 10^{-9}$
$Y_{cf}$	<b>Elastic modulus of CF (Pa)</b>	$7.64 \times 10^{-6}$	$1.36 \times 10^{-6}$
$Y_s$	Elastic modulus of S2 Glass (Pa)	$1.03 \times 10^{-7}$	$2.10 \times 10^{-8}$
$c_{cf}$	Damping coefficient for CF (kg/s)	$1.33 \times 10^{-11}$	$2.23 \times 10^{-12}$
$c_s$	Damping coefficient for S2 Glass (kg/s)	$5.06 \times 10^{-14}$	$9.88 \times 10^{-15}$
$c_{pzt}$	Damping coefficient for PZT (kg/s)	$1.75 \times 10^{-11}$	$2.91 \times 10^{-12}$
$s^E$	<b>Elastic compliance (1/Pa)</b>	$7.76 \times 10^{-6}$	$1.44 \times 10^{-6}$
$d_{\pm}$	<b>Piezoelectric coupling coefficient (m/V)</b>	$1.82 \times 10^{-5}$	$1.43 \times 10^{-6}$
$\epsilon_R^{\pm}$	<b>Remanent strain for <math>\alpha = \pm</math> (%)</b>	$1.64 \times 10^{-5}$	$2.49 \times 10^{-6}$
$\epsilon_R^{90}$	Remanent strain for $\alpha = 90$ (%)	$7.53 \times 10^{-17}$	$2.56 \times 10^{-17}$
$P_R^{\pm}$	<b>Remanent polarization for <math>\alpha = \pm</math> (C/m<sup>2</sup>)</b>	$4.93 \times 10^{-6}$	$3.17 \times 10^{-6}$
$\chi^{\sigma}$	Ferroelectric susceptibility (F/m)	$1.48 \times 10^{-17}$	$1.93 \times 10^{-17}$
$\tau_{90}$	Relaxation time for 90° switching (s)	$1.48 \times 10^{-6}$	$5.03 \times 10^{-7}$
$\tau_{180}$	Relaxation time for 180° switching (s)	$5.96 \times 10^{-9}$	$4.03 \times 10^{-9}$
$\gamma_{pzt}$	<b>Inverse of relative thermal energy (m<sup>3</sup>/J)</b>	$8.30 \times 10^{-6}$	$2.65 \times 10^{-6}$

### 3.7 Conclusion of Sensitivity Analysis

Some of the differences between the results of the sensitivity analysis methods is due to the different quantity of interests. The two local sensitivity measures do not need to have a scalar quantity of interest as is the case for global methods. Also, Morris screening assumes that the parameters are independent, but for this problem they are not. For our problem, we observe that violating the independent parameters assumption did not produce incorrect

results, because the methods all produce similar results. Other global methods like Sobol indices [37], also have the same assumption of independence. Shown in [21], violating the independence assumption for variance based-methods causes failure of the algorithm. We note, however, that the distribution in Morris screening dictates how we sample rather than apportion variances, which is typically less pernicious.

After analyzing the results from all methods, there are six parameters which stand out as the identifiable set,  $d_{\pm}$ ,  $\epsilon_R^{\pm}$ ,  $\gamma_{pzt}$ ,  $P_R^{\pm}$ ,  $s^E$ , and  $Y_{cf}$ . We decided to have four identifiable parameters,  $d_{\pm}$ ,  $\gamma_{pzt}$ ,  $P_R^{\pm}$ , and  $\epsilon_R^{\pm}$ , because the two local methods selected these four as the identifiable set. Note that the results of the local sensitivity methods were supported by all of the global methods. We choose to consider only four parameters, because the rank of the sensitivity matrix from the parameter subset selection was five, but only had reasonable results for four parameters. Table 3.8 displays the results of all of the methods in a single table for easy comparison. We will use the parameters,  $d_{\pm}$ ,  $\gamma_{pzt}$ ,  $P_R^{\pm}$ , and  $\epsilon_R^{\pm}$ , in our analysis for the remaining chapters. Although the results indicate five or six influential parameter, when we ran chains for five parameters, they were not converging. In future work, we will investigate why the chains for five parameters are not converging and further our attempt to add  $s^E$ , or  $Y_{cf}$  to the identifiable set of parameters.



**Table 3.8** Local and Global sensitivity results. Parameters used for uncertainty quantification are bold.

q	Description	$\lambda$	$n_4$	$\rho$	A.S.	$\mu^*$	$\sigma$
$\gamma$	Air damping coefficient (kg/s)	$8.21 \times 10^{-23}$		0.01	$5.96 \times 10^{-15}$	$3.04 \times 10^{-12}$	$5.81 \times 10^{-13}$
$\rho_{cf}$	Density of the CF layer (kg/m <sup>3</sup> )	$-4.31 \times 10^{-18}$		-0.02	$7.65 \times 10^{-10}$	$1.27 \times 10^{-8}$	$2.47 \times 10^{-9}$
$\rho_s$	Density of the S2 Glass (kg/m <sup>3</sup> )	$1.25 \times 10^{-13}$		0.01	$6.05 \times 10^{-11}$	$3.17 \times 10^{-9}$	$6.14 \times 10^{-10}$
$\rho_{pzt}$	Density of the PZT actuators (kg/m <sup>3</sup> )	$2.46 \times 10^{-13}$		0.01	$2.13 \times 10^{-10}$	$5.51 \times 10^{-9}$	$1.11 \times 10^{-9}$
$Y_{cf}$	Elastic modulus of CF (Pa)	$3.96 \times 10^{-8}$		-0.25	$3.22 \times 10^{-6}$	$7.64 \times 10^{-6}$	$1.36 \times 10^{-6}$
$Y_s$	Elastic modulus of S2 Glass (Pa)	$-3.17 \times 10^{-19}$		-0.01	$1.47 \times 10^{-8}$	$1.03 \times 10^{-7}$	$2.10 \times 10^{-8}$
$c_{cf}$	Damping coefficient for CF (kg/s)	$3.40 \times 10^{-18}$		0.01	$7.85 \times 10^{-14}$	$1.33 \times 10^{-11}$	$2.23 \times 10^{-12}$
$c_s$	Damping coefficient for S2 Glass (kg/s)	$1.74 \times 10^{-23}$		-0.01	$2.04 \times 10^{-16}$	$5.06 \times 10^{-14}$	$9.88 \times 10^{-15}$
$c_{pzt}$	Damping coefficient for PZT (kg/s)	$9.37 \times 10^{-15}$		0.01	$1.60 \times 10^{-13}$	$1.75 \times 10^{-11}$	$2.91 \times 10^{-12}$
$s^E$	Elastic compliance (1/Pa)	$1.51 \times 10^{-6}$		-0.28	$3.22 \times 10^{-6}$	$7.76 \times 10^{-6}$	$1.44 \times 10^{-6}$
$d_{\pm}$	<b>Piezoelectric coupling coefficient (m/V)</b>	$5.38 \times 10^{-4}$	<b>X</b>	0.63	$1.26 \times 10^{-5}$	$1.82 \times 10^{-5}$	$1.43 \times 10^{-6}$
$\epsilon_R^{\pm}$	<b>Remanent strain for <math>\alpha = \pm</math> (%)</b>	1	<b>X</b>	0.57	$1.04 \times 10^{-5}$	$1.64 \times 10^{-5}$	$2.49 \times 10^{-6}$
$\epsilon_R^{90}$	Remanent strain for $\alpha = 90$ (%)	$4.89 \times 10^{-22}$		-0.01	$2.26 \times 10^{-17}$	$7.53 \times 10^{-17}$	$2.56 \times 10^{-17}$
$P_R^{\pm}$	<b>Remanent polarization for <math>\alpha = \pm</math> (C/m<sup>2</sup>)</b>	0.01	<b>X</b>	-0.18	$3.47 \times 10^{-6}$	$4.93 \times 10^{-6}$	$3.17 \times 10^{-6}$
$\chi^{\sigma}$	Ferroelectric susceptibility (F/m)	$-7.12 \times 10^{-23}$		-0.01	$1.86 \times 10^{-17}$	$1.48 \times 10^{-17}$	$1.93 \times 10^{-17}$
$\tau_{90}$	Relaxation time for 90° switching (s)	$8.87 \times 10^{-8}$		-0.05	$3.55 \times 10^{-7}$	$1.48 \times 10^{-6}$	$5.03 \times 10^{-7}$
$\tau_{180}$	Relaxation time for 180° switching (s)	$6.87 \times 10^{-10}$		-0.00	$1.83 \times 10^{-9}$	$5.96 \times 10^{-9}$	$4.03 \times 10^{-9}$
$\gamma_{pzt}$	<b>Inverse of relative thermal energy (m<sup>3</sup>/J)</b>	0.08	<b>X</b>	-0.30	$4.72 \times 10^{-6}$	$8.30 \times 10^{-6}$	$2.65 \times 10^{-6}$

## CHAPTER

# 4

# UNCERTAINTY QUANTIFICATION

### 4.1 Bayesian Inference

The goal of Bayesian inference is to compute posterior distributions for the parameters given data. We employ the statistical model

$$Y_k = f(t_k, Q) + \epsilon_k \quad k = 1, \dots, n \quad (4.1)$$

where  $Y_k$ ,  $Q$ , and  $\epsilon_k$  are random variables that represent the measurements, parameters, and measurement errors, respectively. We will assume that  $\epsilon_k \sim N(0, \sigma^2)$  for some fixed error variance  $\sigma^2$  and they are independent and identically distributed. To compute the posterior distribution for  $q$ , a realization of  $Q$ , given  $y$ , a set of realizations for  $Y_k$ , we employ Bayes' Theorem

$$\pi(q|y) = \frac{\pi(y|q)\pi_0(q)}{\pi(y)} = \frac{\pi(y|q)\pi_0(q)}{\int_{\mathbb{R}^p} \pi(y|q)\pi_0(q)dq},$$

where  $p$  is the number of parameters and  $\pi_0(q)$  is a prior distribution for  $Q$ . We note that for the statistical model (4.1) the likelihood function is

$$\pi(y|q) = \frac{1}{(2\pi\sigma^2)^{\frac{n}{2}}} e^{\frac{-SS(q)}{2\sigma^2}},$$

where

$$SS(q) = \sum_{k=1}^n [y_k - f_k(q)]^2.$$

Calculating the posterior distributions analytically is typically infeasible. Therefore, we will use a sampling-based method to calculate the posterior distributions called Delayed Rejection Adaptive Metropolis. This methods allow  $p$  to be large and the likelihood and prior to be of any form.

#### 4.1.1 DRAM

We used the Delayed Rejection Adaptive Metropolis algorithm (DRAM) to perform Bayesian inference [16]. The algorithm is a variation of the Metropolis algorithm with two additional components. The delayed rejection improves the acceptance rate of the samples. If a sample is rejected, it samples another set of parameters from a tighter proposal distribution and compares it with both the previous accepted sample and the sample that was just rejected. The adaptive part of the algorithm means the covariance matrix for the parameter distribution is updated while sampling. We used an implementation reported in [20]. The DRAM algorithm is outlined in Algorithm 4 from [16] for a chain with  $M$  samples and a uniform prior. We note that  $J(q^*|q^{k-1})$  is the proposal distribution  $N(q^{k-1}|V)$ . and we can continue to run delayed rejection with smaller and smaller  $\gamma_2$ , but we used only one delayed rejection step.

In step (b) of Algorithm 4, we chose the proposal distributions,  $N(q^{k-1}|V)$ , to improve the efficiency of DRAM. Sampling around the previous sample,  $q^{k-1}$ , proposes a sample,  $q^*$ , that is appropriately scaled. The covariance matrix ensures that the variance are not too large or small. If the variance of the proposal distribution is too small, then the acceptance rate is too large and the space is not adequately explored. In contrast, if the variance is too large, chain will stagnate due to a large rejection rate. Additionally, the covariance matrix incorporates the underlying correlation structure of the parameters to improve the proposed parameters [34].

1. Set design parameters  $M$ ,  $n_s$ ,  $\sigma_s^2$ ,  $s_p$ ,  $k_0$ , and  $\gamma_2$
2. Determine initial values for  $q_0$ , the error variance  $s_0^2$ , and covariance matrix  $V$  via a least squares fit to the data.
3. For  $k = 1, \dots, M$ 
  - (a) Sample  $z_k \sim N(0, I)$
  - (b) Construct  $q^* = q^{k-1} + \text{chol}(V)z_k$
  - (c) Set  $SS_{q^*} = SS(q^*)$
  - (d) Sample  $d_\alpha \sim U(0, 1)$
  - (e) Compute

$$\alpha(q^*|q^{k-1}) = \min\left(1, e^{\frac{-[SS_{q^*} - SS_{k-1}]}{2s_{k-1}^2}}\right)$$

- (f) If  $\alpha > d_\alpha$ , set  $q^k = q^*$  and  $SS_k = SS_{q^*}$ ; else, delayed rejection:

- i. Sample  $z_k \sim N(0, I)$
- ii. Construct  $q^{*2} = q^{k-1} + \gamma_2 \text{chol}(V)z_k$
- iii. Compute

$$\alpha_2(q^{*2}|q^{k-1}) = \min\left(1, \frac{\pi(q^{*2}|y)J(q^*|q^{*2})(1 - \alpha(q^*|q^{*2}))}{\pi(q^{k-1}|y)J(q^*|q^{k-1})(1 - \alpha(q^*|q^{k-1}))}\right)$$

- iv. Sample  $d_\alpha \sim U(0, 1)$
- v. If  $\alpha_2 > d_\alpha$ , set  $q^k = q^*$  and  $SS_k = SS_{q^*}$ ; else set  $q^k = q^{k-1}$  and  $SS_k = SS_{q^{k-1}}$
- (g) Sample  $s_k^2 \sim \Gamma^{-1}(a(n_s, n), b(SS_k, n_s, \sigma_s^2))$
- (h) If  $\text{mod}(k, k_0) = 1$ , Update  $V = s_p \text{cov}(q^0, \dots, q^k)$

**Algorithm 4:** Delayed Rejection Adaptive Metropolis algorithm from [16].

Algorithm 4 step (f)iii. determines the acceptance probability of the delayed rejection proposal. We achieve this expression by satisfying the detailed balance condition,

$$\pi(q^{k-1}|v)p_{k-1,k} = \pi(q^k|v)p_{k,k-1}, \quad (4.2)$$

where  $q^k = q^{*2}$ . Here the  $p_{k-1,k}$  is the probability of accepting  $q^k$  given  $q^{k-1}$ . We note that before we accept  $q^k$  we must reject  $q^*$ . Therefore, we obtain

$$\begin{aligned} p_{k-1,k} &= P(\text{proposing } q^*)P(\text{rejecting } q^*)P(\text{proposing } q^k)P(\text{accepting } q^k) \\ &= J(q^*|q^{k-1})[1 - \alpha(q^*|q^{k-1})]J_2(q^k|q^{k-1}, q^*)\alpha_2(q^k|q^{k-1}, q^*), \end{aligned} \quad (4.3)$$

where  $J_2$  is the proposal distribution  $N(q^{k-1}\gamma_2|V)$ . A similar formulation is used for  $p_{k,k-1}$ . Substituting (4.3) in the detail balanced condition (4.2) and solving for  $\alpha_2(q^k|q^{k-1}, q^*)$ , yields

$$\alpha_2(q^k|q^{k-1}, q^*) = \min \left( 1, \frac{\pi(q^{*2}|y)J(q^*|q^{*2})(1 - \alpha(q^*|q^{*2}))}{\pi(q^{k-1}|y)J(q^*|q^{k-1})(1 - \alpha(q^*|q^{k-1}))} \right).$$

Here we enforce the natural condition  $\alpha_2(q^k|q^{k-1}, q^*) \leq 1$ .

## 4.2 Uncertainty Propagation

After performing Bayesian inference, which is often termed inverse uncertainty quantification, we want to quantify the uncertainty of our statistical quantity of interest. We accomplish this through uncertainty propagation and constructing credible and prediction intervals. A 95% credible interval is the interval that there is a 95% probability the true value is within the region. The 95% prediction interval is the interval such that if another sample is collected, there is a 95% probability that the data point will be within the bounds. The construction of credible and prediction intervals are created through propagating the parameter and observation uncertainty through the model [34].

There are many methods to propagate uncertainty through the model, that we will not utilize including stochastic Galerkin, collocation, and discrete projection as detailed in [34]. These methods are used to reduce the number of model runs compared to the sampling-based method that we utilized. A sampling-based method is infeasible for complex models with long computation times without a surrogate. For our problem, one model evaluation is on the order of a second, so we can apply a sampling method. We calculated a 95%

credible interval by sampling out of the posterior distributions to calculate  $M$  realizations of the model and used the responses to determine the bounds for the credible interval. To construct the prediction interval, we added the estimated error variance,  $s^2$ , to the credible interval.

### 4.3 Results

We ran Bayesian inference with the four identifiable parameters,  $d_{\pm}$ ,  $\gamma_{pzt}$ ,  $P_R^{\pm}$ , and  $\epsilon_R^{\pm}$ , from Chapter 3. The nominal parameters from Table 2.1 were used as initial values for the identifiable parameters and fixed for the unidentifiable parameters. We ran the algorithm for 70,000 samples. We used 10,000 samples as burn-in and the remaining 60,000 were used as samples to create the posterior distribution. Burn-in are the samples that are taken to ensure that the algorithm has converged to the posterior distribution before taking samples. Figure 4.1 displays the chains, pairwise plots, and marginal densities created from the results. The last 10,000 samples were used to create the plots in Figure 4.1. The chains have explored the parameter space and are well mixed, so the chains have converged. We could also use the Gelman-Rubin method from [15] to support that the chains have converged, however we did not perform the analysis. From the pairwise plots, we conclude that the parameters are correlated.

We then took the results and propagated the quantified uncertainty through the model to create 95% prediction and credible intervals of the quantity of interest [20]. We used 1,000 of the final 10,000 samples from the DRAM results to calculate the intervals. Figure 4.2 displays the prediction and credible intervals. We plotted the intervals with respect to time. Since range of the prediction and credible intervals are small using this data set, the uncertainty is minimal in the model. The lack of uncertainty is due to the periodic or steady state response. We would expect to observe more uncertainty for an impulse response, because impulse response excites all frequencies causing more uncertainty to be present. We will use the uncertainty analysis to develop more robust and efficient control algorithms.

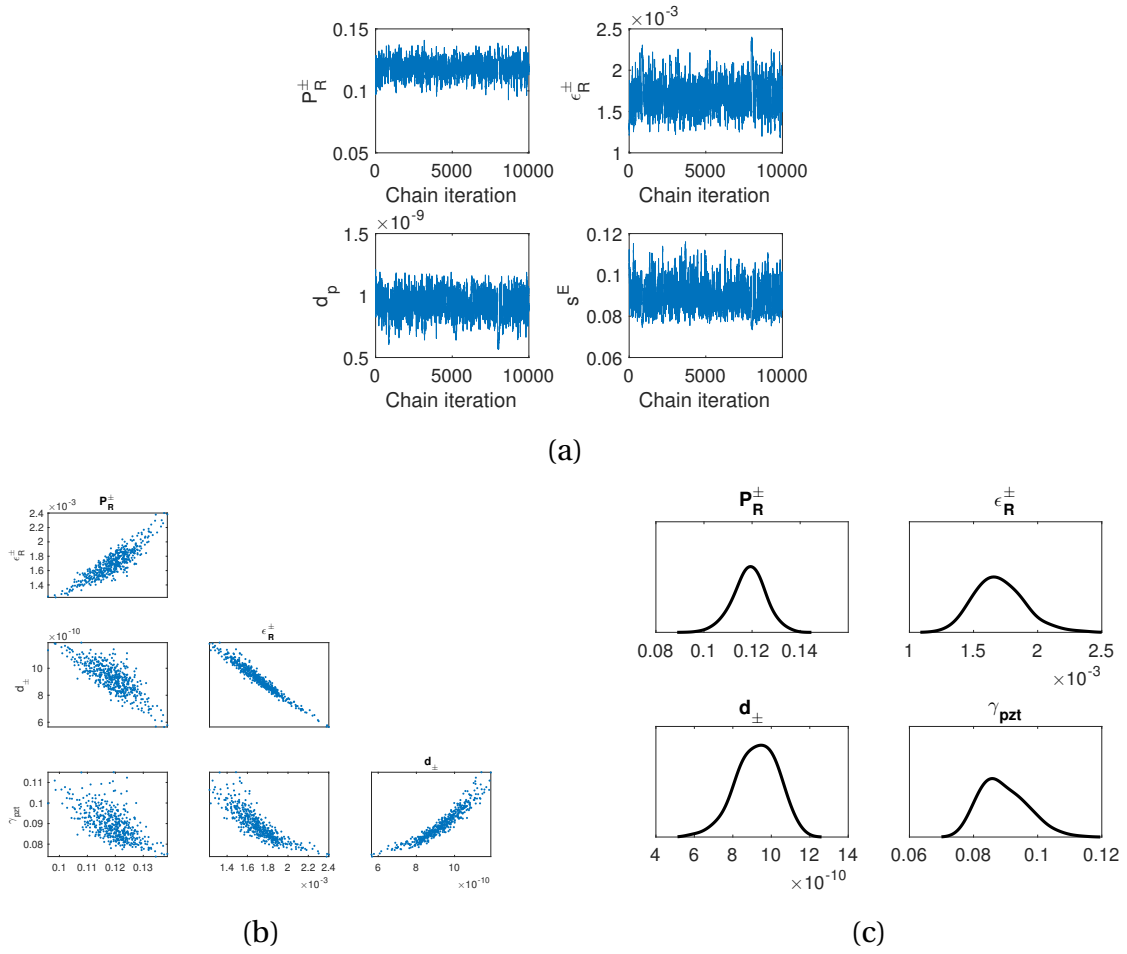


**Figure 4.1** Results from DRAM (a) chains, (b) pairwise plots, and (c) marginal densities.

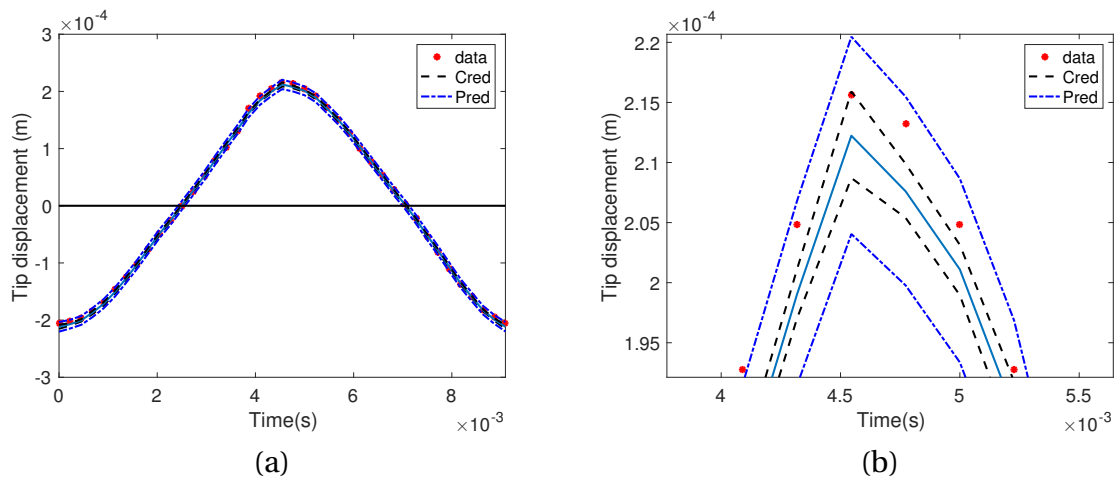


**Figure 4.2** (a) 95% credible intervals and prediction intervals and (b) magnification of (a).



## CHAPTER

## 5

# PARAMETER-DEPENDENT DYNAMIC MODE DECOMPOSITION

### 5.1 Dynamic Mode Decomposition

The Homogenized Energy Model (HEM) model is computationally intensive, which motivates the construction of a surrogate model for control design and real-time control implementation. We investigated using a dynamic mode decomposition (DMD) as a surrogate model. DMD is used when the dynamics are too complex to quantify using physics-based models or models are too computationally expensive to permit real-time solutions for design and control [19].

DMD approximates the Koopman Operator,  $\mathcal{A}$ , that describes the nonlinear dynamics of a system. The Koopman operator is an infinite dimensional linear operator that acts on the Hilbert space,  $H$ , which contains all observable functions  $g : \mathbb{R}^n \mapsto \mathbb{R}^n$  of the state vector  $x_k$ . Let  $x_k \in \mathbb{R}^n$  and  $F : \mathbb{R}^n \mapsto \mathbb{R}^n$  be a flow map such that  $x_{k+1} = F(x_k)$ . We note that the range is the same space as the domain. Here the Koopman operator,  $\mathcal{A}$ , is known as

the composition operator, such that

$$\mathcal{A}g(x_k) = g(F(x_k)) = g(x_{k+1}).$$

In other words, the operator from one observation to the next. In our case, the observations are the state vectors,  $x_k$ , that describe the displacement the beam.

An example from [19], consider the system

$$\frac{dx}{dt} = -\mu x,$$

with the initial condition  $x(0) = x_0$ . The continuous solution is  $x(t) = x_0 e^{-\mu t}$ . The solution at time  $t_{k+1}$  is

$$x(t_{k+1}) = x_{k+1} = x_0 e^{-\mu t_{k+1}}$$

We define the observation functional as  $g(x_k) = x_{k+1}$ ; i.e., the state vector. The Koopman operator is the linear operator on  $g(x_k)$  such that

$$\mathcal{A}g(x_k) = g(x_0 e^{-\mu t_{k+1}}) = x_0 e^{-\mu t_{k+1}} = x_{k+1}$$

Thus, the dynamics of a continuous nonlinear nonlinear system can be expressed by applying the Koopman operator to the observable function  $g(x_k) = x_k$ ,

$$x_{k+1} = \mathcal{A}g(x_k) = \mathcal{A}x_k.$$

Our objective is to approximate the Koopman operator by a finite dimensional matrix  $A$ .

To show the historical formulation of DMD as in [32], we combine observations with step size  $\Delta t$  in a matrix as columns,

$$X_1^{M-1} = [x_1, x_2, \dots, x_{M-1}].$$

Note that new research in [7, 19, 39] has been able to relax the assumption of periodic observations. Data can be sparse in both the time and spatial domain and sampled at non-periodic time intervals. We consider the case where  $\Delta t$  is constant. The span of the columns of

$$X_1^{M-1} = [x_1, Ax_1, \dots, A^{M-2}x_1]$$

is a Krylov subspace. We can express the final observation,  $x_M$ , as a linear combination of the Krylov basis and a residual term,  $r$ , that is orthogonal to the Krylov space:

$$x_M = \sum_{k=1}^{M-1} s_k x_k + r.$$

Note that

$$X_2^M = AX_1^{M-1}. \quad (5.1)$$

Using the expression for  $x_M$ , we obtain

$$X_2^M = X_1^{M-1} \tilde{A} + r e_{(M-1)},$$

where  $e_{(M-1)}$  is the  $(M-1)^{th}$  unit vector and  $\tilde{A}$  is the companion matrix with the  $s_i$  terms in the final column. We note that  $A$  is the finite-dimensional tangential approximation of the Koopman Operator; i.e., the eigenvectors and eigenvalues of  $A$  approximate the Koopman modes and eigenvalues. Therefore, we approximate the Koopman with a finite-dimensional matrix,  $A$ , that is a companion matrix of  $\tilde{A}$ .

We define the DMD modes or dynamic modes as the eigenvectors of

$$A = X_2^M (X_1^{M-1})^\dagger.$$

where  $\dagger$  denotes the Moore-Penrose inverse. This approximation minimizes the Frobenius norm of the error between the approximation and the output, or

$$\min_A \sqrt{\sum_{i=1}^n \sum_{j=1}^m ([X']_{ij} - [AX]_{ij})^2}.$$

To compute the dynamic modes, we use Algorithm 5 from [19]. In step 2, we utilize the data matrix having low rank by taking an SVD of  $X_1^{M-1}$  with rank  $r$ . We truncate the SVD of  $X_1^{M-1}$  by retaining the  $r$  largest singular values and the corresponding singular vectors. The columns of  $\Phi$  are the dynamic modes or the eigenvectors of  $A$  with corresponding eigenvalues

$$\Lambda = \begin{bmatrix} \lambda_1 & 0 & 0 \\ 0 & \ddots & 0 \\ 0 & 0 & \lambda_r \end{bmatrix}.$$

Once the dynamic modes are computed, we can approximate,  $x(t)$ , for all time  $t$  with the formula,

$$x(t) = \Phi e^{\Omega t} b, \quad (5.2)$$

where  $b = \Phi^\dagger x_1$ ,  $\Omega = \frac{\ln(\Lambda)}{\Delta t}$ , and

$$\ln(\Lambda) = \begin{bmatrix} \ln(\lambda_1) & 0 & 0 \\ 0 & \ddots & 0 \\ 0 & 0 & \ln(\lambda_r) \end{bmatrix}.$$

For predictions on evenly spaced intervals  $\Delta t$ , we also can use

$$x_{k+1} = \Phi \Lambda^k b.$$

This is simply the relation

$$x_{k+1} = A^k x_1 = A x_k.$$

Note, if the condition number for  $A$  is large, then the problem is ill-conditioned, which causes the approximation to not be accurate. Using (5.2) projects the Koopman approximation down to the proper orthogonal decomposition (POD) modes which improves the condition number which allows for more accurate approximations when the  $A$  is ill-conditioned.

We note that DMD and POD have many similarities. They are both reduced-order models that utilize the low-dimensionality of the data to make low-rank approximations for a complex dynamical system. The primary component for each algorithm is the SVD of the data matrix. The primary difference between DMD and POD is that DMD is equation free. DMD is a data-driven method that requires no additional work to make future predictions. However, POD requires a projecting the full-order system onto the POD modes to generate a reduced-order model. This is often accomplished by using Galerkin projection, which often generates a simpler dynamical equation that need to be solved to make future predictions. These POD-Galerkin reduced-order models can still be computationally intensive to solve [19] and can produce unstable systems [30].

1. Construct the data matrix,

$$X_1^{M-1} = [x_1, x_2, \dots, x_{M-1}],$$

and output matrix,

$$X_2^M = [x_2, x_3, \dots, x_M].$$

2. Determine the reduced SVD of  $X_1^{M-1}$ ,

$$X_1^{M-1} \approx U \Sigma V^*$$

with rank  $r$ .

3. Compute

$$\tilde{A} = U^* X_2^M V \Sigma^{-1},$$

4. Calculate the eigenvalue decomposition of  $\tilde{A}$ ,

$$\tilde{A} W = W \Lambda$$

5. Determine dynamic modes by calculating,

$$\Phi = X_2^M V \Sigma^{-1} W.$$

Note that the dynamic modes are the columns of  $\Phi$ .

**Algorithm 5:** Dynamic Mode Decomposition algorithm from [19].

### 5.1.1 Examples

We implemented the DMD algorithm on steady state data generated from the HEM from Chapter 2. For an impulse response with the HEM, the time steps need to be extremely small to quantify the high frequency information. We decided to investigate the simplest case first.

We first used the HEM code for PZT bimorph actuation to create data for the algorithm. We make observations along the beam beginning at  $x = 0$  m with step size  $h_x = 6.25 \times 10^{-4}$  m and ending at  $x = 0.01$  m. We let  $t \in [0, 3.5]$  and take the sampling rate to be  $h_t = 0.002$ . We drove the beam with the signal  $V_b(t) = 150 + 150 \sin(4\pi t)$ . Figure 5.1 shows that the DMD approximation fits the data well. In the figure, the DMD approximation was created

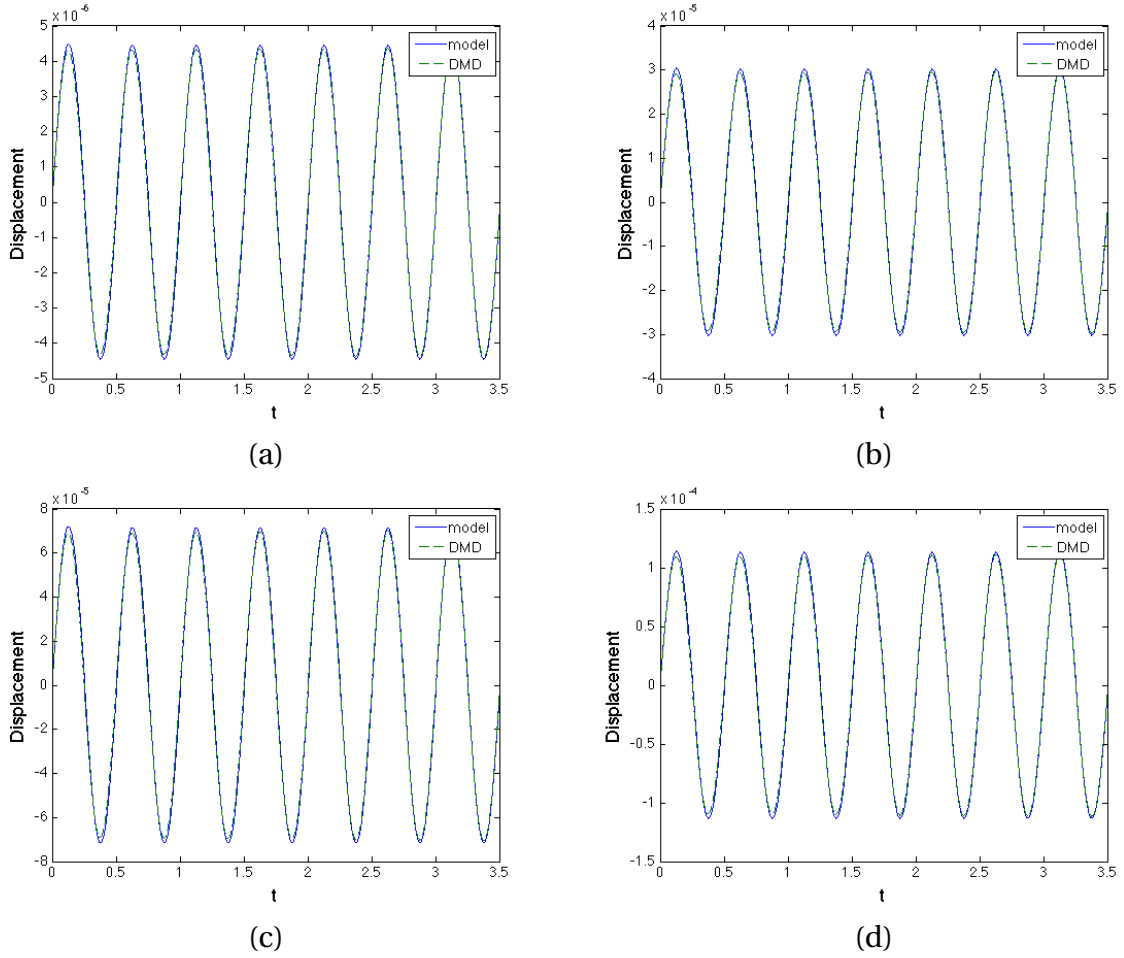


**Figure 5.1** DMD for the HEM driven by  $V_b(t) = 150 + 150 \sin(4\pi t)$  at fixed spatial points: (a)  $x = 0.0025\text{m}$ , (b)  $x = 0.005\text{m}$ , (c)  $x = 0.0075\text{m}$ , and (d)  $x = 0.01\text{m}$ .

using seven singular values and vectors from  $\Sigma$  from step (2) of Algorithm 5. Table 5.1 displays a size of the singular values of  $\Sigma$  calculated during the DMD. We tested the different truncating at different sigmas. The most accurate approximation was produced when we truncated after seven singular values. We note that the relative value for all of singular values are a magnitude larger than machine epsilon.

Figure 5.2 shows that the DMD approximations where only the first 0.875 seconds of the data was used to construct the DMD. In the figure, the DMD approximation was created using seven singular values and vectors. Table 5.2 displays first eight singular values of  $\Sigma$  calculated during the DMD. We used DMD to predict actuation for a length of 3.5 seconds,

so using the DMD to extrapolate from 0.875-3.5 seconds. The error of our approximations seems to grow the longer we extrapolate, but we are able extrapolate for over two seconds while maintain a relative error of less than 15%. We can use less than one second worth of data to model 3.5 seconds of the actuation.

We are able to approximate the HEM using DMD when we consider a steady response. However, there are limitations to DMD. When we attempt to form the DMD of an impulse response, we were not able to approximate the dynamics with the DMD as shown in Figure 5.3. Note that we consider the impulse response of a simplified beam model due to the complexity of the HEM. The beam is longer,  $\ell = 0.393$  m, height and width are uniform throughout the beam, and the substrate is a single piece of material. The patch is attached to the beam at [0.041 m, 0.092 m]. The simplified model uses a single parameter to quantify the material behavior of PZT given a voltage. The numerical implementation is from [3], which is based on the beam code from [33]. The DMD approximates the model for less than a hundredth of a second, before decaying to a steady response. The rapid decay of the high frequencies are causing the approximation to decay and not quantify the lower frequencies.

We then attempted to allow the high frequency information to decay out, then produce the DMD which still did not produce accurate approximations. We allowed two seconds to pass before sampling the data that is utilized in the DMD. Figure 5.4 displays the approximation of the DMD, which performs worse than starting the sampling when  $t = 0$ . The high frequency information still affects the approximation even though it appears that most of

**Table 5.1** Singular values for HEM Example.

	Singular Values
$\sigma_1$	0.007
$\sigma_2$	$2.807 \times 10^{-10}$
$\sigma_3$	$1.274 \times 10^{-12}$
$\sigma_4$	$3.156 \times 10^{-16}$
$\sigma_5$	$1.900 \times 10^{-16}$
$\sigma_6$	$1.700 \times 10^{-16}$
$\sigma_7$	$4.823 \times 10^{-17}$
$\sigma_8$	$5.847 \times 10^{-18}$

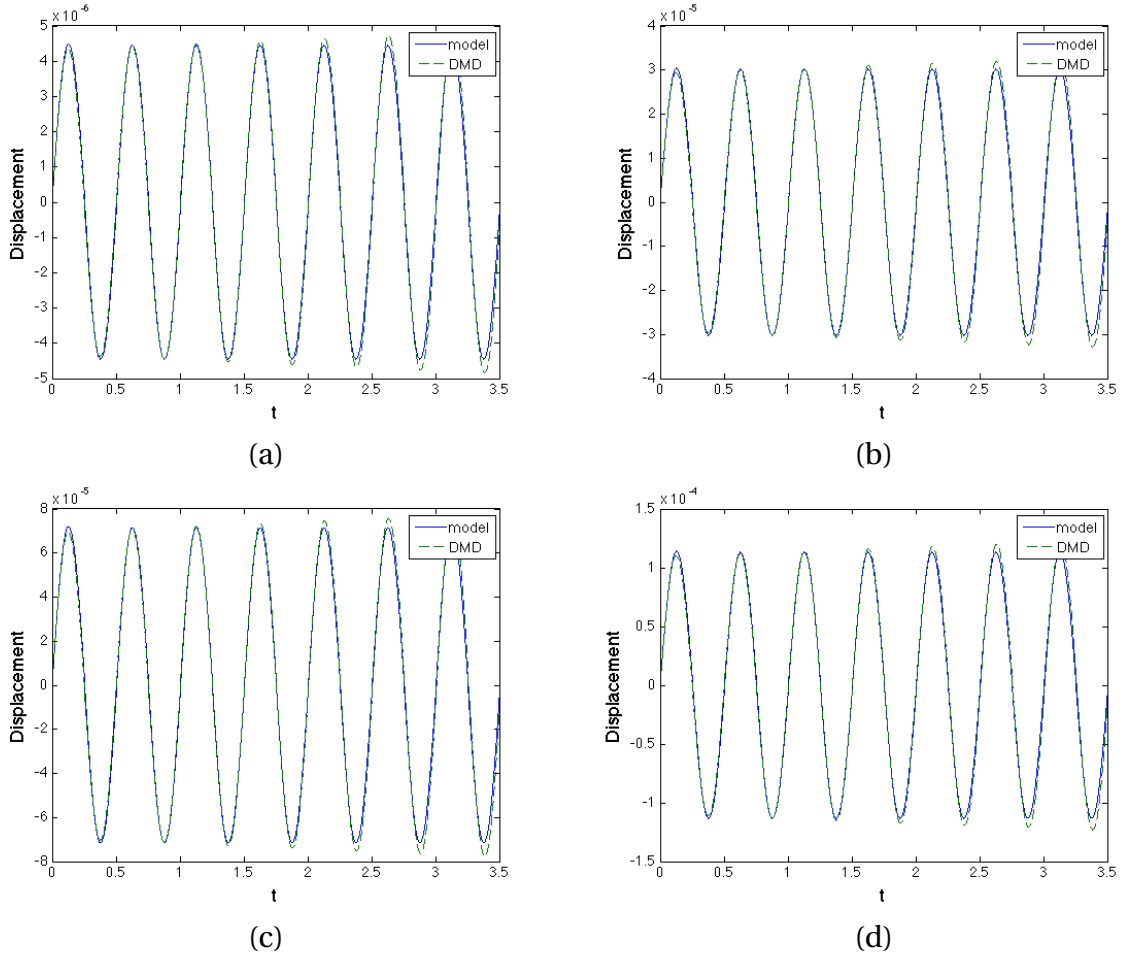


**Figure 5.2** DMD approximation for the HEM driven by  $V_b(t) = 150 + 150 \sin(4\pi t)$  using the first 0.8750 seconds of data to create the DMD, then extrapolating with the DMD at fixed spatial points: (a)  $x = 0.0025\text{m}$ , (b)  $x = 0.005\text{m}$ , (c)  $x = 0.0075\text{m}$ , and (d)  $x = 0.01\text{m}$ .

the high frequencies have decayed to zero. We attempted other methods to achieve better approximations; i.e., change the sampling frequency and sampled across more points along the beam. However, we were not able to improve the approximation, so DMD could not quantify the dynamics of the impulse behavior of a beam.

We will strictly consider a controlled response for the remainder of the chapter. Another limitation of DMD is that it does not allow for different controls to be applied to the system, so we investigate an extension of DMD called dynamic mode decomposition with control.



**Table 5.2** Singular values for HEM Example with extrapolation.

	Singular Values
$\sigma_1$	0.003
$\sigma_2$	$2.791 \times 10^{-10}$
$\sigma_3$	$6.365 \times 10^{-13}$
$\sigma_4$	$2.229 \times 10^{-16}$
$\sigma_5$	$9.543 \times 10^{-17}$
$\sigma_6$	$4.854 \times 10^{-17}$
$\sigma_7$	$1.141 \times 10^{-17}$
$\sigma_8$	$1.975 \times 10^{-18}$

## 5.2 Dynamic Mode Decomposition with Control

Dynamic mode decomposition with control (DMDC) take ideas from DMD and applies it to a control system as detailed in [28]. We can express the dynamics of a control system as

$$x_{k+1} = Ax_k + Bu_k.$$

where  $x_k \in \mathbb{R}^n$ . Here  $B$  is the control matrix and  $u_k \in \mathbb{R}^m$  is the control vector for the  $k^{th}$  observation. The goal of DMDC is to find approximations for  $A$  and  $B$ . As in Section 5.1, we construct the data matrix  $X_1^{m-1}$  and output matrix  $X_2^m$ . We additionally define the input matrix as

$$U_{\text{cont}} = [u_1, u_2, \dots, u_{m-1}].$$

As with DMD, we obtain

$$X_2^M \approx A = AX_1^{M-1} + BU_{\text{cont}} = [A \ B] \begin{bmatrix} X_1^{M-1} \\ U_{\text{cont}} \end{bmatrix},$$

This produces an augmented operator matrix,

$$\mathbf{A} = \begin{bmatrix} A & B \end{bmatrix}$$

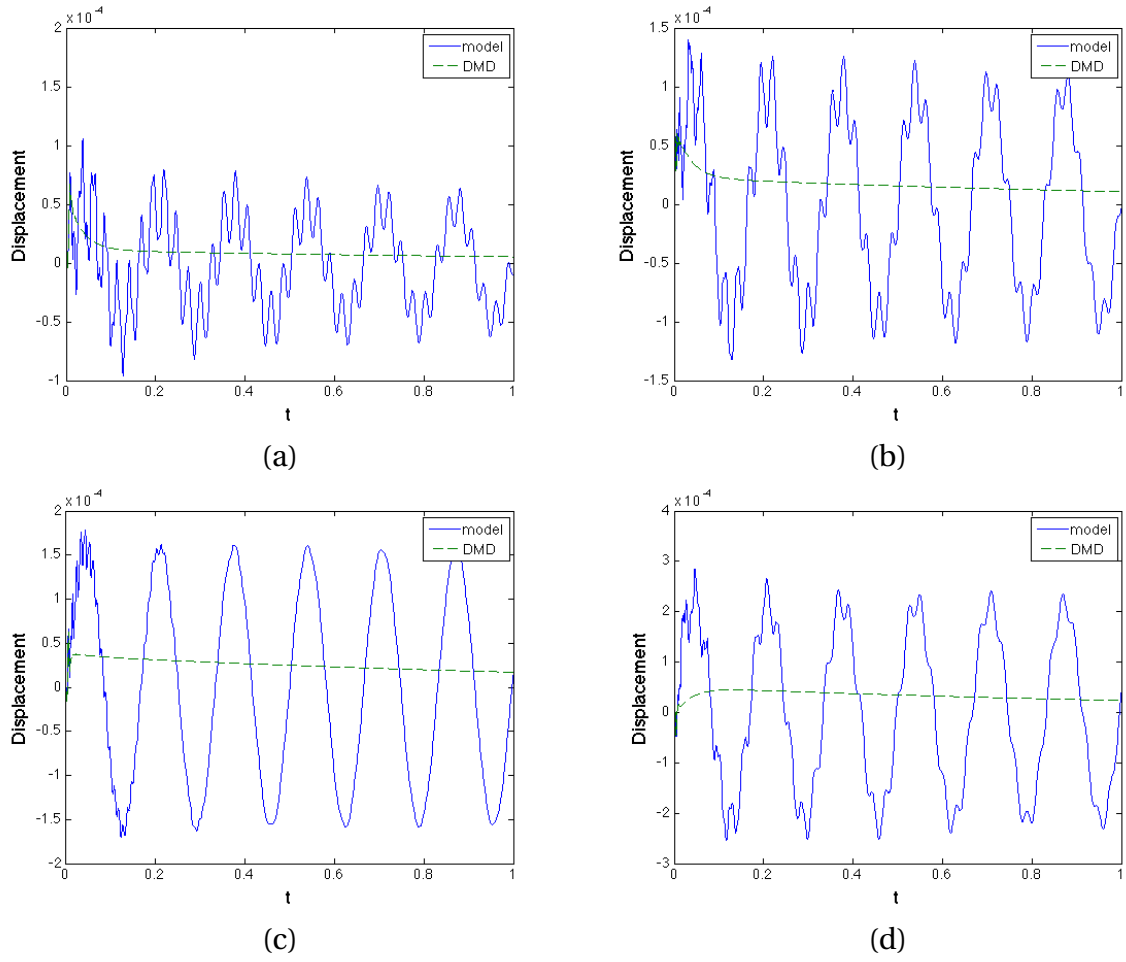


**Figure 5.3** Impulse response for a simplified beam example at fixed spatial points: (a)  $x = 0.1500\text{m}$ , (b)  $x = 0.225\text{m}$ , (c)  $x = 0.3000\text{m}$ , and (d)  $x = 0.3750\text{m}$ .

and an augmented data matrix

$$\mathbf{X} = \begin{bmatrix} \mathbf{X}_1^{M-1} \\ \mathbf{U}_{\text{cont}} \end{bmatrix}.$$

Note that the system

$$\mathbf{X}_2^M = \mathbf{A}\mathbf{X}$$

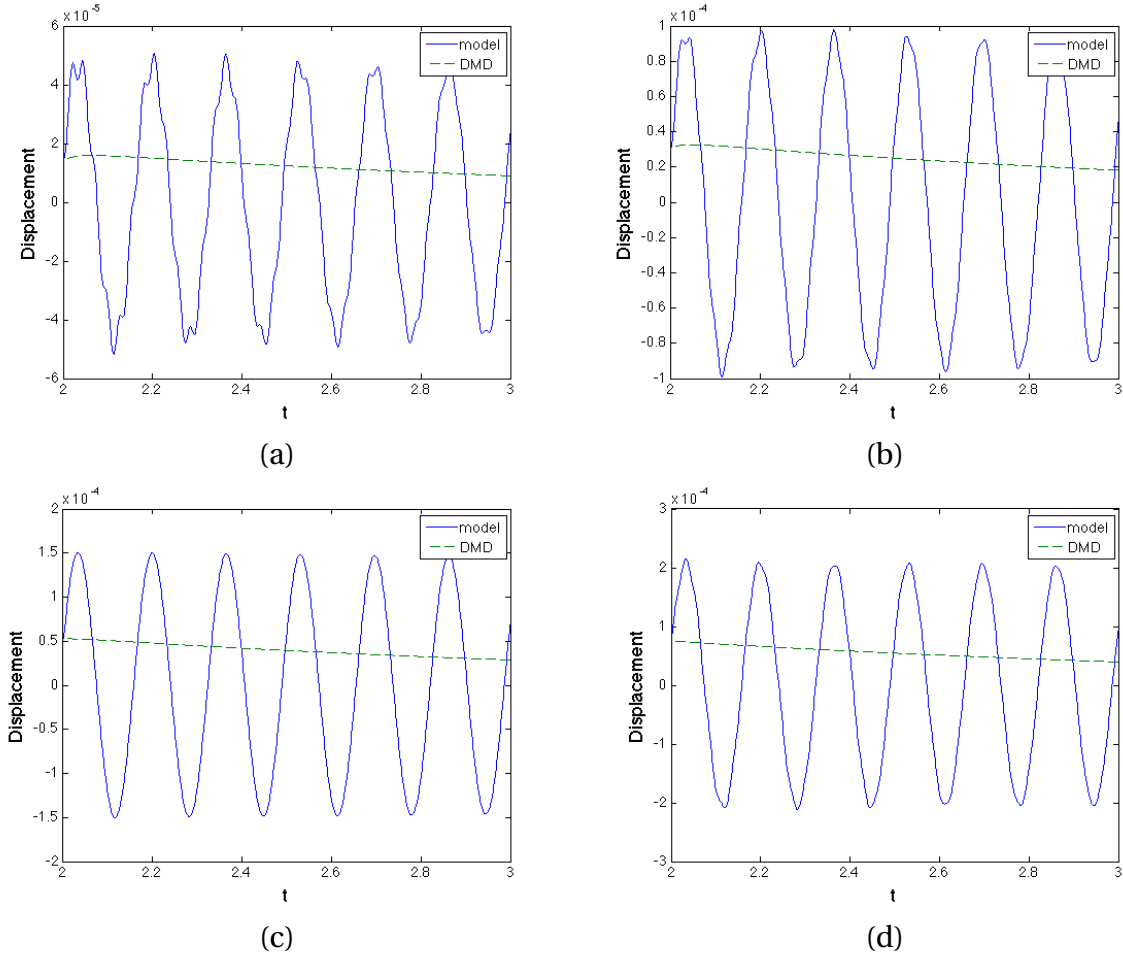


**Figure 5.4** Impulse response for a simplified beam example where sampling started at  $t_0 = 2$  secs at fixed spatial points: (a)  $x = 0.1500m$ , (b)  $x = 0.2250m$  (c)  $x = 0.3000m$ , and (d)  $x = 0.3750m$ .

is of the same form as (5.1). We define DMDc as the eigenvectors of  $A$  defined by

$$[A \ B] = X_2^M \begin{bmatrix} X_1^{M-1} \\ U_{\text{cont}} \end{bmatrix}^\dagger.$$

We calculate the DMDc using Algorithm 6 from [28]. To compute the reduce SVD of  $\begin{bmatrix} X_1^{M-1} \\ U_{\text{cont}} \end{bmatrix}$  with rank  $r$  and  $X_2^M$  with rank  $\bar{r}$ , we truncate the two SVD's by retaining the  $r$  and  $\bar{r}$ , largest singular values and their corresponding singular vectors, respectively. The columns

1. Construct the data matrix,

$$X_1^{M-1} = [x_1, x_2, \dots, x_{M-1}],$$

the output matrix,

$$X_2^M = [x_2, x_3, \dots, x_M],$$

and the input matrix,

$$U_{\text{cont}} = [u_1, u_2, \dots, u_{m-1}].$$

2. Determine the reduced SVD of the augmented data matrix,

$$\begin{bmatrix} X_1^{M-1} \\ U_{\text{cont}} \end{bmatrix} \approx U \Sigma V^*$$

with rank  $r$  and the reduced SVD of the output matrix,

$$X_2^M \approx \bar{U} \bar{\Sigma} \bar{V}^*,$$

with rank  $\bar{r}$ .

3. Compute

$$\tilde{A} = \bar{U}^* X_2^M V \Sigma^{-1} U_1^* \bar{U},$$

and

$$\tilde{B} = \bar{U}^* X_2^M V \Sigma^{-1} U_2^*,$$

where we split  $U = [U_1 \ U_2]$ , with  $U_1 \in \mathbb{R}^{n \times r}$  and  $U_2 \in \mathbb{R}^{m \times r}$ .

4. Calculate the eigenvalue decomposition of  $\tilde{A}$ ,

$$\tilde{A} W = W \Lambda$$

5. Determine dynamic modes by calculating,

$$\Phi = X_2^M V \Sigma^{-1} U_1^* \bar{U} W.$$

Note the dynamic modes are the columns of  $\Phi$ .

**Algorithm 6:** Dynamic Mode Decomposition with control algorithm from [28].

of  $\Phi$  are the dynamic modes or the eigenvectors of  $A$  with corresponding eigenvalues  $\Lambda$ . We do not create dynamic modes for  $B$ .

Differently from DMD, we do not approximate using the dynamic modes. We predict future states by using the reduced order system,

$$\tilde{x}_{k+1} = \tilde{A}\tilde{x}_k + \tilde{B}u_k. \quad (5.3)$$

where  $x_k = \overline{U}\tilde{x}_k$ . If we want to use the full-order system's state and control matrices in control design, we also can truncate Algorithm 6 after step 2 to approximate the state matrix  $A$  and control matrix  $B$  as

$$A = X_2^M V \Sigma^{-1} U_1^*,$$

and

$$B = X_2^M V \Sigma^{-1} U_2^*, \quad (5.4)$$

where we separate  $U = [U_1 \ U_2]$ . After we compute  $A$  and  $B$ , we can use the system

$$x_{k+1} = Ax_k + Bu_k$$

to predict the behavior of the nonlinear system. Note that depending on the size of the state vector, it will be computationally more tractable to use the reduced order system. For the HEM problem,  $n = 16$ , so we are able to use either method.

We use the HEM to generate data for the dynamic mode decomposition with control (DMDc) algorithm. Figure 5.5 displays the HEM data at the tip of the beam used to create the approximate the system's  $A$  and  $B$  matrices as well as the DMD approximation. We observed that DMDc accurately approximates the data. The data was sampled at a rate of 500 evenly spaced samples a second. The control input matrix is constructed from the voltages that are applied to both patches. When we attempt to only use one voltage, the algorithm failed to produce an accurate surrogate. The DMDc approximation using one voltage as the control does not quantify the effects of both PZT patches on the system. Thus, even though the voltages are related, using both voltages in the input matrix is necessary. We truncated the data and control matrix at  $r = 3$  singular values, because there is a drop-off on the order of  $10^{-6}$  in the magnitude of the singular values. Note, we need to have at least two singular values for the control and at least one for the system, so it is possible to split  $U = [U_1, U_2]$ .

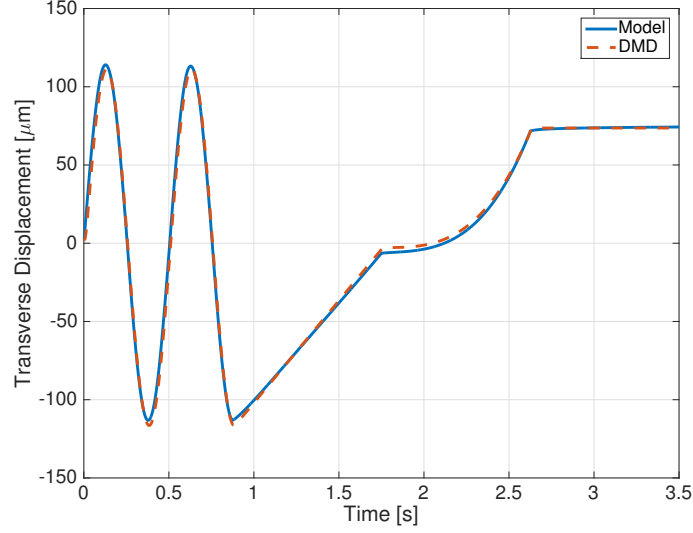


**Figure 5.5** Data that was used to create the approximate the full-order system's state matrix  $A$  and control matrix  $B$  that is utilized in future control design and the DMDc approximation.

### 5.3 PI Control

With the approximation of state  $A$  and control  $B$  matrix, we then implemented a PI Controller for the DMD model using the voltage  $v_b(t)$  from Section 2.2. Using the Ziegler-Nichols PI gains tuning technique outlined in [1], we implemented the controller

$$u_k = -(1 \times 10^5)e_k - (1 \times 10^8) \int_0^t e_k(s)ds + \frac{V_{\max}}{2}.$$

Here  $e_k = x_k^{\text{obs}} - r_k$  where  $r_k$  is the target function at time  $t_k$  and  $x_k^{\text{obs}}$  is the displacement at the tip of the beam at time  $t_k$ . Note that  $\frac{V_{\max}}{2}$  is added to ensure that the bimorph starts in its static neutral position. We used Ziegler-Nichols method to achieve initial values and then adjusted the gains to meet desired performance. The gains seem large, but it is primarily adjusted for the difference in the order of magnitudes for the tip displacement and the voltage. We employ a PI control instead of a PID because a fast response is not required for this system. Figure 5.6 displays the tracking capabilities of the PI controller for the surrogate

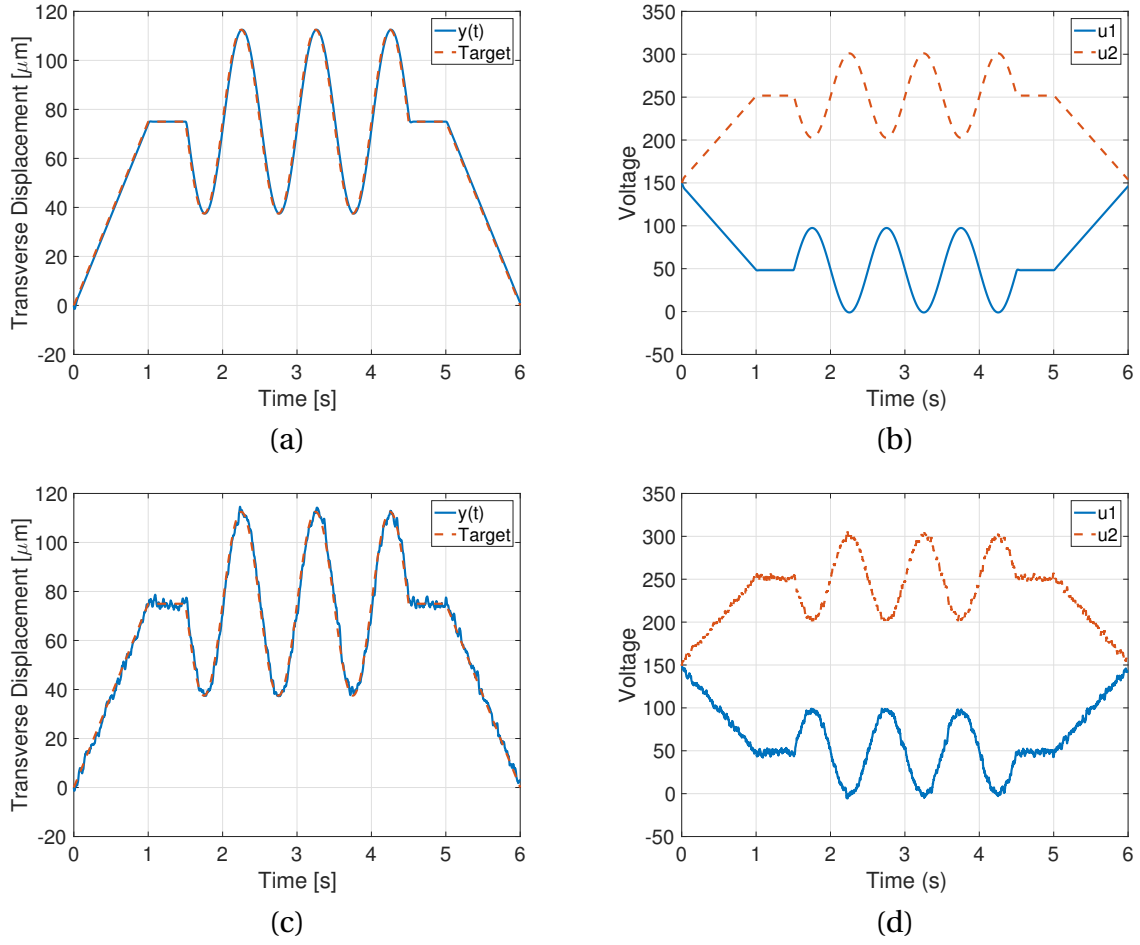


**Figure 5.6** (a),(b) The performance of the designed PI controller and the control designed, and (c),(d) includes 5% noise.

model. We added 5% noise to the state vector that is being used as feedback in the control,

$$x_k^{\text{obs}} = x_k + (0.05 \times 10^{-4})\epsilon_k,$$

where  $(0.05 \times 10^{-4})$  is 5% of the maximum order of magnitude of the tip displacement. Here  $\epsilon_k \sim N(0, 1)$ . We observe that the system is able to track the trajectory despite the added noise.

We next tested how the control would work on the HEM. We applied the control as a feedforward control to the HEM as outlined in Algorithm 7. Figure 5.7 displays the results

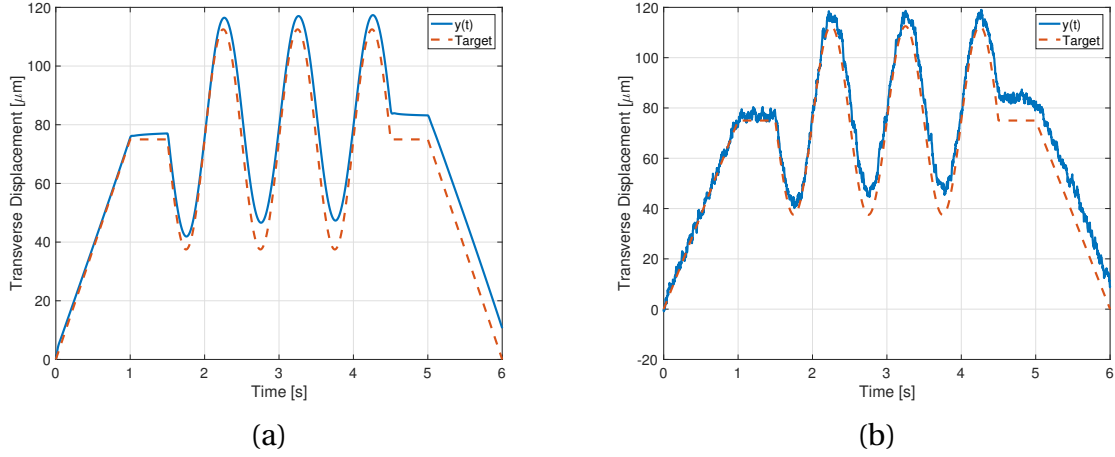


**Figure 5.7** (a) The control from DMDc as a feedforward control in HEM and (b) with 5% noise.

for the feedforward problem. The feedforward problem produces a stable solution, but tracks the target function less accurately than the feedback problem on the DMDc system, which we expected. We observed the feedforward control tracks accurately initially until the oscillations of the target function. The surrogate does not track the target function to the desired accuracy. We will investigate implementing the PI control as a feedback control.

Last, we employed the PI control designed with the surrogate model as a closed-loop controller to the HEM. Figure 5.8 displays the results of the PI controller on the high-fidelity model with 5% noise added to the system. The PI controller adequately tracks a discontinuous target function.

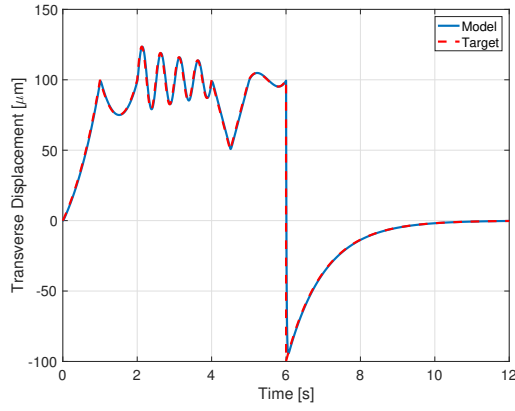
1. Compute  $A$  and  $B$  from DMDc to approximate the system,

$$x_{k+1} = Ax_k + Bu_k$$

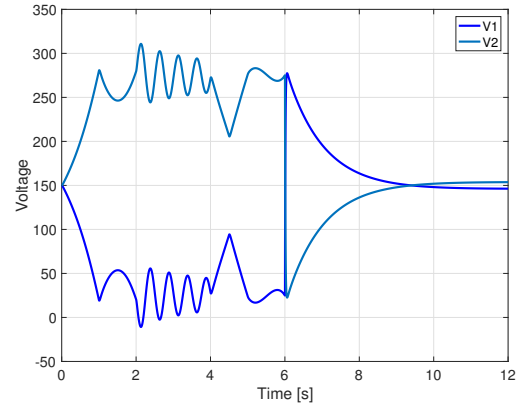
2. Design a PI Control for the DMDc system
3. Use the PI control on the DMDc system and collect  $u_k$ .
4. Run the HEM with the control  $u_k$  as the voltage,  $V_b(t)$ .

**Algorithm 7:** Feedforward Algorithm.

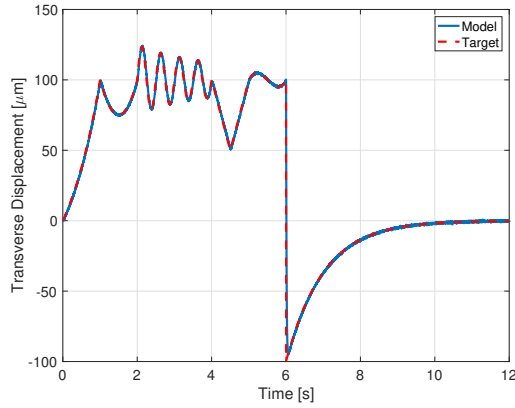




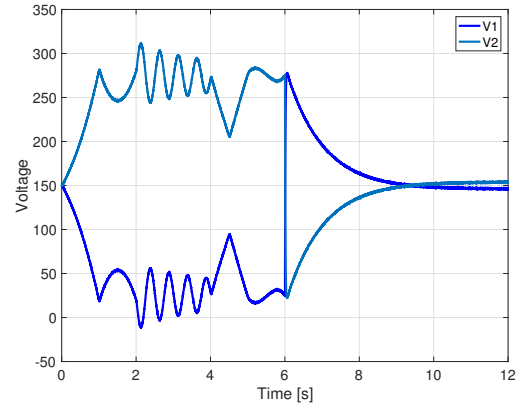
(a)



(b)



(c)



(d)

**Figure 5.8** (a),(b)The control from DMDC as PI control in the high-fidelity model and (c),(d) with 5% noise.

## 5.4 Interpolation method

The goal here is to expand DMDC to be parameter-dependent. This allows us to perform optimization and uncertainty quantification on the surrogate model in lieu of the full-order model. We can also use DMDC to design a robust control for the full order problem. The method we employ is an interpolation method discussed in [13]. The method was developed for projection-based surrogate models like proper orthogonal decomposition (POD).

We consider the problem

$$x_{k+1} = A(q)x_k + B(q)u_k,$$

where  $x \in \mathbb{R}^n$ ,  $B(q) \in \mathbb{R}^{n \times \ell}$ , and  $A(q) \in \mathbb{R}^{n \times n}$ . Here  $n$  is the number of states and  $\ell$  is the number of control inputs. Let

$$\mathbb{A} = \{A^1, A^2, A^3 \dots A^N\},$$

where  $A^k = A(q^k)$  and  $q^k \in \mathbb{R}^p$ . Here  $\mathbb{A}$  will be interpolated elementwise to calculate  $\tilde{A}$  corresponding with the parameter  $\tilde{q}$ . We accomplish this by using cubic splines. For a single parameter, we order the  $q^j$  in monotonically increasing order. If  $q^k \leq \tilde{q} \leq q^{k+1}$ , then the cubic spline interpolant for the  $\tilde{A}_{ij}$  is

$$\tilde{A}_{ij} \approx f^{k_{ij}}(\tilde{q}) = \sum_{l=0}^3 \alpha_l^{k_{ij}} \left( \frac{\tilde{q} - q^k}{q^{k+1} - q^k} \right)^l$$

The coefficients  $\alpha_h^{k_{ij}}$  are determined by the conditions

$$\begin{aligned} f^{k_{ij}}(q^k) &= A_{ij}^k, \\ f^{(k-1)_{ij}}(q^k) &= A_{ij}^k, \\ \frac{df^{(k-1)_{ij}}}{d\tilde{q}}(q^k) &= \frac{df^{k_{ij}}}{d\tilde{q}}(q^k), \\ \frac{d^2 f^{(k-1)_{ij}}}{d\tilde{q}^2}(q^k) &= \frac{d^2 f^{k_{ij}}}{d\tilde{q}^2}(q^k). \end{aligned}$$

Initially, we considered a third-level Clenshaw-Curtis grid to prevent Runge's phenomenon. The Clenshaw-Curtis nodes are defined by

$$q_3^r = \frac{1}{2} \left( 1 - \cos \left( \frac{\pi(r-1)}{2^{3-1}} \right) \right),$$

where  $r = 1, \dots, 2^{3-1} + 1$  as illustrated in Figure 5.9 for a two dimensional case. To interpolate, we used MATLAB's *interp* function with the cubic spline. The number of nodes increase

exponentially with the number of parameters for a tensored grid,

$$\text{number of nodes} = (2^{3-1} + 1)^p,$$

so we also considered two sparse grids.

The first sparse grid we consider is Smolyak's sparse grid, proposed in [36]. The nodes for the Smolyak's sparse grid are

$$\Theta_l^p = \bigcup_{|\ell'| \leq l+p-1} \Theta_{\ell_1}^1 \times \cdots \times \Theta_{\ell_p}^1,$$

where  $l$  is the level,  $p$  is the number of parameters, and  $|\ell'| = \sum_{k=1}^p \ell_k$ . Here  $\Theta_{\ell_1}^1$  is the set of nodes for one parameter at the  $\ell_1$  level from the Lobatto grid. A two dimensional example is shown in Figure 5.10. The nodes for  $k^{th}$  level Lobatto grid are given by  $x = \pm 1$  and the roots of  $\frac{dP_{k-1}}{dx}$  where  $P_k$  is the  $k^{th}$  Legendre polynomial. As the second method of sparse grids, we implemented a 200-point latin hyper cube design, from [24], as displayed in Figure 5.10. Once we have the nodes for the grid, we rotated the nodes using the covariance matrix from uncertainty quantification results, so the grid aligns with the correlation structure of the parameters. To interpolate the two different sparse grids, we used MATLAB's *griddatan* function. This is a linear spline interpolator that accommodates scattered or sparse data.

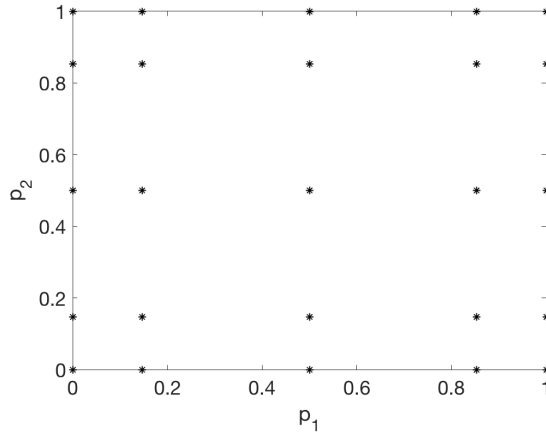


**Figure 5.9** Two dimensional level-3 Clenshaw-Curtis grid.

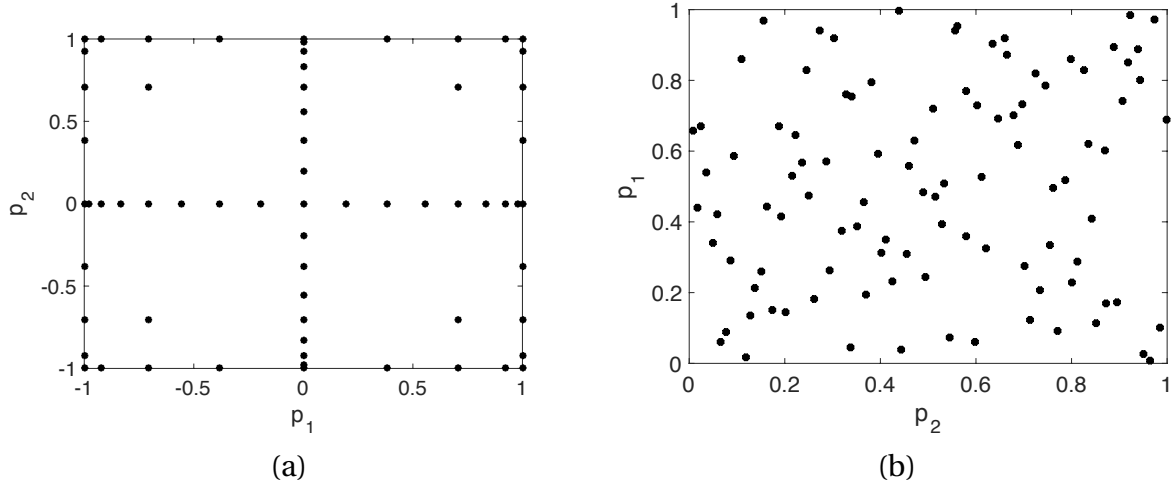


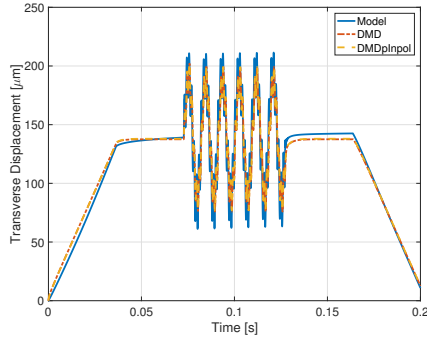
**Figure 5.10** (a) Level-5 Lobatto grid based Smolyak's sparse grid and (b) Latin hypercube .

## 5.5 Results

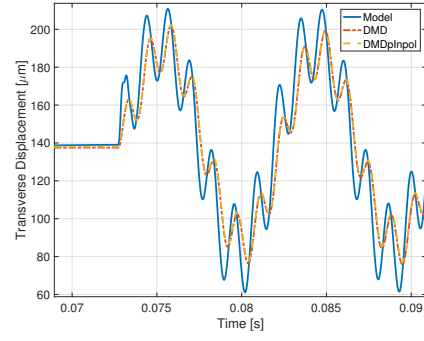
We initially consider the four identifiable parameters,  $d_{\pm}$ ,  $\gamma_{pzt}$ ,  $P_R^{\pm}$ , and  $\epsilon_R^{\pm}$ , from Section 3.2.3, which were used for performing uncertainty quantification in Section 4.3. The control was taken to be a ramp up-oscillation-ramp down control. We created oscillations from two sinusoid frequencies, 110 Hz and 770 Hz, added together. Testing was done by randomly sampling parameters from their posterior distribution.

In Figure 5.11, we compare the high-fidelity model, the DMD model, and the new DMD with parameter interpolation (DMDip). For the first two sets of parameters, the DMDip is comparable to the DMD and the approximations are within 25% of the actual model. The primary source of error is due to the delayed reaction to the voltage of the surrogate model. Note that making the oscillation region have only one frequency brings the output of the model, DMD, and DMDip to within 1% of each other. For the last set of parameters, we note that in Figure 5.11(e)-(f) that the DMD approximations are more accurate in the oscillation region, but the DMD and DMDip are clearly different. This may be due to the number of nodes in the grid. A finer Clenshaw-Curtis grid may solve this problem.

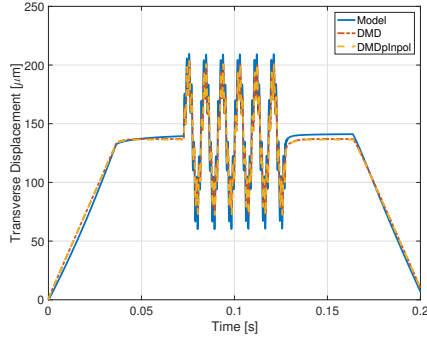
Table 5.3 displays the timing results to compute the full model, DMD, and DMDip and the number of nodes for each DMDip grid. We observe that we obtain a significant speedup using the DMD and DMDip-Clenshaw over the full order model. The two sparse



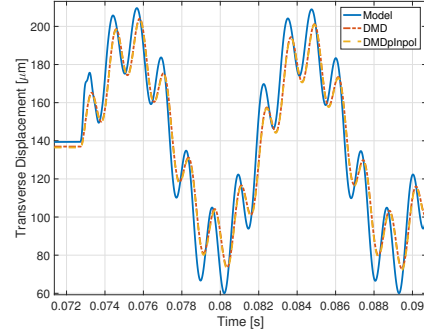
(a)



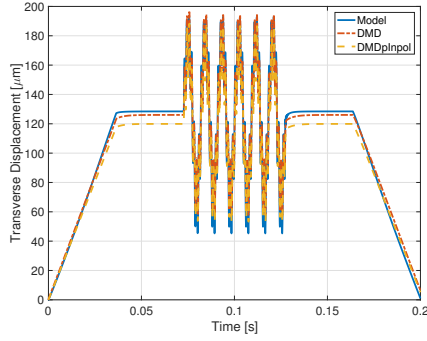
(b)



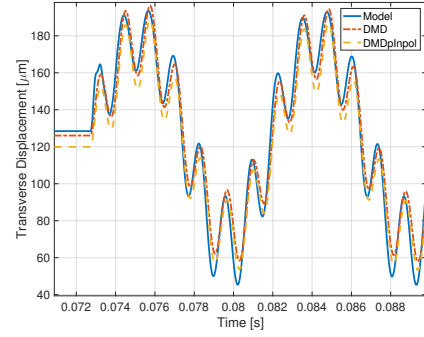
(c)



(d)



(e)



(f)

**Figure 5.11** DMD with parameter interpolation results using 5 point Clenshaw-Curtis grid where each row are results from a different set of randomly drawn parameter values for  $d_{\pm}$ ,  $\gamma_{pzt}$ ,  $P_R^{\pm}$ , and  $\epsilon_R^{\pm}$ .

grid methods are between 2-3 times faster than the full order mode. We do not see further speed up with sparse grid because, the *griddatan* function uses Delaunay triangulation

algorithm to interpolate, which is an expensive algorithm. Note that the DMD time is the time needed to perform DMD given that the data was already collected or generated.

Figure 5.12 displays the relative error,

$$\text{error} = \frac{\|y_{HEM} - y_{DMDip}\|_{\infty}}{\|y_{HEM}\|_{\infty}}$$

for 100 randomly sampled set of parameters for each of the three grid types. Note that the parameter sets were generated from the posterior distributions from the uncertainty quantification results in Figure 4.1. The control was taken to be a ramp up-oscillation-ramp down control. We created oscillations from two sinusoid frequencies, 110 Hz and 770 Hz, added together. The errors are plotted against the value of the parameters used to generate the responses. We observe that errors are correlated to parameter values. This is due to the response dependence on the parameters values. Even though, the error is relative to the magnitude of the response, the magnitude of the response affects the magnitude of the relative error. The approximations are all within 20% of the model, so they are acceptable for our application of control design. However, the DMDip is only going to perform as well as the DMDc, so we also need compared the approximations of DMDc and DMDip.

We plotted the error between the DMDc and DMDip response for each set of parameters in Figure 5.13. The errors are all less than 3% of the DMD. Our DMDip method produces an approximation of the DMD response. We note that the sparse grid methods do not exhibit correlation between the error and the parameter, so the value of the parameter does not affect the accuracy of DMDip. We decided to use the Smolyak's sparse Lobatto grid for the reminder of this analysis, because the results had the least number of errors over 1%. Note

**Table 5.3** Time to complete one model run, DMD run with the data already obtained, and DMDip run. Also, the number of nodes used for each interpolation method for DMDip.

Method	Time (s)	# of Nodes
Model	65.4	N/A
DMD	0.2	N/A
DMDip-Clenshaw	1.1	625
DMDip-Lobatto Sparse	24.5	401
Latin Hypercube	18.6	200

that the number of nodes from Table 5.3 are all on the same order of magnitude. However, the sparse Lobatto grid is more accurate then the Clenshaw-Curtis grid, because it is a larger level grid. The latin hyper cube has similar results. We could vary the number of nodes in the latin hyper cube design to achieve a more accurate interpolator, but the results we obtained are sufficiently accurate.

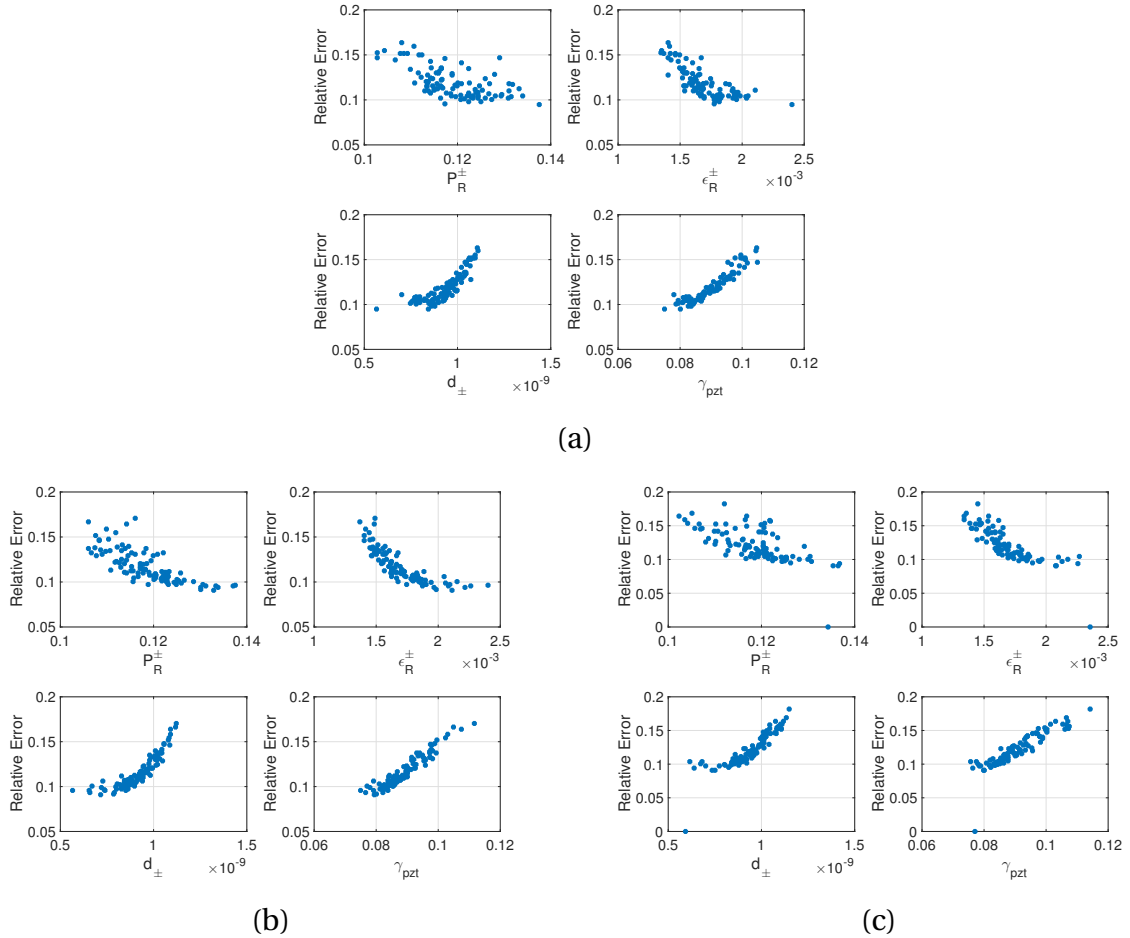
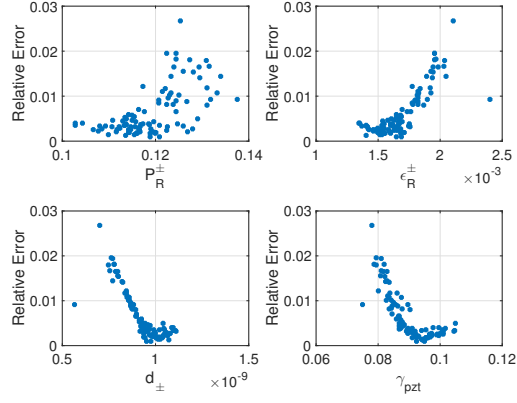
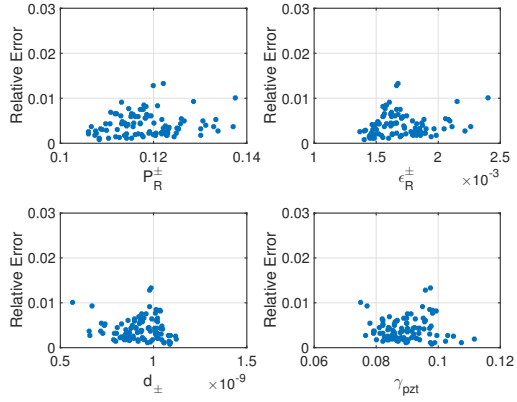


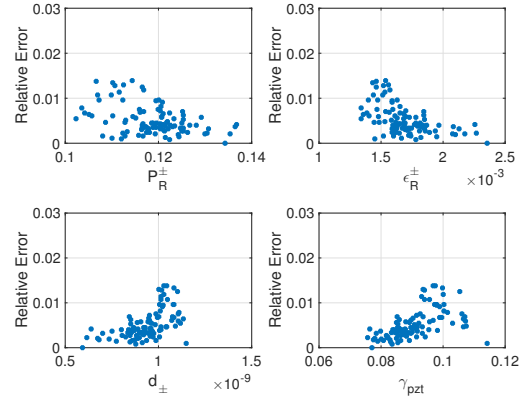
**Figure 5.12** The relative error between the model andDMDip responses plotted against the parameters for (a) full Clenshaw grid, (b) Smolyak's sparse Lobatto grid , and (c) Latin hypercube.



(a)



(b)



(c)

**Figure 5.13** The relative difference between the DMD and DMDip responses plotted against the parameters for (a) full clenshaw grid, (b) Smolyak's sparse Lobatto grid , and (c) Latin hypercube.



## CHAPTER

# 6

## SYNTHESIS OF UQ AND CONTROL

### 6.1 Discrete-Time Tracking Problem

With a parameter and control-dependent surrogate model, we can now use the surrogate model to develop control algorithms for the full-order model. Our objective is to design a robust control algorithm, so the tip of the beam tracks a target function. One common method is to examine the optimal control for the tracking problem. To do this we will consider the linear quadratic tracking problem for a discrete-time problem as discussed in [22]. Note that the surrogate model

$$x_{k+1} = Ax_k + Bu_k$$

is a linear discrete-time surrogate of a continuous system. We will consider a finite horizon tracking problem. We define the cost function to be

$$J_0 = \frac{1}{2}(Cx_N - r_N)^T P(Cx_N - r_N) + \frac{1}{2} \sum_{k=1}^{N-1} (Cx_k - r_k)^T Q(Cx_k - r_k) + u_k^T R u_k,$$

with times  $t \in [t_0, \dots, t_N]$ ,  $P$ ,  $Q$ , are semi-positive definite matrices and  $R$  is a positive definite matrix. Here  $P$  is the penalty for missing the target at the final time,  $Q$  is the penalty for not tracking the target before the final time, and  $R$  is the penalty for applying large voltages. The matrix  $R$  insures that the system is efficient with its energy consumption. Note that the step size from  $t_k$  to  $t_{k+1}$  must be equal for all  $k \in [0, N]$ , so DMDc can function properly. Finally,  $C = [0, \dots, 1]$  is the matrix that produces the tip displacement of the beam when multiplied with the state. To solve the optimal control problem, we utilize Legendre multipliers to obtain the solution

$$\begin{aligned}x_{k+1} &= Ax_k + Bu_k, \\ \lambda_k &= A^T \lambda_{k+1} + C^T Q C x_k - C^T Q r_k, \\ u_k &= -R^{-1} B^T \lambda_{k+1},\end{aligned}$$

where  $\lambda_k$  is the costate with the final-time condition

$$\lambda_N = C^T P (C x_N - r_N),$$

with initial condition  $x_0$  as in [22].

Observe that the control is in terms of the costate and that state and costate are dependent on each other with boundary conditions at initial and final times. Thus, we must express  $\lambda_k$  in terms of the state  $x_k$ . Let

$$\lambda_k = S_k x_k - v_k,$$

where  $\{S_k\}_{k=1}^N$  and  $\{v_k\}_{k=1}^N$  are sequences of auxiliary matrices and vectors, respectively. Note that  $S_k \in \mathbb{R}^{n \times n}$  and  $v_k \in \mathbb{R}^n$ . Substituting  $\lambda_k = S_k x_k - v_k$  and simplifying, we obtain the

solution of the form

$$\begin{aligned}
x_{k+1} &= Ax_k + Bu_k, \\
F_k &= (B^T S_{k+1} B + R)^{-1} B^T S_{k+1} A, \\
S_k &= A^T S_{k+1} A - A^T S_{k+1} B F_k + C^T Q C, \\
v_k &= (A - B F_k) v_{k+1} + C^T Q r_k, \\
F_k^\nu &= (B^T S_{k+1} B + R)^{-1} B^T, \\
u_k &= -F_k x_k + F_k^\nu v_{k+1},
\end{aligned}$$

with boundary conditions

$$\begin{aligned}
S_N &= C^T P C, \\
v_N &= C^T P r_N.
\end{aligned}$$

Note that  $F_k$  and  $F_k^\nu$  are the feedback gain and feedforward gain matrices. We observe that  $F_k$ ,  $S_k$ ,  $v_k$ , and  $F_k^\nu$  are all independent of the state. If we know the tracking function  $r_k$ , we can precompute all of these terms. However, this can cause memory problems, because it is necessary to store long sequences of matrices and vectors. To address the memory issue, we will consider a suboptimal tracking algorithm by using the infinite-time horizon solution for  $S_k$ .

When we substitute  $F_k$  into the equation for  $S_k$ , we observe that

$$S_k = A^T S_{k+1} A - A^T S_{k+1} B (B^T S_{k+1} B + R)^{-1} B^T S_{k+1} A + C^T Q C,$$

is the Riccati equation. We can use the solution to the algebraic Riccati equation

$$S = A^T S A - A^T S B (B^T S B + R)^{-1} B^T S A + C^T Q C,$$

to find suboptimal gain matrices. After obtaining the solution to the algebraic Riccati

equation,  $S_\infty$ , we obtain the gains

$$F_\infty = (B^T S_\infty B + R)^{-1} B^T S_\infty A,$$

$$F_\infty^v = (B^T S_\infty B + R)^{-1} B^T.$$

Then, we can precompute the sequence of vectors

$$v_k = (A - B F_\infty) v_{k+1} + C^T Q r_k,$$

where  $v_N = C^T P r_N$ . Finally, we can compute

$$x_{k+1} = A x_k + B u_k,$$

where

$$u_k = -F_\infty x_k + F_\infty^v v_{k+1},$$

With this implementation, we need to store three matrices and a sequence of vectors. If we want to reduce the number of stored vectors, we can precompute  $v_0$  and use

$$v_{k+1} = (A - B K_\infty)^{-T} v_k - (A - B K_\infty)^{-T} C^T Q r_k$$

to calculate the sequence  $\{v_k\}$  as we compute the state.

Figure 6.1 shows the solution to the optimal control problem where

$$B = B_{DMDc} \times \begin{bmatrix} -1 \\ 1 \end{bmatrix}, \quad R = 1 \times 10^{-4}, \quad P = 5 \times 10^9, \quad Q = 5 \times 10^9.$$

Here  $B_{DMDc}$  is (5.4); i.e., the matrix we get from DMDc with Section 5.2 or the interpolated  $B$  matrix from DMDip from Section 5.4. We adjust the control matrix  $B$ , so that the solution of the optimal control will be  $V_b(t)$  from Section 2.2. The control values are physically reasonable, because they are below  $V_{max} = 300$  V. We adjusted  $R$ ,  $P$ , and  $Q$  until we tracked the target to desired accuracy while maintaining a physically reasonable applied voltage. The tip displacement tracks the target function with less than 1% error. Once the optimal control was determined for the surrogate model, the optimal control was applied as a feedforward control, as in Algorithm 7 from Section 5.3, in the full-order HEM model. Figure 6.2 displays the solution to the optimal control in the full order model. The tracking

for the full-order model is not as accurate, but it is still less than a 20% error. Therefore, this is a viable solution to track the target function for many applications. We are able to use an optimal control designed with DMD to control the HEM. We will be able to run computational control experiments with the reduced-order problem to approximate and design controls for the PZT bimorph system.

### 6.1.1 Uncertainty in the Optimal Control

With a viable optimal control, we use the results from Section 4.3 to quantify the uncertainty in the solution. We sample from the posterior distributions for the four parameters and solve the optimal control problem from Section 6.1 with the reduced-order system. We took 1,500 samples to create the posterior distributions for the control and full order model displacement of the control. We present these results in Figure 6.3. We plotted 95% credible intervals; i.e., the mean response is region with a 95% probability. There is little uncertainty in either the control or displacement. The 95% credible interval has a range of less than  $10\mu\text{m}$  for the tip displacement and less than 10 volts for the voltage. The optimal control is robust with respect to the parameter uncertainty.

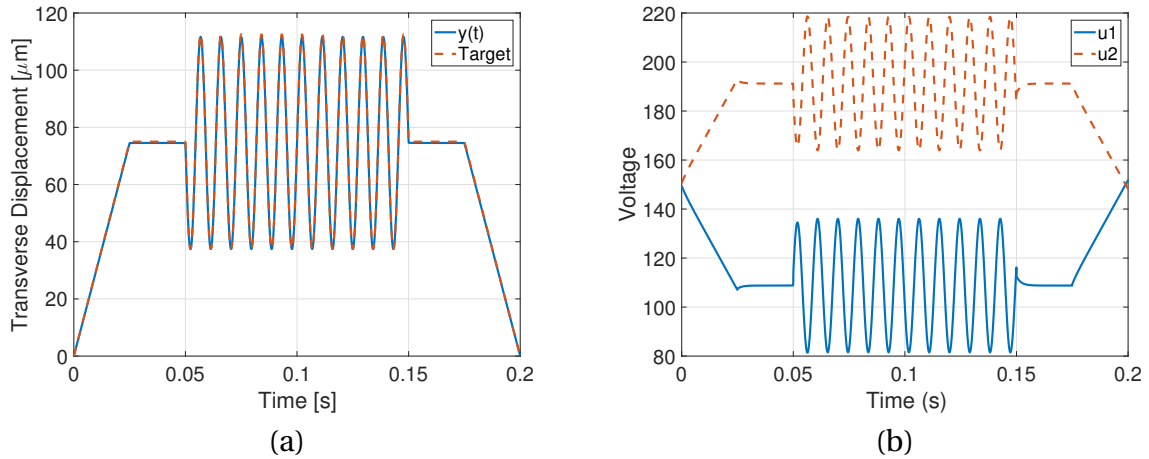


**Figure 6.1** The DMDip (a)optimal trajectory and (b)optimal control with a randomly sampled set of parameters .

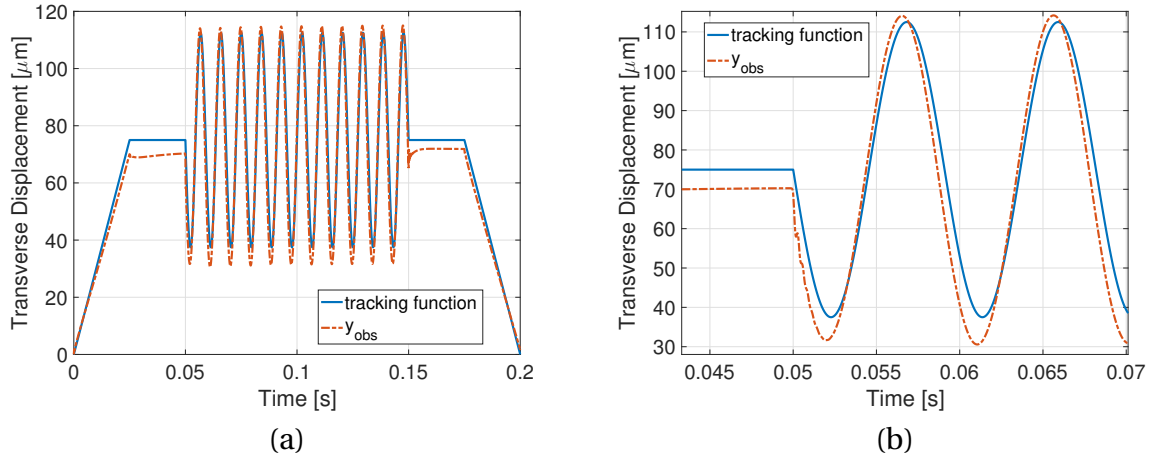


**Figure 6.2** The HEM solution using the optimal control in Figure 6.1 where (a) trajectory and (b) magnification of (a)

## 6.2 Combining the Optimal and PI control

When designing a control for the beam, we need to design the control using one set of parameter values, while keeping it robust enough to accommodate the uncertainty in the parameter. To illustrate, we employ the optimal control for the mean values of the results from Section 4.3 with the PI control from Section 5.3. The optimal control would be implemented as a feedforward control for the system. The feedback control is necessary to insure accurate tracking of the target function. Figure 6.4 displays the results of the combination of the feedback and feedforward controller. We observe that the function tracks the target function while the control is within the normal voltage usage with less than 1% error.

Next, we tested how robust the new controller is by quantifying the uncertainty in the control and output. We use the results from Section 4.3 to quantify the uncertainty in the solution. We sample from posterior distributions for the four parameters to propagate the uncertainty into the combined control problem. We took 1,000 samples to create the posterior distributions for the control and full-order model displacement. Figure 6.5 displays those results. There is little uncertainty in either the control or the displacement. The displacement uncertainty is less than 1%, while the voltage is within a range of five volts. In the combined control design, the control tracks the target function even under parameter

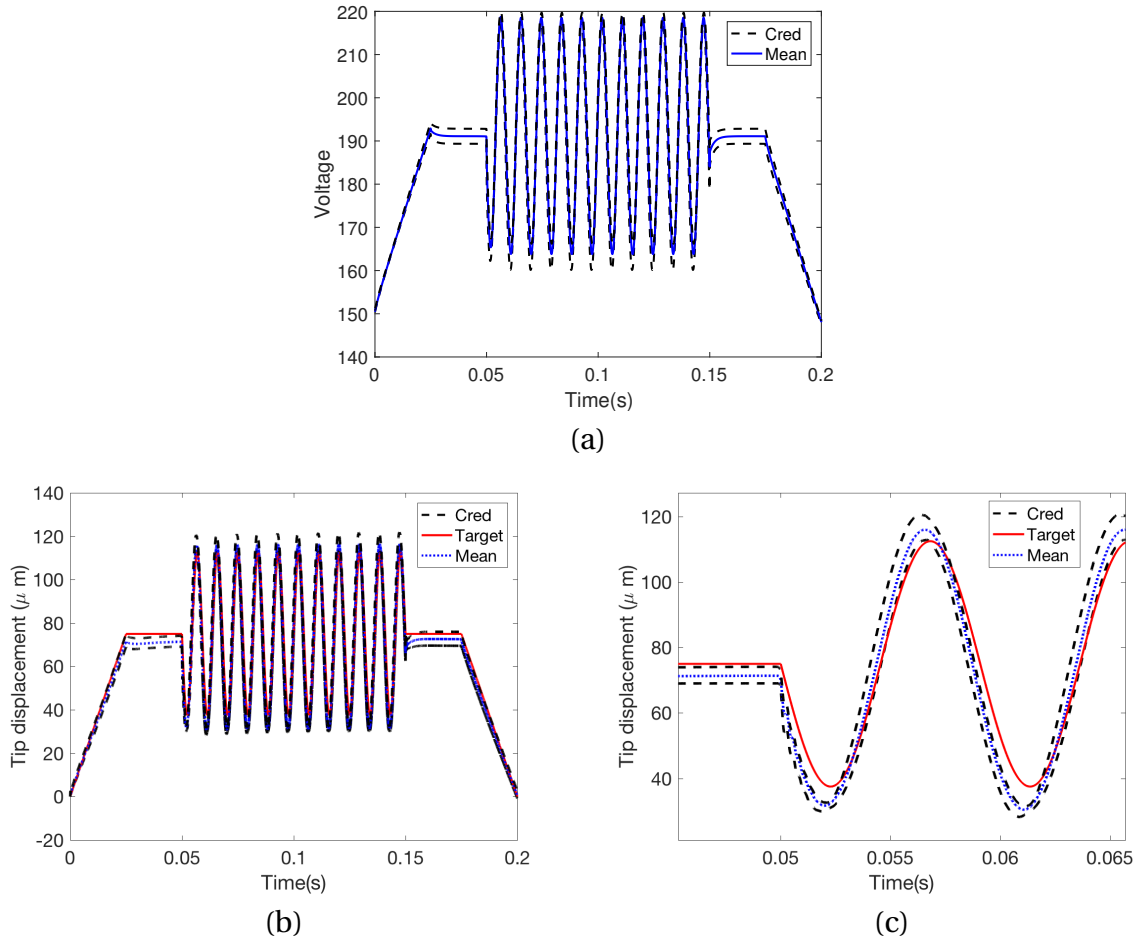


**Figure 6.3** The HEM credible intervals of the tracking problem for (a) the control and (b),(c) the tip displacement.

uncertainty. The combined control is robust with respect to the parameter uncertainty and maintain voltages on normal levels.

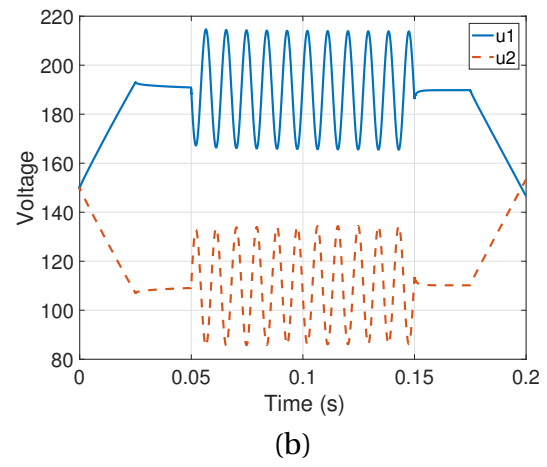
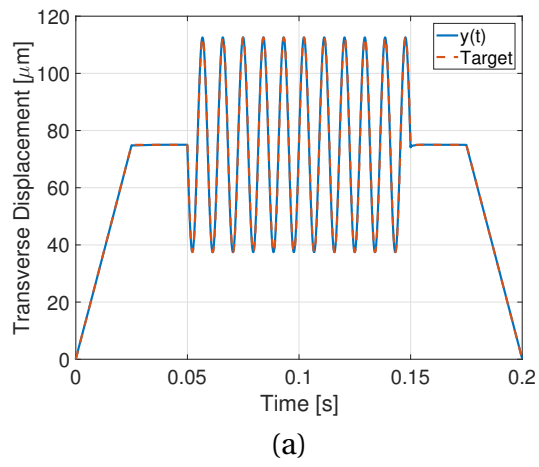


**Figure 6.4** The HEM solution using the optimal control in Figure 6.1 combined with the PI control from Section 5.3 where (a) trajectory and (b) control.



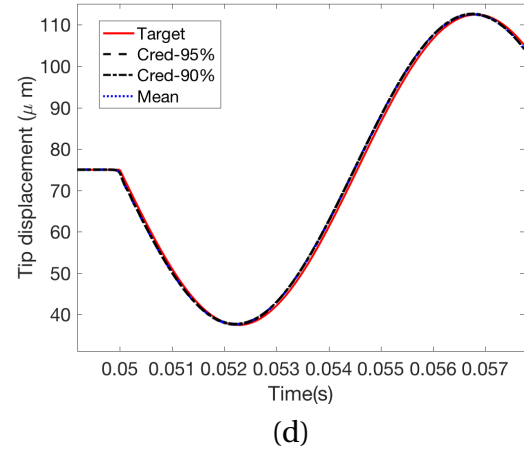
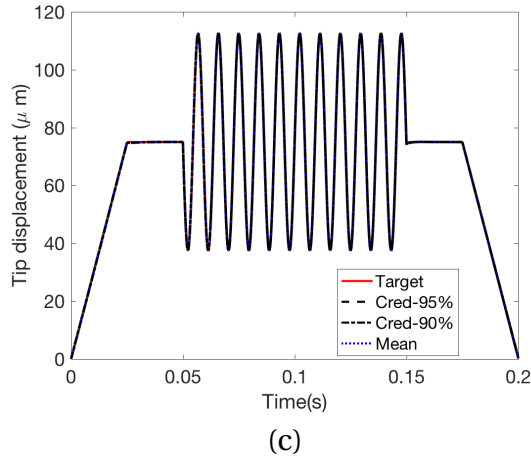
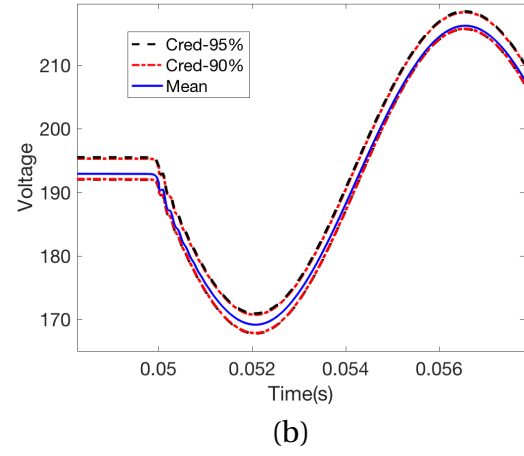
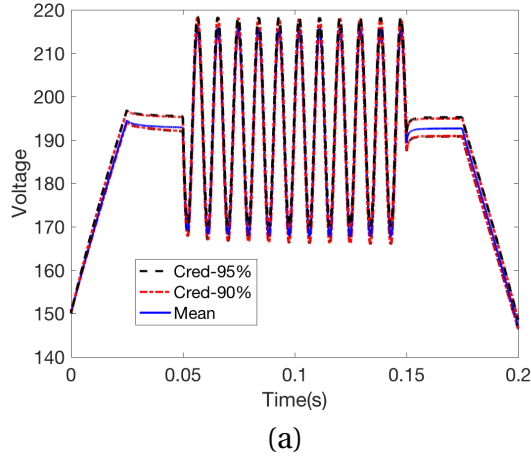


**Figure 6.5** The HEM credible intervals of the tracking problem with combining the optimal control and PI control for (a),(b) the control and (c),(d) the tip displacement.

## CHAPTER

# 7

## CONCLUSION

We employed a model for a PZT bimorph actuator that incorporates a Homogenized Energy Model (HEM) for the strain and polarization of the PZT. The numerical results replicate the hysteresis loops of the PZT. This is a vast improvement over the linear model, which ignores the nonlinear effects that are inherent to PZT in highly-dynamic drive regimes. Modeling these nonlinearities with the HEM will facilitated more efficient control algorithms for the micro-air vehicles (MAV). We were able to determine nominal parameter values that allowed the model to fit the data.

With these nominal parameters, we determined using local and global sensitivity analysis that the four parameters  $d_{\pm}$ ,  $\gamma_{pzt}$ ,  $P_R^{\pm}$ , and  $\epsilon_R^{\pm}$  are identifiable in the sense they are uniquely determined by the data. We developed a scaled subset selection to determine the sensitivity measures that is effective for problems with parameters on drastically different scales. We then compared the results of the scaled subset selection method to four different methods. With the identifiable set, we fixed the other parameters and performed Bayesian inference. We then used these parameter uncertainties to propagate them through the model to construct 95% credible and prediction intervals that can be used to help develop

a control algorithm.

We observed that we can perform dynamic mode decomposition with control (DMDc) on the HEM for a bimorph actuator to construct a surrogate model. The surrogate model can be used to implement a PI controller for the system. When the control developed from the DMDc is applied to the HEM in a feedforward algorithm, we observe that the solution is stable, but is less accurate than in the feedback problem on the surrogate model. When the control developed from the DMDc is applied to the HEM, we observe that the controller accurately tracks a discontinuous target function even when noise is applied to the control. We were able to extend DMD using interpolation to make a control and parameter dependent model. This model provides a significant speed up with an accepted amount of loss of accuracy.

With a parameter and control-dependent surrogate model, we are capable of developing control algorithms for the HEM that is robust to uncertainty. We focus on quantifying the uncertainty in an optimal tracking control. The optimal control was solved using the surrogate model. The reduced computation time of the surrogate model allowed us to quantify the robustness of the optimal control. However, the optimal control, when applied to the full order model as a feedforward control, does not track as well as we desired. To adjust for this, we implemented a PI control along with the feedforward optimal control to improve tracking. We designed a robust control with respect to parameter uncertainty that tracks very well.

In future research, we will quantify uncertainty using a more informative data set, since the results are limited to the information in the data. It would be optimal to have a data set that consist of an impulse response which maximizes the amount of information in the data. This will yield informing more parameters and quantifying more uncertainty. However, to accomplish this, we need to test our surrogate model under an impulse response. We need to identify the limitations of the surrogate model. We need to test that we can reproduce the uncertainty quantification results using the reduced order model. If DMD does not approximate the results well, we may have to look into active subspace surrogates that are both time and control dependent.

We should also test if we can perform uncertainty quantification on additional parameters. The sensitivity analysis leads us to believe that there is a possibility for five to seven influential parameters. It would be interesting to investigate these other influential parameters. Additional testing of DMD with parameter interpolation is necessary to assess its

capability to interpolate over more parameters. Thus, we must further investigate sparse grid algorithms. MATLAB's *griddatan* is not an efficient algorithm, because *griddatan* employs the Delaunay triangulation algorithm. Note that *griddatan* takes almost half of the time as the full-order model and when we increase the number of nodes *griddatan* will take longer. There are other methods that may improve the speed of DMD with parameter interpolation. We also could attempt to adjust the *griddatan* code to compute the Delaunay triangulation algorithm once and then pass the triangulation as an argument to the interpolating part of the code. We should also investigate using the more robust complex step method when approximating derivatives for the sensitivity analysis. Finally, we should look into other methods of synthesizing uncertainty quantification and control design. One method is to consider a game theory problem where the uncertainty of the parameters is the opponent. This work has laid the foundation for future research.

## BIBLIOGRAPHY

- [1] Astrom, K. J. & Murray, R. M. *Feedback Systems: An Introduction for Scientists and Engineers*. Princeton University Press, 2008.
- [2] Banks, H. T., Cintrón-Arias, A. & Kappel, F. “Parameter Selection Methods in Inverse Problem Formulation”. *Mathematical Modeling and Validation in Physiology: Applications to the Cardiovascular and Respiratory Systems*. Ed. by Batzel, J. J., Bachar, M. & Kappel, F. Berlin, Heidelberg: Springer Berlin Heidelberg, 2013, pp. 43–73.
- [3] Braun, T. *Beam Code*. MATLAB-based on: [https://rsmith.math.ncsu.edu/Smart\\_Material\\_Systems/Chapter8/Beam\\_Code/](https://rsmith.math.ncsu.edu/Smart_Material_Systems/Chapter8/Beam_Code/). 2005.
- [4] Bravo, N., Crews, J. & Smith, R. C. “Data-Driven Model Development and Feedback Control Design for PZT Bimorph Actuators”. *Proceedings of the ASME 2017 Conference on Smart Materials, Adaptive Structures and Intelligent Systems* (2017).
- [5] Bravo, N., Crews, J. & Smith, R. C. “Uncertainty Quantification for PZT Bimorph Actuators”. *Proceedings of the SPIE 2018 Conference on Behavior and Mechanics of Multifunctional Materials and Composites* (2018).
- [6] Bravo, N., Smith, R. C. & Crews, J. “Surrogate Model Development and Feedforward Control Implementation for PZT Bimorph Actuators Employed for Robobee”. *Proceedings of the SPIE 2017 Conference on Behavior and Mechanics of Multifunctional Materials and Composites* **10165** (2017).
- [7] Brunton, S. L., Proctor, J. L., Tu, J. & Kutz, N. “Compressed sensing and dynamic mode decomposition”. *Journal of Computational Dynamics* **2.2** (2015), pp. 165–191.
- [8] Coleman, K., Lewis, A., Smith, R. C., Williams, B., Morris, M. & Khuwaileh, B. “Gradient-Free Construction of Active Subspaces for Dimension Reduction in Complex Models with Applications to Neutronics”. *SIAM/ASA Journal on Uncertainty Quantification* **7.1** (2019), pp. 117–142.
- [9] Constantine, P. *Active Subspaces: Emerging Ideas for Dimension Reduction in Parameter Studies*. SIAM, 2015.
- [10] Constantine, P. & Diaz, P. “Global sensitivity metrics from active subspaces”. *Reliability Engineering System Safety* **162** (2017).
- [11] Crews, J., Bravo, N. & Smith, R. C. “Model Development for PZT Bimorph Actuation Employed for Micro-Air Vehicles”. *Proceedings of the ASME 2016 Conference on Smart Materials, Adaptive Structures and Intelligent Systems* (2016).

- [12] Crews, J., McMahan, J., Smith, R. C. & Hannen, J. “Quantification of parameter uncertainty for robust control of shape memory alloy bending actuators”. *Smart Materials and Structures* **22**.11 (2013).
- [13] Degroote, J., Vierendeels, J. & Wilcox, K. “Interpolation among reduced-order matrices to obtain parameterized models for design, optimization, and probabilistic analysis”. *International Journal for Numerical Methods in Fluids* **63** (2010), pp. 207–230.
- [14] D’Errico, J. *PolyfitnTools: MATLAB Code*. <https://www.mathworks.com/matlab-central/fileexchange/34765-polyfitn>. 2015.
- [15] Gelman, A. & Rubin, D. “Inference from Iterative Simulation Using Multiple Sequences”. *Statistical Science* **7**.4 (1992), pp. 457–472.
- [16] Haario, H., Laine, M., Mira, A. & Saksman, E. “DRAM: Efficient Adaptive MCMC”. *Statistics and Computing* **16**.4 (2006), pp. 339–354.
- [17] Hu, Z., Smith, R. & Ernstberger, J. “The homogenized energy model for characterizing polarization and strains in hysteretic ferroelectric materials: Implementation algorithms and data-driven parameter estimation techniques”. *Journal of Intelligent Material System and Structures* **23**.16 (2012), pp. 1869–1894.
- [18] Kutz, N. J. *Data-Driven Modeling and Scientific Computation*. 1st ed. Oxford University Press, 2014.
- [19] Kutz, N. J., Brunton, S. L., Brunton, B. W. & Proctor, J. L. *Dynamic Mode Decomposition: Data-Driven Modeling of Complex Systems*. SIAM, 2016.
- [20] Laine, M. *mcmcstat: MATLAB code*. <http://helios.fmi.fi/lainema/mcmc/>. 2003.
- [21] Leon, L., Smith, R. C., Oates, W. S. & Miles, P. “Analysis of a multi-axial quantum-informed ferroelectric continuum model: Part 2-sensitivity analysis”. *Journal of Intelligent Material System and Structures* **29**.13 (2018), pp. 2840–2860.
- [22] Lewis, E., Vrabie, D. & Syrmos, V. *Optimal Control*. 3rd. John Wiley and Sons, Inc, 2012.
- [23] Ma, K., Chirarattananon, P., Fuller, S. & Wood, R. “Controlled Flight of a Biologically Inspired, Insect-Scale Robot”. *Science* **340** (2013), pp. 603–607.
- [24] McKay, M., Beckman, R. & Conover, W. “A comparison of Three Methods for Selecting Values of Input Variables in Analysis of Output from a Computer Code”. *Technometrics* **42**.1 (2000), pp. 55–61.

- [25] McMahan, J. A., Crews, J. H. & Smith, R. C. "Inversion algorithms for the homogenized energy model (HEM) for hysteresis in ferroelectric and shape memory alloy compounds". *Journal of Intelligent Material System and Structures* **24.15** (2013), pp. 1796–1821.
- [26] Morris, M. "Factorial Sampling plans for preliminary computation experiments". *Technometrics* **33.2** (1991), pp. 161–174.
- [27] Oates, W. S., Zrostlik, R., Eichhorn, S. & Smith, R. C. "A nonlinear optimal control design using narrowband perturbation feedback for Magnetostrictive Actuators". *Journal of Intelligent Material System and Structures* **21.16** (2010), pp. 1681–1693.
- [28] Proctor, J. L., Brunton, S. L. & Kutz, N. J. "Dynamic Mode Decomposition with Control". *SIAM J. Applied Dynamical Systems* **15.1** (2016), pp. 142–161.
- [29] Quaizer, T. & Monnigmann, M. "Systematic identifiability testing for unambiguous mechanistic modeling: applications to jak-stat, map kinase, and nf- $\kappa$ b signaling pathway models". *BMC Systems Biology* **3.50** (2009).
- [30] Rathinam, M. & Petzold, L. "A new look at proper orthogonal decomposition". *SIAM Journal on Numerical Analysis* **41.5** (2003), pp. 1893–1926.
- [31] Saltelli, A. "Making best use of model evaluations to computer sensitivity indices". *Computer Physics Communications* **145** (2002), pp. 280–297.
- [32] Schmid, P. "Dynamic Mode Decomposition of numerical and experimental data". *Journal of Fluid Mechanics* **656** (2010), pp. 5–28.
- [33] Smith, R. C. *Smart Material Systems: Model Development*. Philadelphia, PA: SIAM, 2005.
- [34] Smith, R. C. *Uncertainty Quantification: Theory, Implementation, and Applications*. Philadelphia, PA: SIAM, 2014.
- [35] Smith, R. C. & Hu, Z. "The homogenized energy model for characterizing polarization and strains in hysteretic ferroelectric materials: Material properties and uniaxial model development". *Journal of Intelligent Material System and Structures* **23.16** (2012), pp. 1833–1867.
- [36] Smolyak, S. "Quadrature and interpolation formulars for tensor products of certain classes of functions". *Doklady Akademii Nauk SSSR* **4.240-243** (1963).

- [37] Sobol, I. “Global sensitivity indices for nonlinear mathematical models and their Monte Carlo estimates”. *Mathematics and Computers in Simulation* **55** (2001), pp. 271–280.
- [38] Sobol, I. & S., K. “Derivative based global sensitivity measures and their link with global sensitivity indices”. *Mathematics and Computers in Simulation* **79.10** (2009), pp. 3009–3017.
- [39] Tu, J., Rowley, C., Kutz, N. & Shang, J. “Spectral Analysis of Fluid Flows using sub-Nyquist rate PIV data”. *Experiments in Fluids* **55.9** (2014), pp. 1–13.
- [40] Wang, Q., Du, X., Xu, B. & Cross, L. “Electromechanical Coupling and Output Efficiency of Piezoelectric Bending Actuators”. *IEEE Transactions on Ultrasonics, Ferroelectrics and Frequency Control* **46.3** (1999), pp. 638–646.
- [41] Wentworth, M. “Parameter selection and verification techniques based on global sensitivity analysis illustrated for an HIV model”. *SIAM Journal of Uncertainty Quantification* (2016).
- [42] Wood, R. “The First Flight of a Biologically Inspired At-Scale Robotic Insect”. *IEEE Transactions on Robotics* **24.2** (2008), pp. 341–347.
- [43] Wood, R., Steltz, E. & Fearing, R. “Nonlinear Performance Limits for High Energy Density Piezoelectric Bending Actuators”. *Proceedings of the 2005 IEEE International Conference on Robotics and Automation* (2005), pp. 3633–3640.
- [44] Wood, R., Steltz, E. & Fearing, R. “Optimal Energy Density Piezoelectric Bending Actuators”. *Sensors and Actuators A: Physical* **119.2** (2005), pp. 476–488.